Ordered Mesoporous Silica for Drug Delivery in Topical Applications

Politecnico di Torino
Department of Applied Science and Technology
XXVIII cycle

PhD thesis
2013-2016

Ordered Mesoporous Silica for Drug Delivery in Topical Applications

Andrea Gignone
Tutor: Prof. Barbara Onida

SOMMARIO

ACRONYMS

Ab-Initio Molecular Dynamics	AIMD
Active Pharmaceutical Ingredient	API
Amikacin Sulfate	AKS
Brauner-Emmet-Teller	BET
Clotrimazole	CTZ
Controlled Release Technology	CRT
Density Functional Theory	DFT
Differential Scanning Calorimetry	DSC
Dynamic Light Scattering	DLS
Drug Delivery	DD
Drug Delivery System	DDS
Ethanol	EtOH
Field Emission Scanning Electron Microscopy	FESEM
Fourier Transform Infrared	FTIR
High Pressure Liquid Chromatography	HPLC
Incipient wetness impregnation	IWI
Korea Advanced Institute of Science and Technology	KIT
Maximum Toxic Concentration	MTC
Michigan State University	MSU
Minimal Effective Concentration	MEC
Mobil Crystalline of Materials	MCM
Non Linear Density Functional Theory	NLDFT
Ordered Mesoporous Silica	OMS
Pore Size Distribution	PSD
Root Mean Square Deviation	RMSD
Santa Barbara Institute	SBA
Silanol	SiOH
Solid State Nuclear Magnetic Resonance	SSNMR
Specific Surface Area	SSA
Supercritical CO2	scCO2
Termogravimetric	TG
Tetraethoxysilane	TEOS
Ultaviolet Visible	Uv-Vis
X-Ray Diffraction	XRD

INTRODUCTION

This PhD thesis focuses the development and characterization of all physicochemical aspects of a new controlled release technology for two active pharmaceutical ingredient principle (Clotrimazole and Amikacin Sulfate) using ordered mesoporous silica until the introduction onto the market.

The first chapter comprehends the characterization of different OMS synthesized and commercially available; the study of different incorporation techniques based on hydrophilicity/hydrophobicity of API; the characterization of the new impregnated OMS.

Chapter 2 is oriented on the interaction details of API on silica surfaces. A closer look is given to the big questions of OMS-drug phenomena: mobility, solubility, bioavailability, etc.

Chapter 3 highlight the differences between OMS and the spatial assembly of drug inside the mesoporous channels.

Chapter 4 describes the development of the new CRT for AKS describing all the main aspect of the innovative semisolid formulation. In-vitro and ex-vivo release test has been produced and characterized, revealing the functionality of the OMS reservoir effect.

In chapter 5 the same DDS have been developed for CTZ. Both the DDS have been compared with commercially available creams.

ORDERED MESOPOROUS SILICA AS DRUG DELIVERY SYSTEM: STATE OF THE ART

ABSTRACT

Drug delivery (DD) is the method or process of administering a pharmaceutical compound to achieve a therapeutic effect in humans or animals. For this purpose, several drug delivery systems (DDSs) have been formulated. These include liposomes, proliposomes, microspheres, gels, prodrugs, cyclodextrins, among others. Similar developments with other compounds have produced a plethora of new devices, concepts and techniques that together have been termed controlled-release technology (CRT). Amorphous silica plays a key role due to its favourable characteristics, such as high specific surface, biocompatibility, etc. In this chapter, starting from an overview on DDSs, the discussion will be focused on ordered mesoporous silica (OMS). Topics of this part will be the applications, objects and fields of use of OMS. Numerous questions will be open and answered regarding the main issues of OMS literature: firstly, the amorphization of the Active Pharmaceutical Ingredient (API); secondly, the different types of incorporations; thirdly, the requirement of DDS for low soluble API and, lastly, the description of a new CRT.

DRUG DELIVERY SYSTEMS

A drug delivery system (DDS) is defined as a formulation or a device that enables the introduction of a therapeutic substance in the body. It improves efficacy and safety by controlling the rate, time and place of release. This process includes the transport of a pharmaceutical compound in the body with the aim of achieving safely a desired therapeutic effect at the area where it is needed.[1] Any DDS comprises a drug formulation, a medical device or dosage form (to carry the drug inside the body) and a mechanism for the release. These systems have several criteria, ranging from ease of delivery to effectiveness of the drugs. Conventional drug delivery (DD) involves the preparation of the drug into a suitable form, such as a compressed tablet for oral

administration or a solution for intravenous administration. These dosage forms have been found to have serious limitations in terms of higher dosage requirement, lower effectiveness, toxicity and adverse side effects.[2] This is the case of many medications, which have unacceptable side effects due to the drug interacting with parts of the body that are not the target. Side effects limit the ability to design optimal medications for many diseases, such as cancer, neurodegenerative and infectious diseases.[3] It is also important to consider the way in which a drug is metabolized by the body. For instance, some Active Pharmaceutical Ingredient (API) are destroyed in the intestinal tract, therefore they cannot be introduced orally to the body. Others may be dangerous in large amounts, which means that for patient safety it should be used a time-release method to deliver the drug.[2] In addition, drug dosage must be carefully calculated so that the body can use the drug. This requires a DDS which allows for precise dosing.[2] Hence, it is necessary to develop suitable dosage forms or controlled DDS to allow the effective, safe and reliable application of the pharmaceutical compound to the patient.[4] Such systems are being developed to overcome the limitations of conventional dosage forms and offer many advantages, which include:[5]

- Improved efficiency by preventing peak-valley fluctuations
- Increased convenience
- Decreased toxicity
- Decreased side effects
- Decreased dosage frequency
- Shorter hospitalizations
- Lower healthcare costs (both short and long term)
- Viable treatments for previously incurable diseases
- Potential for prophylactic applications
- Site specific delivery
- Better patient compliance

Several studies have shown that the benefits aforementioned can be achieved by correct timing of drug administration and controlled kinetics of drug release. Thus, controlled drug release regulates the rate, the location and aims at optimizing drug efficiency while simultaneously reducing adverse collateral effects.[2,5–9]

DRUG RELEASE PROFILES

The DDS employed plays a vital role in controlling the pharmacokinetic effect of the drug. An optimal DDS ensures that the active drug is available at the site of action for the correct time and duration. The drug concentration at the appropriate site should be above a minimal effective concentration (MEC) and below a minimal toxic concentration (MTC). This concentration interval is known as the therapeutic range (Figure I.1). Dosage forms can be differentiated according to the way the drug is released.

The immediate release is probably the most used. The drug is released immediately after administration. These forms usually release the drug in a single action following a first order kinetics profile. In other words, the drug is released initially very quickly and then passes through the mucosal membrane into the body, reaching the highest plasma level in a comparatively short time. Once taken into the body, the drug is distributed throughout the body and elimination by metabolism and excretion occurs. This elimination process also follows a first order kinetics.

The modified release of API can occur in three different ways: delayed, extended and pulsed release. In the first case, the API release takes place sometime later the initial administration, after which the release is immediate. The second one is when the drug release occurs for a prolonged period after ingestion. This allows a reduction in dosing frequency compared to a drug presented as a conventional dosage form.

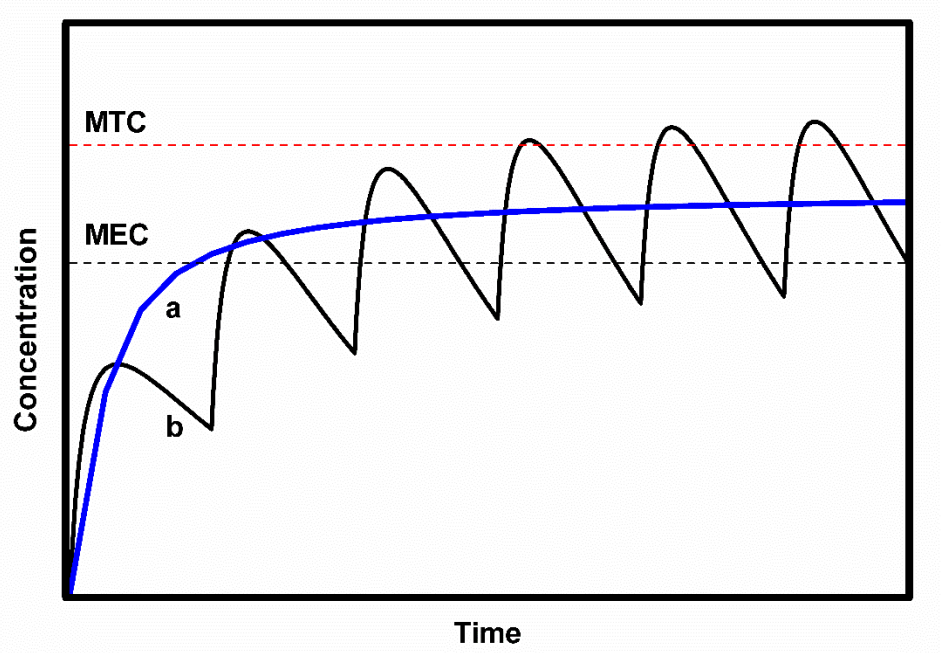

Figure I.1: Example of API concentration with zero order release (**a**) and pulsed administrations (**b**).

For immediate release dosage forms the time interval in which the plasma concentration reach the drug therapeutic range can be quite short.[10,11] Therefore, frequent dosing or pulsed release, with its associated compliance problems, is required. As a consequence, there is a considerable fluctuation in drug concentration level, which often is out of the therapeutic range.[4] This is especially an issue in chronic diseases when patients need to take the medication for prolonged periods (Figure I.1.b).

Extended release can be achieved using a sustained or a controlled delivery dosage forms. Sustained release systems maintain the rate of drug release over a sustained period (Figure I.1.a). They achieve this mostly by the use of suitable polymers. On the other hand, controlled release systems also offer a sustained release profile but they are designed to lead to predictably constant plasma concentrations. This means that they are actually controlling the drug concentration in the

body, not just the release of the drug from the dosage form, as is the case in a sustained release system.

DRUG CARRIERS

Every pharmaceutical compound contains an API, which has a direct effect in the diagnosis, treatment or prevention of diseases. It is important to realise that the API is just one part of the medicine and it cannot be administered to the patient on its own. Therefore, it is necessary to formulate the drug into a dosage system containing drug carriers, which are forms that serve as mechanisms to improve the delivery and the effectiveness of drugs. They can be attached to drug molecules for targeted delivery, increased efficiency or controlled release. Many of these can also act as buffers to reduce the toxic effects of medications. These compounds can also change the way the drug acts in the body.[12,13] Drug carriers are used in controlled release technology (CRT) to prolong in-vivo actions, decrease drug metabolism, reduce drug toxicity and determine where the drug travels and how it behaves when it gets there.[12] These include synthetic and natural compounds from a variety of sources, ranging from lipids to nanoparticles. Some of the more common drug carrier systems are reported in Figure I.2.

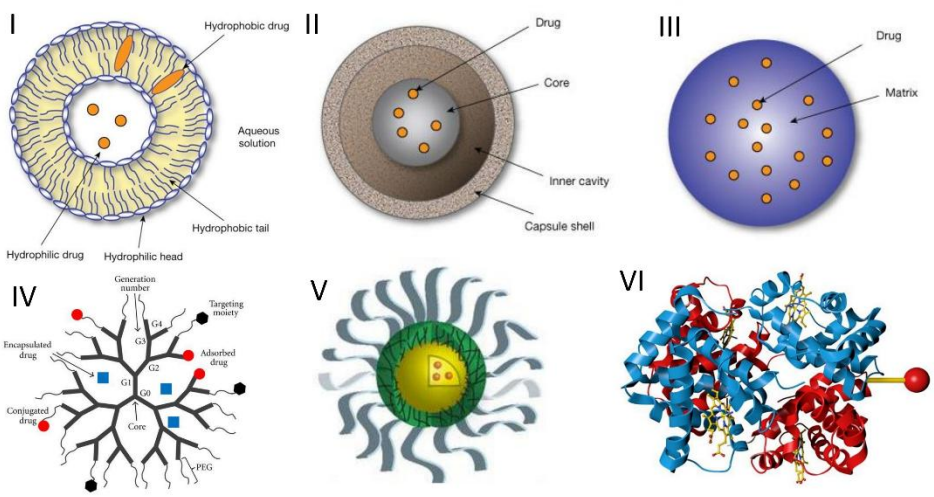

Figure I.2: Liposomes (**I**): containers made of a lipid bilayer; their limitation is the extremely high fragility of the liposomal structure and the low transport capacity of non-soluble drugs. Microspheres (**II-III**): synthetic materials, such as ceramics or polymers, or from natural materials, such as albumin. Dendrimers (**IV**): repetitively branched molecules; their properties are dominated by the functional groups on the molecular surface. Soluble polymers (**V**): hollow particles that hold drugs; drugs are loaded into the core hydrophobic block (yellow); the crosslinking block (green) provides stability to the micelle by forming pH reversible bonds that allow for triggered drug release; the grey block gives the micelle aqueous solubility and stealth. Conjugated proteins (**VI**).[14]

ORDERED MESOPOROUS SILICA

Among all the CRT, ordered mesoporous silica (OMS) are a particular case of the previous system. Silicon dioxide (SiO_2) is one of the most abundant oxide materials in the Earth's crust. SiO_2 is the essential components of all silicate materials: crystalline and amorphous. All silicates are constituted by the SiO_4 tetrahedron (Figure I.3.I). The low energy process of change the siloxane bridge (Si-O-Si) allow the formation of infinite polymorphisms.[15]

I

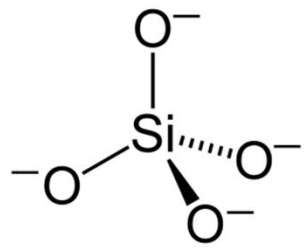

II

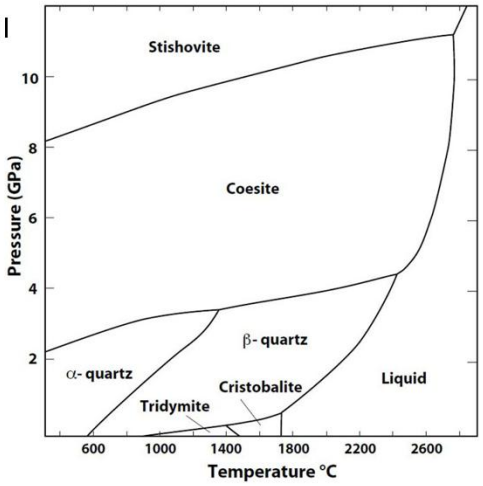

Figure I.3: The SiO_4^{4-} tetrahedron (**I**); O-Si-O angle: 109°; Si-O-Si angle: 130°-180°. Phase diagrams of silica (**II**); most of this crystalline phase are not reversible.

OMS are amorphous inorganic materials synthesized in the presence of surfactants as templates for the polycondensation of silicic species. Synthesis conditions such as source of silica, type of surfactant, ionic strength, pH and composition of the reaction mixture, temperature and duration of synthesis determine the characteristics of the porous structure and the macroscopic morphology.[16,17]

A wide variety of ionic and non-ionic surfactants has been used for obtaining materials with different porous and morphological characteristics. The pore sizes of these materials are always very homogeneous ranging from 2 to 100 nm. The huge surface area which can easily reach values of 1000 $m^2 \cdot g^{-1}$ and the wide void volume (1 $cm^3 \cdot g^{-1}$) delineate the ability of these materials as CRT. In addition, their thermal, chemical, mechanical and pH stability defines its superiority to the organic counterpart.[18–21]

Table I.1: Brief summary of the main silicas used.

Name	*MCM-41*	*MSU-H*	*SBA-15*	*KIT-6*	*Syloid*
Surfactant	C_{16}TABr	P123			None
pH	>11	≈7	<2		
Structure	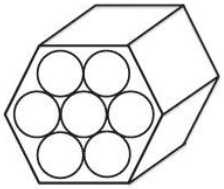 P6mmm			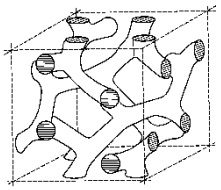 Ia3d	Disordered

In 1992 a new family of OMS was reported as MCM-X (Mobil Crystalline of Materials). They are synthesized by using alkyl ammonium surfactants (i.e. Hexadecyltrimethylammonium bromide (C16TABr)) and tetraethyl orthosilicate (TEOS) or sodium silicate in basic condition. Their pore size and wall thickness are between 4 to 2 nm. By varying the synthesis conditions, different structures of the mesophase can be obtained. For instance: hexagonal phase (MCM-41), cubic phase (MCM-48) and lamellar phase (MCM-50).[22]

The first OMS synthesized with non-ionic triblock polymers were reported by the Santa Barbara centre (Santa Barbara Amorphous).[23] As for MCM-41, selecting the right surfactant and concentration different structure can be obtained. For instance, Pluronic P-123, $HO(CH_2CH_2O)_{20}(CH_2CH(CH_3)O)_{70}(CH_2CH_2O)_{20}H$, is used mainly for the silica hexagonal structure (p6mmm); while, Pluronic F-127 for the cubic ia3d structure. The main characteristics of surfactants are:

- Chain hydrophilicity-hydrophobicity
- Head characteristic:
    - Anionic

  - Cationic
  - Amphoteric
  - Non-ionic
- Chain elongation
- Chain/Head hindrance volume ratio

These features have to be correlated with other synthesis conditions:

- Temperature
- pH
- Concentrations
- Co-solvents
- Co-surfactant
- Silica source

Other families of OMS are Michigan State University (MSU), Korea Advanced Institute of Science and Technology (KIT).

After the polycondensation, an hydrothermal treatment can be executed with the aim of enlarge and modify the pore structure and connectivity.[21,24] Subsequently, there is the removal of surfactant through filtration or extraction and calcination.

Surface silanols (SiOH) represent the last characteristic besides highly organized porosity, SSA, pore volume, chemical stability, etc. Their content depends on the way the surfactant is removed. It can be modulated by post synthesis treatments. They are generated as stabilization of the silica surface. The presence of SiOH on the surface promotes the adsorption of molecules (from water to proteins) through hydrogen bonding (H-bond).[25]

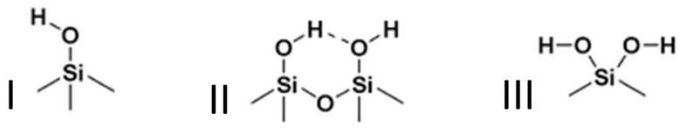

Figure I.4: The surface isolated SiOH (I), H-bonded (II) and geminal (III).

Furthermore, the presence of geminal and single SiOH allows the chemical modification grafting different functionalities through covalent linkages. For instance, they can react with alkylchlorosilanes in order to obtain an hydrophobic surface.[26]

OMS FOR DRUG DELIVERY

Due to these outstanding features, OMS are excellent candidates in biomedical systems as local drug delivery systems and bone tissue regeneration.[13,27–32] For controlled release applications, it has been shown that silica is able to store and gradually release therapeutically relevant drugs. Furthermore, silica is used to enhance the biocompatibility of several DDS, such as magnetic nanoparticles, biopolymers and micelles.[27] Vallet-Regi et al. were the first to explore the drug release properties of OMS using ibuprofen. To incorporate API they dissolved it in hexane, obtaining an incorporated quantity of 30% by mass.[33] They also have demonstrated the release of erythromycin and alendronate.[34,35] Other controlled release systems have shown the delivery of API such as vancomycin and adenosine triphosphate, fluorescein, β-oestradiol, cholestame and calceine, camptothecin.[31,36–39]

OMS also show ability in the dissolution of poorly water-soluble drugs. An insufficient dissolution of hydrophobic drugs in the gastrointestinal fluids strongly limits the oral bioavailability. Mellaerts et al. loaded itraconazole on SBA-15, an antimycoticum known for its poor aqueous solubility. Gastrointestinal dissolution tests produced a supersaturated solution giving rise to enhanced trans epithelial intestinal transport.[40] Ambrogi et al. using carbamazepine into MCM-41 have verified a remarkable increase of dissolution rates.[41] This have evidenced that OMS is a

promising carrier to achieve enhanced oral bioavailability for drugs with extremely low water solubility.

At the state of the art, the explanation of these phenomena should be a consequence of drug amorphization inside OMS. Numerous works have demonstrated drug amorphization inside OMS just by mechanical mixing, without any other energy supplement. These could demonstrate that the most stable condition of drug inside silica mesopores is an amorphous state. Indeed, NMR studies have evidenced high mobility of drug inside OMS at ambient temperature and pointed out weak interactions.[42,43]

These arguments will be discussed in chapter 2.

DRUG LOADING STRATEGIES

Drug loading into a host material can be performed with different techniques.[44]

The solution method is probably the most widely used drug loading process. In this method, the drug is dissolved in a suitable solvent and the porous material is dipped in this solution. The drug molecules are absorbed on the pore walls. The solution method last from one to several hours, after which OMS is separated from the solution by filtration or centrifugation. In conclusion, the particles are dried by removing the remaining solvent.[45] If the drug concentration near to the adsorbent surface exceeds the saturation concentration, e.g. during the drying step, the drug may start to crystallize on the external adsorbent surface. Since this crystalline surface fraction may have different dissolution properties than the amorphous solids inside the pores, its formation is not favourable. If crystalline solids are formed on the surface, they can be removed by washing the loaded particles. Unfortunately, the washing process is difficult to control.[46] Solution loading is simple to perform and it gives reproducible results as the properties of the carrier are consistent.

High temperature is not required during the process, making it suitable for loading sensitive molecules. To achieve high loading degrees, relatively high concentrations of loading solutions have to be used. This can be challenging, especially with poor soluble drugs. To overcome this inconvenience, different solvents can be used. Among all the possibilities, apolar solvent are the most appropriate. Indeed, it has been demonstrated that water, ethanol and other polar solvents compete in the adsorption with the drug. In fact, due to the high interaction energy and strong H-bonds formed with surface silanols, these molecules are strayed from silica surface only during degas operations. On the other hand, most apolar solvent are carcinogen or toxic.[8] The main disadvantage of the immersion method is the large proportion of the drug that is wasted in the filtration/centrifugation process. It is also difficult to predict the drug loading degree that will be achieved.

The Incipient wetness impregnation (IWI) method consists in contacting the OMS with a volume of solvent equal to the silica pore volume. The capillary action draws the solution into the pores and the drug dissolved in it. The support can be dried to drive off the volatile components within the solution, depositing the drug on its surface. While drying, the drug located in the solution outside the pores is driven inside by diffusion, which is a much slower process. There are different methodologies distinguished by the volume of solvent used:[47]

- Impregnation by soaking or with an excess of solution: excess liquid is eliminated by evaporation or by draining;
- Dry or pore volume impregnation: the amounts of drug are introduced in the volume corresponding to the pore volume of the support;
- IWI: it is a procedure similar to dry impregnation, but the volume of the solution is more empirically determined to correspond to that beyond which the support begins to look wet.

The main advantage of this methods is that it is easy to control the amount of the drug that is loaded in the carrier. Furthermore, the drug is efficiently loaded and the method is, therefore, suitable for expensive molecules.

Figure I.5: Comparison between different incorporation process and drug adsorption.[48]

Covalent grafting method is widely used for payload molecules, which can be loaded by attaching them covalently on the mesoporous material surfaces. A commonly used method is to form a peptide bond between the amine group of a payload molecule and a carboxylic acid linker on the surface of the material. The benefit of a chemical grafting is the possibility to control the release of the payload molecules. The release can be determined by cleavage of the payload molecule from the linker or erosion of the porous material. In chemical grafting, the drug load is controlled by the surface area and the density of the linker and the payload molecules. The maximum loading degree that can be achieved is inevitably lower than this that can be achieved with non-covalent adsorption methods, because the payload molecules cannot accommodate the whole pore volume. With this method, there is a risk that the payload molecule will not be released from the linker. Nevertheless, this method provides stronger chemical interactions between the drug molecule and the surface.[16]

It is important to remember that all the methods aforementioned have an inherent disadvantage: the employment of organic solvents. The

subsequent solvent removal steps add processing complexity and increased cost to these processes. In addition, there are safety issues to be considered and appropriate environmental protection measures must be initiated when using organic solvents. To avoid this, other techniques can also be employed to load drugs onto OMS.

In the hot melt method drug molecules are loaded from a molten phase. The drug is heated along with the adsorbent to a temperature above the melting point of the drug. A prerequisite for using this method is that both the adsorbent and the drug have sufficient thermal stability, which excludes all of the pharmaceuticals that are known to decompose upon melting.[46] Some drugs as ibuprofen has been successfully loaded by using this method. However, this method is not generally appropriate because it requires the molecules to withstand a temperature above their melting point and the viscosity must be low enough to allow the molecule to efficiently enter the pore structure.

Vapour deposition is another technique. In high vacuum condition, the melting temperature of the drug is reduced. Consequently, it is possible to avoid degradation and evaporates small amount of drug that will be deposited in a cold region (OMS). This method allows to control the purity of the drug avoiding any external parameter: solvent, viscosity, solubility, etc.

The physical mixing, for instance, requires only that drug and carriers are blended in desired proportions using spatula for some minutes. A more scalable process of the physical mixing is the ball milling. Indeed, during the process the particles are physically broken to favour the drug entrapment and reconstituted due to the strong interaction energy of silica surfaces.

SUPERCRITICAL CO_2

Organic solvents can be replaced with supercritical carbon dioxide. Drugs may also be incorporated by dissolving them in compressed high volatile fluids like supercritical carbon dioxide ($scCO_2$), at temperatures and pressures above their critical point.[49] A supercritical fluid can be defined as any substance present at a temperature and pressure higher than its critical value, and which has a density close to or higher than its critical density. At the point at which the critical temperature and critical pressure are reached, the density of both the liquid and vapour are equal and the supercritical phase is obtained.

The employment of $scCO_2$ for drug loading offers many advantages compared to traditional organic solvents. This topic will be discussed in details in chapter 1.

Supercritical fluids have both liquid and gas-like properties. Their liquid-like nature enables them to act like a solvent, while their gaseous properties allow quick and easy diffusion through materials.[50] When the supercritical state is reached, properties like density, viscosity and the vapour–liquid equilibrium ratio become dependent on temperature at a certain pressure, which permits the solubility of solutes in the supercritical fluid to be controlled.

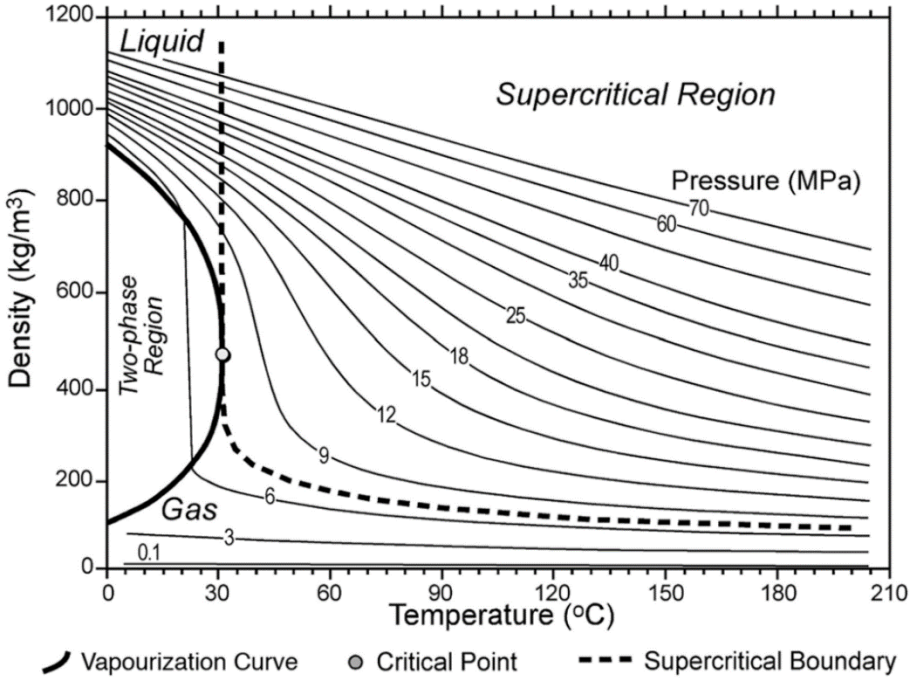

Figure I.6: Phase diagram of a CO_2 showing the supercritical region and critical point.[50]

At pressures and temperatures not too far from its critical point, a supercritical fluid has a high compressibility. Therefore, its density and its solvent power are easily adjustable over a wide range with a minimal change in temperature or pressure. This tunability may be used to control the solubility parameter.[50]

The solubility parameter is a coefficient that indicates a substance solubilisation in a specific solvent. Materials with similar values are likely to be miscible, hence a solute presents a complete solubility or miscibility if it has a solubility parameter as equal as possible to that of the solvent.

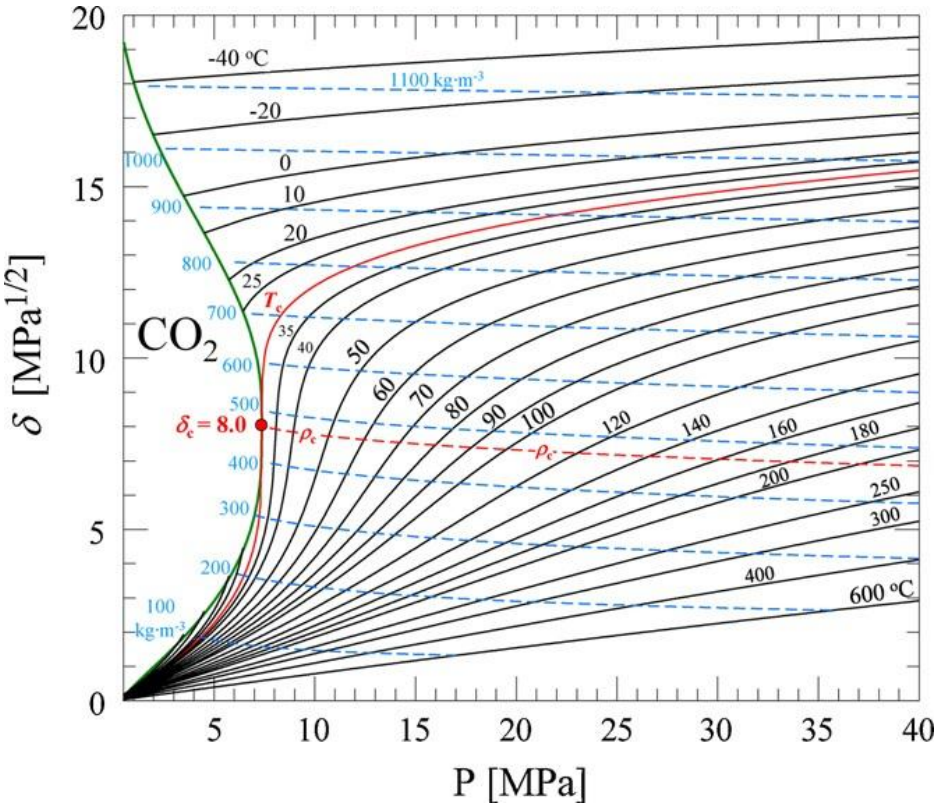

Figure I.7: CO_2 solubility parameter as a function of Temperature, Pressure and Density.[50]

In a supercritical fluid, the solubility parameter tends to increase with the fluid density (at constant temperature).[50] Another advantage includes the reduced processing complexity, as there is no need for solvent removal steps associated with organic solvent usage.[51–53] Carbon dioxide is the most widely used supercritical fluid because it presents the advantage of having easily accessible critical conditions, that are a critical temperature close to ambient temperature (304.25 K) and a critical pressure which is not too high (7.39 MPa), it is inert, non-flammable and inexpensive. The critical temperature is close to a physiological value and so it is safe for heat-sensitive proteins.

One disadvantage of using supercritical fluids, however, is that specialised high-pressure equipment and knowledge are required for

processing it. Furthermore, some interesting hydrophobic drugs, which cannot be impregnated by aqueous solution-suspension soaking, can be incorporated by this method.

$ScCO_2$ is used for many applications like:

- Extraction of desired compound from other products; i.e. caffeine from coffee bean;[54]
- Chromatography;
- Cleaning;
- Biological applications:[55,56]
    - Sterilization
    - Virus inactivation
- Particle formation
    - Aerogels[57]
- Polymeric processing and foams;[58]
- Impregnation
    - Drug loading on different matrixes[59]

In this thesis, it will be used as an incorporation process for drug inside OMS. This topic will be further discussed in chapter 1.

TOPICAL APPLICATION

Among all the administration routes, topical and transdermal delivery approaches have unique advantages:

- In case of skin diseases, topical delivery directly carries drugs to the site;
- Smaller amounts of drugs are needed to produce a therapeutic effect;
- Plasma level peaking of drugs will be avoided;

- Increased bioavailability due to elimination of hepatic first-pass metabolism;
- Greatly enhanced patient compliance by eliminating frequent treating.

For these reasons and many others, currently, there are numerous topical and transdermal products on the market. Many formulations of low molecular weight drugs and macromolecules have been developed and some are currently under clinical trial.[60]

At the same time a huge number of CRT have been developed for topical diseases, such as gels with permeation enhancers, submicron emulsion vehicle systems, volatile vehicle–antinucleant polymer systems, lecithin microemulsion gel, oleo-hydrogel systems, deoxycholate hydrogels, creams containing lipid nanoparticles, solid lipid nanoparticles, liposomes as drug carriers, etc.[61]

Human skin has a surface area between 1.5 and 2.0 m^2 for adults. The skin thickness varies over the body with the thinnest part of eyelids being less than 0.1 mm thick and the thickest on the palms, soles and upper back more than 5.0 mm. Not only is the skin a protective barrier against toxic substances, pathogens, and organisms, but it is also involved in many important physiological functions such as fluid homeostasis, thermoregulation, immune surveillance and sensory detection.[62] These functions are related to the skin's complex multiple layers with each layer associated with highly specified cells and structures.

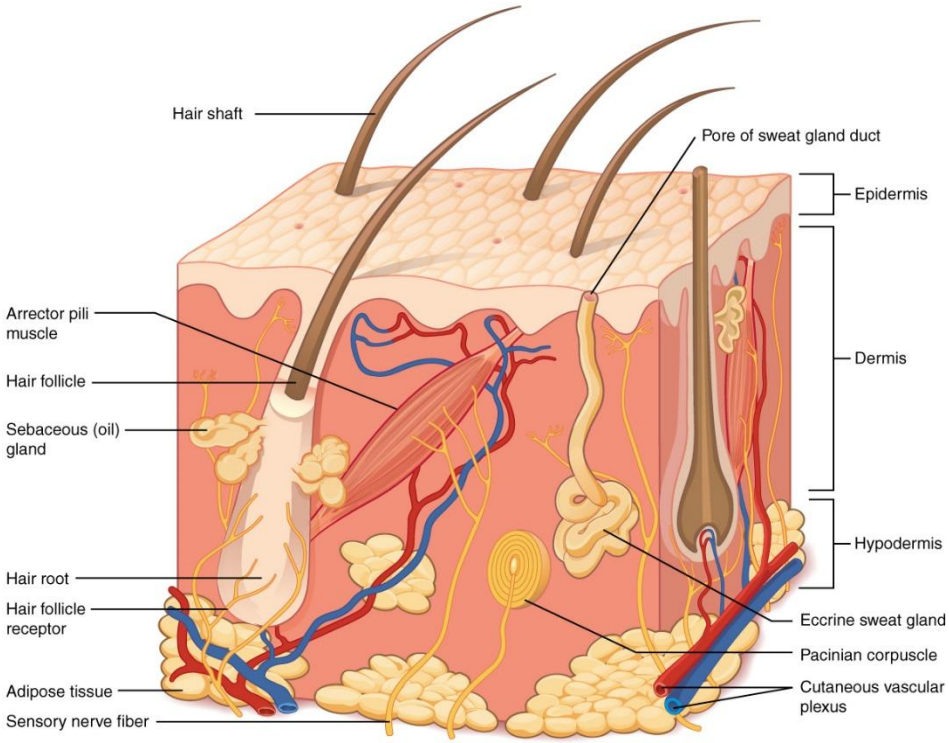

Figure I.8: A schematic image of epidermis, dermis and hypodermis structure. The appendages such as hair shaft and hair follicle, sweat gland, sebaceous gland, and arrector pili muscle are illustrated.[63]

The permeation barrier properties of human skin are mostly attributed to the top layer of the epidermis, the stratum corneum. The barrier function is related to the unique structure in the stratum corneum layer that is composed of “bricks (corneocytes) and mortar (intercellular lamellar lipid bilayers)”.[64]

Approaches that deliver drugs/active compounds through the skin barrier are referred to the topical administration (as opposed to the enteral and parenteral route). Passive and active skin penetration enhancement methods have been successfully used to improve the efficiency of either the topical delivery (the drugs/active compounds are delivered into skin strata), or transdermal delivery (drugs/active compounds are delivered into subcutaneous tissues and are taken up systemically into the body).

Topically applied therapies are promising for the treatment of skin diseases such as psoriasis, contact dermatitis and skin cancers, since the drugs are delivered directly into skin strata.

A NEW CONTROLLED RELEASE TECHNOLOGY

Despite of all the above descripted benefits of topical administration, there are some critical drawbacks, among which difficult accurate dose and the need of frequent reapplications.[11] These frequent reapplications are required because the post-application efficacy of traditional creams is limited to a period between 3 to 6 hours. In addition, recurrent treatments result in considerable inconvenience for the patient and inopportune amnesia. Moreover, many dermatologic pathologies, grouped under the generic name of chronic dermatitis, have a cyclic and recurring feature, creating complex treatment problems over the course of the patient's life. What is more, pulsed administration has period of inefficacy and overdose, due to low/high API concentration on the skin site (Figure I.1).

In order to tackle these issues, zero order release at constant skin concentration for an extended time interval is required but is utopian. Sustained controlled release systems aims to simulate as good as possible the zero order release. A new CRT comprising OMS, incorporated with different API, blended in a saturated solution of the same API is here proposed. Indeed, this semisolid formulation let to a sustained controlled release. After the application on the skin site, the dissolved API in the saturated solution explicate its function as all the commercial creams. Subsequently, the concentration of the dissolved API begins to decrease leading to the end of the cream purpose. Simultaneously, the API incorporated in OMS begun to dissolve. The API release preserves the saturated concentration inside the vehicle until the OMS is empty. As follows, the therapeutic concentration of API is kept

constant on the application site for a long and controlled time. The OMS incorporated with API develop a reservoir effect.

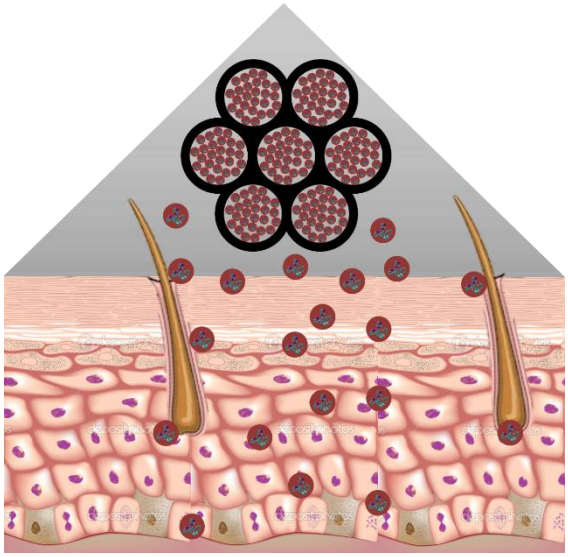

Figure I.9: A schematic image of the patented application.

This new CRT is patented at the WIPO (the global forum for intellectual property services, policy, information and cooperation) with numbers WO2012007906 A2-A3. At the European patent office as EP2593083 A2 and on the United States territory as US20130156832 A1.

DERMATOLOGICAL DISEASE

The major challenges in the skin diseases treatment include poor efficiency of drug delivery into the disease site and risks of increased toxicity associated with approaches used to improve the drug delivery efficiency.

In this thesis, two main drugs have been explored for the treatment of different diseases. The first is clotrimazole (CTZ), a synthetic imidazole derivative. It is primarily used locally in the treatment of vaginal and skin infections due to yeasts and dermatophytes. In vitro, it is most active against Candida spp., Trichophyton spp., Microsporum spp. and

Malazzesia furfur (Pityrosporon orbiculare). In addition, it has some in vitro activity against certain Gram-positive bacteria and at very high concentrations it has activity against Trichomonas spp. In the treatment of vaginal candidiasis, CTZ vaginal tablets have produced cure rates comparable with those of conventional nystatin vaginal tablets. CTZ topical preparations are generally well tolerated, but local irritation has required withdrawal of therapy in a few cases. The site of action of CTZ, like that of miconazole and the polyene antifungal agents, appears to be the cell membrane to which it is preferentially bound. It has been proposed that the mechanism of action involves an interaction with the phospholipid layer of cellular membranes causing alterations in membrane permeability. Permeability changes result in loss of essential precursors, metabolites and ions, thus inhibiting macromolecular synthesis. Absorption of CTZ through intact skin was essentially negligible in individuals with normal skin. The highest concentration of topically applied CTZ remained in the epidermis, particularly in the stratum corneum, with less appearing in the dermis, and very little penetrating subcutaneously. Consequently, topical administration avoids side effects of oral administration like itching, nausea, vomiting and abnormal liver activity.[65]

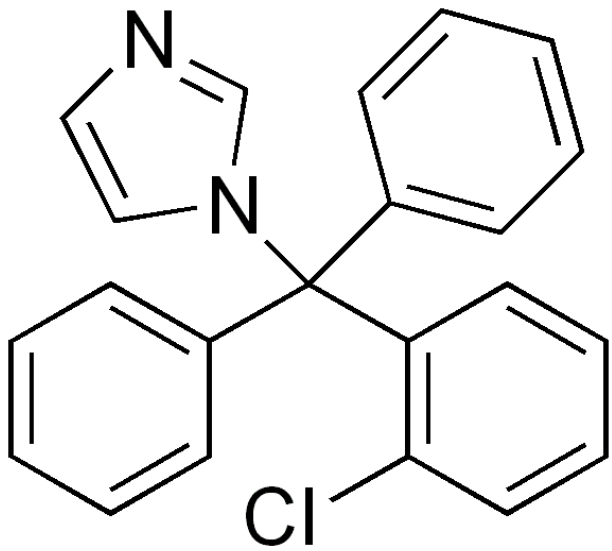

Figure 1.10: Chemical structure of Clotrimazole: 1-[(2-Chlorophenyl)(diphenyl)methyl]-1H-imidazole.[66]

The second one, Amikacin sulfate (AKS) is an aminoglycoside antibiotic used to treat different types of bacterial infections. AKS works by binding to the bacterial 30S ribosomal subunit, causing misreading of mRNA and leaving the bacterium unable to synthesize proteins vital to its growth. AKS is most often used for treating severe, hospital-acquired infections with multidrug-resistant Gram-negative bacteria, such as Pseudomonas aeruginosa, Acinetobacter and Enterobacter. AKS can also be used to treat non-tubercular mycobacterial infections and tuberculosis when first-line drugs fail to control the infection. Side effects of AKS are similar to those of other aminoglycosides. Kidney damage and hearing loss are the most important effects.

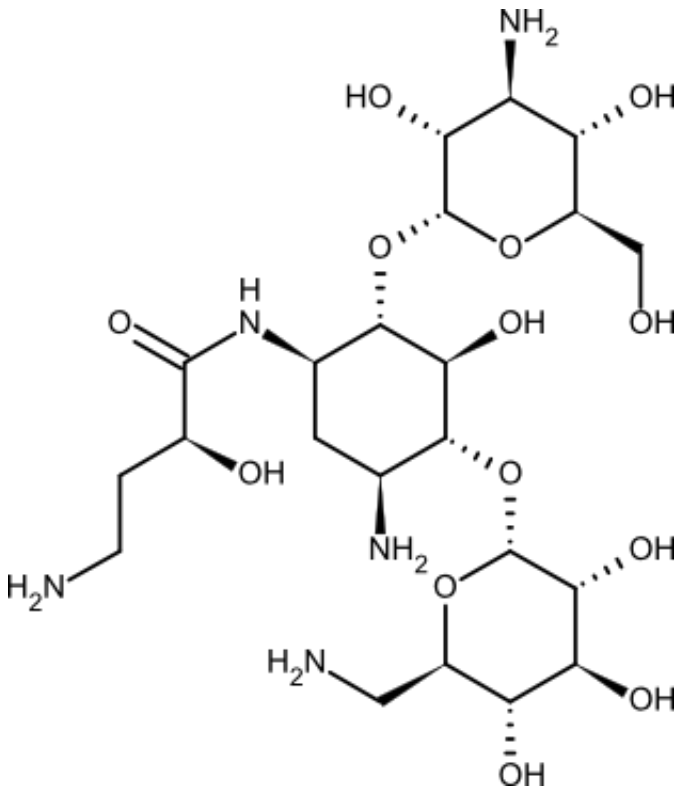

Figure I.11: Chemical structure of Amikacin: (2S)-4-Amino-N-[(2S,3S,4R,5S)-5-amino-2-[(2S,3R,4S,5S,6R)-4-amino-3,5-dihydroxy-6-(hydroxymethyl)oxan-2-yl]oxy-4-[(2R,3R,4S,5R,6R)-6-(aminomethyl)-3,4,5-trihydroxy-oxan-2-yl]oxy-3-hydroxy-cyclohexyl]-2-hydroxy-butanamide.

AKS may be administered once or twice a day but it must be given by intravenous or intramuscular route or via nebulization. For the treatment of dermatological disease, the topical route avoid the majority of side effects.[67]

CTZ and AKS were chosen for the ability to be topically administrable, low toxicity, the number of administration during the day (2-5 dose/day) and their opposite characteristics. The first drug is an antifungal, the second one is an antibiotic; one have a long half-life, the other short; but more important, CTZ is hydrophobic, while AKS is hydrophilic. Indeed, the main incorporation strategies will be $scCO_2$ for CTZ and IWI for AKS.

AIM OF THE THESIS

The aim of this PhD work was to develop and characterize all physicochemical aspects of this new CRT for CTZ and AKS using OMS until the introduction onto the market.

The first part comprehends the characterization of different OMS synthesized and commercially available; the study of different incorporation techniques based on hydrophilicity/hydrophobicity of API; the characterization of the new impregnated OMS.

Consequently, the work is oriented on the interaction details of API on silica surfaces. A closer look is given to the big questions of OMS-drug phenomena: mobility, solubility, bioavailability, etc.

Therefore, all the $scCO_2$ incorporation parameters have been studied, highlighting the differences between OMS and the spatial assembly of drug inside the mesoporous channels.

Thus, the patented CRT has been developed for AKS describing all the main aspect of the innovative semisolid formulation. In-vitro and ex-vivo release test has been produced and characterized, revealing the functionality of the OMS reservoir effect.

Finally, the same DDS have been developed for CTZ. Both the DDS have been compared with commercially available creams.

ORDERED MESOPOROUS SILICA AS DRUG DELIVERY SYSTEM: EXPERIMENTAL

MATERIALS

ORDERED MESOPOROUS SILICA

The synthesis of OMS are here reported.

MCM-41

Four different MCM-41 have been used during this thesis. The first one named MCM41-1 has been synthesized following the procedure of Jana et al.[68] Briefly, 25.04 g of hexadecyltrimethylammonium bromide (C_{16}TMABr) was dissolved in 75.22 g of water at 323 K. Subsequently, 16 g of 1,3,5-trimethylbenzene (TMB) was added and stirred vigorously. In another solution 1.8 g of H_2SO_4 and 1.8 g of waterglass (Na_2SiO_3) were added to 60 g of H_2O. These two solutions were then mixed and stirred vigorously for 30 min. Then again 30 g of water was added to this mixture, stirring constantly. The pH of the gel was adjusted close to 10 by adding dilute sulfuric acid and then the resultant gel was transferred into a teflon-lined autoclave and heated statically at 373 K for its crystallization under autogeneous pressure in an oven for 10 days. After crystallization, the solid product was recovered by filtration, washed with large amounts of warm deionized water and dried at 373 K and finally calcined in air at 813 K for 6 hours.

MCM41-2, MCM41-3 and MCM41-4 were synthesized following the procedure of Grun et al.[20] modified in order to change the pore size distribution of OMS. Briefly, n-Alkyltrimethylammonium bromides of different alkyl chain lengths were used as template: C_{16}TMABr and TMB for MCM41-2; C_{16}TMABr for MCM41-3; C_{12}TMABr for MCM41-4. The

template was dissolved in 120 g of deionized water to yield a 0.055 mol/L solution, and 9.5 g of aqueous ammonia (25 % by mass, 0.14 mol) was added to the solution. While stirring 10 g of Tetraethoxysilane (0.05 mol) (TEOS) was added slowly to the surfactant solution over a period of 15min resulting in a gel with the following molar composition: 1 TEOS:0.152 C_nTMABr:2.8 NH_3:141.2 H_2O The mixture was stirred for one hour, then the white precipitate was filtered and washed with 100 ml of deionized water. After drying at 363 K for 12 h, the sample was heated to 823 K (1 K/min) in air and kept for 5 h to remove the template.

A fifth sample was a commercially available MCM-41 bought from ACS Material (MCM41-ACS).

KIT-6

Mesoporous KIT-6 silica materials were obtained following the method reported Kleitz et al.[69] Briefly, 9.0 g of Pluronic P123 ($EO_{20}PO_{70}EO_{20}$, Sigma-Aldrich) was dissolved in 325 g of distilled water and 17.40 g of HCl (37%) under vigorous stirring. After complete dissolution, 9.0 g of 1-butanol (BuOH, Aldrich, 99%) was added. The mixture was left under stirring at 308 K for 1h, after which 19.35 g of TEOS was added to the homogeneous clear solution. The synthesis is carried out in a closed polypropylene bottle. This mixture was left under stirring at 308 K for 24 h, followed by an aging step, alternatively at 50, 80, 100, or 130 °C for 24 h under static conditions (this process is referred to as hydrothermal treatment). The resulting solid products were then filtered and dried for 48 h at 95 °C. For template removal, the as-synthesized silica powders were first shortly slurried in an ethanol-HCl mixture and subsequently calcined at 823 K for 2 h. The KIT-6 produced are referred in this thesis as KIT6-50, KIT6-80, KIT6-100, KIT6-130 in order to report the hydrothermal temperature treatment.

SBA-15

SBA-15 was synthesized according to the method described by Zhao et al.[23] First, 4.0 g of surfactant, Pluronic P123, were dissolved in 30 g of water and 120 g of 2 M hydrochloric acid solution. Then, 8.5 g of TEOS was added. This solution was stirred for 20 h at 308 K and then aged at 353 K overnight, without stirring (hydrothermal treatment). Finally, the product was collected by filtration, washed, and air-dried at room temperature. Calcination was carried out at 873 K (1 K/min) for 6 h. These sample is named as SBA15-C in this work.

Another sample was a commercially available SBA-15 and it was bought from ACS Material (SBA15-ACS).

MSU-H

OMS of MSU-H type were bought from Sigma Aldritch and kindly provided by Formac Pharmaceuticals (MSU-H-F)

DISORDERED MESOPOROUS SILICA

Two porous silica, with trade name Syloid AL-1 FP, were donated from Grace GmbH & Co. These are disordered silica synthesized without the use of any template but with different pore size distribution centred on 1 and 10 nm. Consequently, they were named as Syloid-1 and Syloid-10.

ACTIVE PHARMACEUTICAL INGREDIENT

Amikacin sulfate (AKS) (MW = 781.76 g/mol) (Ph.Eur 8.2) (purity 99,8%) and Clotrimazole (CTZ) (MW = 344.837 g/mol) (purity 98.9%) were

acquired from Sigma Aldritch. They were used as such, without any purification procedure.

CHEMICALS

Carbon dioxide with a purity of 99.5% was supplied by SIAD. Bidistilled water was supplied by J.T.Baker. All the reagents required for OMS synthesis (C_{16}TMABr, TMB, TEOS, etc.), 1-fluoro-2,4-dinitrobenzene (FDNB), 1,2-propandiol, glycerol, acetonitrile and hydroxyethyl cellulose (Natrosol MR) were purchased from Sigma Aldritch. Commercial formulation of AKS (5% by mass) and CTZ (2% by mass) were purchased from a community pharmacy.

CHARACTERIZATION METHODS

X-RAY DIFFRACTION

X-Ray Diffraction (XRD) and wide angles patterns were obtained using a PANAlytical X'Pert Pro (Cu K_α radiation) diffractometer with a PIXcel^{1D} photon detector.

FOURIER TRANSFORM INFRARED SPECTROSCOPY

For Fourier Transform InfraRed (FTIR) measurements, powders were pressed in self-supporting wafers and spectra were recorded at room temperature with a Bruker Tensor 27 spectrometer operating at 2 cm^{-1} resolution. If degassing was necessary, the sample were outgassed at 373 K for one hour (residual pressure equal to 0.1 Pa). FTIR spectrum of crystalline API were recorded on the powder dispersed in potassium bromide (KBr). FTIR spectrum of API dissolved in solution were recorded on a diluted carbon tetrachloride (CCl4) solution (1 g/L).

NITROGEN ADSORPTION

Nitrogen adsorption isotherms were measured using a Quantachrome AUTOSORB-1 instrument after degassing at 373 K for 2 hours. Brauner-Emmet-Teller (BET) specific surface areas (SSA) were calculated in the relative pressure range 0.04-0.1 and the pore size distribution was determined through the NLDFT (Non Linear Density Functional Theory) method, using the NLDFT equilibrium or adsorption model for cylindrical pores.[22]

TERMOGRAVIMETRY

TermoGravimetric (TG) analyses were carried out between 298 K and 1523 K in air (flow rate 100 mL/min with a heating rate of 10 K/min) using a SETARAM 92 instrument.

The API desorption analysis were performed using a SETARAM 92 instrument following the procedure explained by Verevkin et al.[70] and Price et al.[71] Using the Clausius-Clapeyron relation, equation (1), the enthalpies of vaporization (ΔH_{vap}) at the average temperature of investigation were obtained.

$$ln\left(\sqrt{T}\frac{dm}{dt}\right) = A + \frac{\Delta H_{vap}}{RT} \qquad (1)$$

where *dm/dt* is the mass loss rate at the specified temperature; *R* is the universal gas constant and *T* is the temperature of the isothermal experiment. Subsequently, vaporization enthalpies were reported to 298.15 K using general methods of correction, reported by Chickos et al.[72] (the Sidgwick's rule):

$$\Delta H_{vap}(298.15) = \Delta H_{vap}(T) + 0.0545\ (T - 298.15) \qquad (2)$$

In equation (2), *T* is the temperature of measurement or mean temperature of measurement if ΔH_{vap} *(T)* has been obtained from a Clausius-Clapeyron treatment of vapor pressures. The experimental conditions used for the reliable determination of vaporization enthalpies of low volatile molecular compounds are following the references of Verevkin at al.[70] A calibration curve with phenol has been done. The uncertainty of temperature calibration was less than 1 K.

DIFFERENTIAL SCANNING CALORIMETRY

Differential Scanning Calorimetry (DSC) measurements were performed with a DSC1 STAR^e (Mettler Toledo) System apparatus of TA Instruments equipped with a low temperature probe between 298 K and 1073 K under nitrogen flux (flow rate 60 mL·min^{-1} with a heating rate of 10 K·min^{-1}).

SCANNING ELECTRON MICROSCOPY

Field Emission Scanning Electron Microscopy (FESEM) image were recorded with a FESEM ZEISS MERLIN.

DINAMIC LIGHT SCATTERING AND ZETA POTENTIAL

Dinamic Light Scattering (DLS) and Zeta Potential analysis were performed with 90 Plus Instrument (Brookhaven) on a suspended water mixture of OMS after homogenization with a high shear homogenizer (Ultraturrax, Ika) for 5 min at maximum velocity.

NUCLEAR MAGNETIC RESONANCE

Solid State Nuclear Magnetic Resonance (SSNMR) spectra were recorded on a Bruker Avance II 400 instrument operating at 400.23 and 100.65 MHz for ^{1}H and ^{13}C nuclei, respectively. 4 mm o.d. zirconia rotors (sample volume of 80 µL) were employed and spun at 12 kHz for ^{13}C CPMAS spectra. A ramp cross-polarization pulse sequence was used with contact times of 3–5ms, a ^{1}H 90° pulse of 3.8 µs, recycle delays of 1–60 s and 48–4096 transients. ^{1}H MAS spectra were performed on a 2.5 mm probe with a spinning speed of 32 kHz. A DEPTH sequence (π /2-π-π) was used to suppress the probe background signal.[73,74] The ^{1}H 90° pulse length was set to 2.50 πs, the recycle delays to 1-40 s and 32-64 transients were averaged for each sample. ^{1}H and ^{13}C chemical shifts were referenced through the resonance of adamantane (^{1}H signal at 1.87 ppm) and hexamethylbenzene (^{13}C methyl signal at 17.4 ppm), respectively.

DRUG INCORPORATION METHODS

SOLUTION

API incorporation was performed by adsorption from solution. To this purpose, normally, 300 mg of API and 100 mg of OMS were introduced in an Erlenmeyer flask with 5 ml of solvent (water or ethanol) and maintained at room temperature under stirring for 24 hours. Then the powder was filtered and dried overnight in vacuum (residual pressure 0.1 Pa).

INCIPIENT WETNESS IMPREGNATION

The API loading was performed by Incipient Wetness Impregnation (IWI) procedure, based on the capillary action [47]. Typically, 1 ml of a saturated solution of API was added drop by drop to one gram of OMS during

mechanical agitation. The homogeneous wet powder obtained was vacuum dried for 24 hours at 0.1 Pa obtaining a dry powder. For the IWI water and ethanol were used as solvents.

SUPERCRTICAL CO_2

For the incorporation process by means of $scCO_2$ a homemade device was used. This consists in a glass cylinder of 1 cm diameter containing a pellet of CTZ (100 mg) and a pellet of OMS (100 mg) separated by a disc of filter paper, in order to prevent their contact and to separate the pellets after the incorporation process.

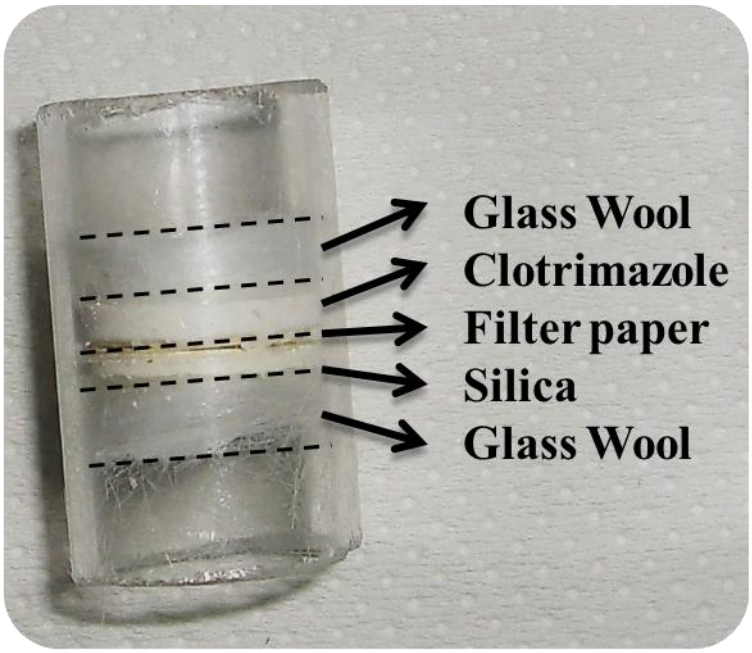

Figure 1.11: Photograph of the homemade device used for the $scCO_2$ incorporation process.

This device was placed inside a stainless steel vessel, which was put in an oven that maintained all the system at constant temperature. The apparatus was also equipped with a volumetric pump and a back pressure

regulator. A scheme of the apparatus is reported in Figure 1.12 and further details can be found elsewhere.[75]

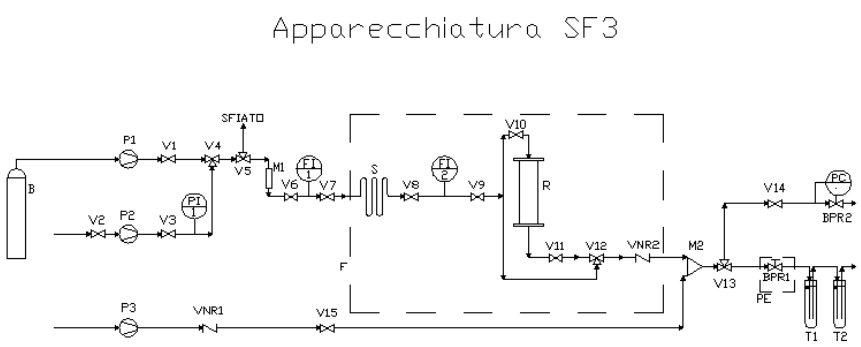

Figure 1.12: $scCO_2$ apparatus details: B – CO_2 tank; P1 – CO_2 pump; P_2 – co-solvent pump (not used); P_3 – hexane pump (not used); V_{xx} – valves On/Off; $V_4/V_5/V_{12}/V_{13}$ three way valves; V_{NR} – not returning valve; R – reactor; M – Mixer; S – heating coils; F – oven; BPR_1 – manual back pressure regulator; BPR_2 – automatic back pressure regulator; PE – heating pad; Tx – trap; Fl_x – mass flow meter.

The incorporation was performed in static condition. The vessel was filled with liquid CO_2 and heated up to 373K. After the heating, additional carbon dioxide was pumped in the vessel to reach the final desired pressure (25.0 MPa). The system was then maintained in the described conditions for several hours (from 6 to 18) to allow the drug dissolution and diffusion into the OMS. At the end of the incorporation process, the temperature was decreased to room conditions and the apparatus was depressurized.

AB-INITIO AND MOLECULAR DYNAMICS SIMULATIONS

All the calculations were performed within the Density Functional Theory (DFT). Concerning static calculations, the developmental version of the

CRYSTAL14 code[29] in its massively parallel version[77] was adopted and the computational approach is the same of Ref.[78]. Briefly, the chosen functional was the Perdew, Burke, and Enzerhof GGA (Generalized Gradient Approximation) exchange-correlation functional (PBE),[31] including the empirical Grimme's D2 correction,[80] to describe the dispersive interactions (vdW). In the following, the superscript D means that Grimme's correction is included. Split valence double- (for Si atoms) and triple-ζ (for other atoms) Gaussian type basis sets plus polarization functions were used to describe the systems.[81,82] Chlorine atoms were represented with a 86-311G* basis set.[83] Only the atomic coordinates of the two more superficial layers of each silica slab in the docking geometries were optimized, to compensate for the reduced thickness of the models. Starting geometries were generated so to maximize the interactions between the drug and the surface. Interaction energies, per unit cell per adsorbate molecule (ΔE), were calculated and corrected for the basis set superposition error (BSSE) according to the counter-poise methodology described in previous papers by Delle Piane et al.[23,25] and reported in Supporting Information.

Harmonic frequencies were calculated with CRYSTAL14 at Γ point and the infrared intensity for each normal mode was obtained by computing the dipole moment variation along the normal mode, adopting the Berry phase method.[85] For the simulation of the IR spectra of the different structures, only a fragment consisting of the most interesting chemical groups has been considered for constructing the Hessian matrix and will be defined for each case in Results and Discussion.

Enthalpies (ΔH) of adsorption at standard temperature (298 K) were obtained from the vibrational partition functions, by applying the Zero Point Energies (ΔZPE) and thermal (ΔE_T) corrections to the BSSE corrected electronic adsorption energies (ΔE^C) as $\Delta H = \Delta E^C + \Delta ZPE + \Delta E_T$.

Ab-initio molecular dynamics (AIMD) simulations were performed using the CP2K code.[86] The Quickstep technique[87] with a mixed plane wave and Gaussian basis set methodology (Gaussian and Plane Wave method, GPW) was employed to calculate the electronic structure. We used the PBE functional, with the Goedecker−Teter−Hutter pseudopotentials[88] and a triple-ζ basis set with polarization functions (TZVP)[89] augmented with the empirical Grimme's D2 correction.[80] The cutoff for the plane wave basis was set to 400 Ry. AIMD simulations were run at 300 K in the NVT ensemble, using the Canonical Sampling through Velocity Rescaling (CSVR) thermostat.[90] A time step of 0.5 fs was chosen. All simulations were equilibrated at 300 K with a more stringent thermostat (time constant: 10 fs) for about 1 ps and then the production phase was run for at least 10 ps with a more relaxed thermostat (time constant: 50 fs). Since CP2K requires 3D periodic systems, a value of c = 35 Å was chosen to separate the slab replicas with enough vacuum. In all cases, only the superficial layer of the silica slab and the drug molecules were allowed to move.

DRUG RELEASE

RELEASE KINETICS

The drug release kinetic of API to the saturated concentration were evaluated in vitro by soaking 100 mg of OMS incorporated by API (OMS-API) in 5 ml of stirred solvent. At different time intervals, a small amount of solution (100 µl) was collected, diluted and analysed through UV–Vis spectrophotometry analysis. To assess the amount of released API a 5-point calibration curve has been obtained.

RESERVOIR EFFECT

The reservoir effect of saturated solution with OMS-API have been evaluated for AKS and CTZ. In a saturated solution of API a certain amount of OMS, impregnated with the same API, were added under agitation. At regular intervals (1h) a small amount of solution (between 500-100 µl) were withdraw and substituted with the same quantity of pure solvent. The extracted solutions were then diluted and analysed through UV–Vis spectrophotometry to assess the API concentration. The addition of pure solvent causes a dilution of the solution and allow us to evaluate the reservoir effect of impregnated OMS. In order to evaluate the correct content of drug in the solution a 5-point calibration curves has been done for CTZ and AKS in the respective solvent. The coefficient of determination was 0.997 for CTZ and 0.995 for AKS, both in the concentration range 0.01-0.1 $mg \cdot ml^{-1}$.

ULTRAVIOLET-VISIBLE SPECTROSCOPY

API concentration in solution were evaluated through UltraViolet Visible (UV-Vis) spectroscopy using a UV-Vis-NIR spectrometer (Cary 5000, Agilent technologies). Each time and for each solution, a 5-point calibration curve has been obtained.

IN VITRO RELEASE

API diffusion from different gels was studied using an apparatus consisting of a vertical glass diffusion cells (Franz cell) of 6.0 mL volume equipped by a Spectra/Por (12000-14000 Dalton MWCO) hydrophilic cellulose membrane (Spectrum Lab). The diffusion area was 2 cm^2. Gels and commercial formulation were employed as a donor phase. The receiving phase consisted of acetate buffer at pH 5.0 (AKS) or water solution of HCl (pH 1.0) (CTZ). The apparatus was maintained under stirring for 72 h at 307 K, during which at scheduled times the receiving phase was withdrawn and entirely substituted with fresh receiving phase.

Each withdrawn was analysed. Each sample was prepared and analysed in triplicate.

IN-VITRO PERMEATION STUDIES

AKS transepidermal permeation and skin uptake from the different gels were studied using vertical Franz diffusion cells and porcine ear skin. Skin slices were isolated using an Acculan dermatome (Aesculap) from the outer side of pig ears freshly obtained from a local slaughterhouse and then stored for at least 24 h at 255 K. Prior to each experiment, the excised skin was rinsed with normal saline solution and pre-hydrated by floating it in 0.002% (w/v) sodium azide aqueous solution. The skin was then sandwiched between the two cells with the stratum corneum side upwards. The diffusion area was 2 cm^2. AKS-OMS gel and commercial formulation were employed as a donor phase. The receiving phase consisted of acetate buffer at pH 5.0. The apparatus was maintained under stirring for 168 h at 307 K, during which at scheduled times the receiving phase was withdrawn and entirely substituted with fresh receiving phase. Each withdrawn was analysed using HPLC. Each sample was prepared and analysed in triplicate.

HIGH PRESSURE LIQUID CHROMATOGRAPHY

AKS was derivatized by mixing 100 µl of aqueous solution of the drug with 300 µl of methanol, 40 µl of NaOH (0.05 M) and 50 µl of a methanolic solution of the derivatizing agent (FDNB) (180 $mg \cdot ml^{-1}$). The obtained mixture was heated at 363 K in an air-circulating oven for 10 min, then cooled and injected in HPLC. Each solution was separately derivatized prior to injection. The HPLC apparatus consisted of an isocratic pump (Series 200, Perkin-Elmer instrument) equipped with a µBondapack C18

300 mm · 4.6 mm column (particle size: 10 µm; pore size: 125 Å; endcapped) (Waters, Milford, MA, USA). The mobile phase was a mixture of acetonitrile–water–acetic acid (47:53:0.1 v/v/v) pumped at 1.5 ml/min. A spectrophotometric detector (LC 290, Perkin-Elmer) working at 365 nm was used.

CHAPTER 1: DRUG INCORPORATION

ABSTRACT

Clotrimazole (CTZ) and Amikacin Sulfate (AKS), two active principles widely used in dermatology, were incorporated inside Ordered Mesoporous Silica (OMS). Three main techniques have been compared: incorporation by solution, incipient wetness impregnation and supercritical CO_2. At the same time six main OMS have been used: MSU-H, MCM41-1 to MCM41-4 and MSU-H-F. In all cases the pristine OMS were characterized by nitrogen adsorption measurement. Numerous incorporation parameters have been studied. The amount of incorporated CTZ was higher with the $scCO_2$ process (34% by mass), while AKS content was higher with the IWI technique (43% by mass). The drug-containing OMS was characterized by XRD, FESEM, TGA, FT-IR and nitrogen adsorption analysis. In all cases the drug resulted amorphous and distributed inside the mesopores.

INTRODUCTION

In the first pioneering work by Vallet-Regi et al.[33], drug incorporation in MCM-41 was carried out by adsorption from a solution using hexane as solvent.

Since the long-term toxicity of n-hexane in humans is well known[91,92], many other solvents have been studied for the incorporation. For instance, Charnay et al.[93] reported that when highly polar solvents such as dimethyl sulfoxide (DMSO), dimethylformamide (DMF) and dimethylacetamide (DMA) were used, the amount of adsorbed drug was limited, whereas a higher quantity of drug was incorporated when ethanol

or hexane were used. The drug incorporation is strongly affected by the solvent due to the competition between the drug and the solvent in the adsorption [93].

An answer could be the IWI process. [47] This technique allows the choice of less dangerous solvents tackling the problems of solvent removal and adsorption competition. Surely, a high drug solubility must be persecuted in order to enhance the drug adsorption efficacy. On the other hand, a repetition of the IWI could be done to enhance the drug content.

Finally, also the incorporation through $scCO_2$ is an alternative way to adsorption or impregnation from a liquid solution. Unfortunately, not all drugs can be solubilized by the CO_2 flow. Even if pressure and temperature can modify the solubility parameter of CO_2, salts like AKS cannot be solubilized.

Belhadj-Ahmed et al. [94] investigated the supercritical impregnation of vitamine E acetate on silica matrixes by means of a dynamic technique. Min et al. studied the incorporation of ibuprofen inside SBA-15 through $scCO_2$ [95], showing that the loaded drug quantity increased with a higher solubility of ibuprofene in $scCO_2$.

The first paragraph of this chapter will discuss the positive aspects of the $scCO_2$ process compared to the incorporation from solution. For the sake of brevity, only OMS of MSU-H type will be presented in this part. CTZ is the model drug and ethanol, for safety reasons, is the selected solvent.

Secondly, the $scCO_2$ process will be replied on the MCM-41 OMSs, 1 to 4.

Thirdly, the IWI method will be studied for AKS in order to compare the two techniques, using two different OMS (MSU-H and MSU-H-F).

1.1 SOLUTION AND $SCCO_2$ PROCESS COMPARISON

The effect of the $scCO_2$ treatment on the structure and morphology of OMS was investigated by means of XRD and FESEM prior to the incorporation of CTZ. The target was to study the possible effects of $scCO_2$ on OMS. There was no literature on this topic.

As it is reported in "Incorporation of clotrimazole in ordered mesoporous silica by supercritical CO_2" by Gignone et al.[8], wide angle XRD patterns and FESEM micrographs showed no significant modifications.

$ScCO_2$ was used to incorporate CTZ using the apparatus showed in the experimental section. Pressure and time of the $scCO_2$ treatment were varied, in order to investigate the effect on the amount of incorporated CTZ, whereas the temperature was maintained constant and equal to 373 K. This temperature was chosen significantly higher than the critical temperature of carbon dioxide, at variance with what was reported by Belhadj-Ahmed et al. [94] and by Min et al. [95]. Thermal degradation of CTZ can be ruled out since it was reported to occur at 453 K.[96] The selected working pressures ensured a good solvent power of the fluid. The density and solubility parameter were respectively equal to 550 $kg \cdot m^{-3}$ and 9.1 $(MJ \cdot m^{-3})^{1/2}$ at 25.0 MPa, while they were 819 $kg \cdot m^{-3}$ and 12.5 $(MJ \cdot m^{-3})^{1/2}$ at 50.0 MPa.

As a whole, four different incorporation procedures were carried out and their typical parameters are summarized in Table 1.1, together with the corresponding loading of incorporated CTZ, which was measured by TG analyses.

Table 1.1: Incorporation process parameters for $scCO_2$ and ethanol solution (EtOH) and corresponding CTZ loading evaluated by TG analysis.

Incorporation Procedure	Time (h)	Temperature (K)	Pressure (MPa)	Drug-OMS ratio*	Loading (%)
$scCO_2$ -1	6	373	25.0	1:1	12
$scCO_2$ -2	12	373	25.0	1:1	30
$scCO_2$ -3	12	373	50.0	1:1	34
$scCO_2$ -4	18	373	25.0	1:1	30
EtOH	24	298	0.1	3:1	9.0

*mass ratio

The maximum amount of incorporated CTZ, corresponding to 34% by mass, was obtained at 50.0 MPa after a 12-hours-supercritical treatment.

Data in Table 1.1 reveal that time plays a crucial role up to 12 hours. In fact, the CTZ loading increased from 12% to 30% by mass when time increased from 6 to 12 hours at 25.0 MPa, whereas no further increase was observed when the process was carried out for a longer time, i.e. 18 hours, at the same pressure. These data suggest that after 12 hours the equilibrium between CTZ in $scCO_2$ and CTZ inside the MSU-H was reached.

At variance, pressure was observed to affect the incorporated amount only at a minor extent, since an increase from 25.0 MPa to 50.0 MPa yields a limited increase of the CTZ percentage (from 30% to 34%), probably due to a higher solubility of CTZ in $scCO_2$ at higher pressure.

It is worth noting that the incorporation via $scCO_2$ was largely more efficient than that obtained by adsorption from ethanol solution. In fact, in the latter case the percentage of CTZ inside MSU-H was only 9.0%.

Moreover, the amount of CTZ used for the adsorption was three times higher than that of MSU-H, at variance with the $scCO_2$ treatment for which the same amounts of CTZ and MSU-H were used.

As already reported[8] CTZ is maintained in an amorphous state. The lack of crystallization is crucial, because amorphous drugs are widely accepted to have higher aqueous solubility and dissolution rate than related crystalline phases. This effect may be particularly important when molecules poorly soluble in water, such as CTZ, are considered.[41,97,98] FT-IR spectroscopy, nitrogen adsorption measurements and TG analysis on this samples showed important details of the CTZ distribution; but this correlation will be discussed altogether in the following chapters.

1.2 MCM-41 $SCCO_2$ INCORPORATION

MCM-41 silicas have been widely studied used as drug carrier. During this research work, through the solution technique, the maximum CTZ content was about 6% by mass without residue mesoporosity. These data are different from the MSU-H case, see table 2.1.

In this case four MCM-41 have been synthesized, as already described, and characterized.

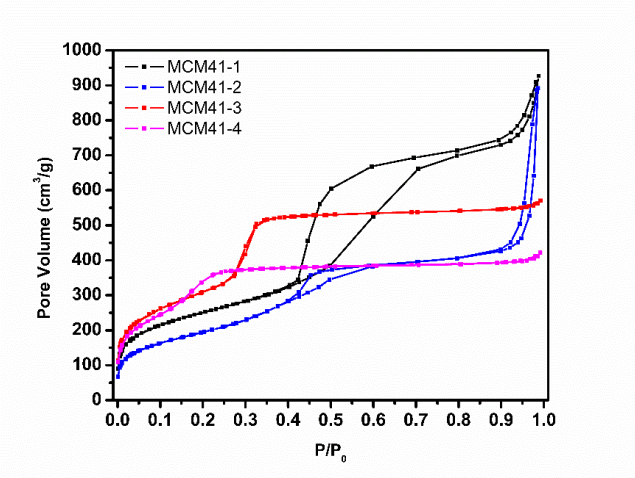

Figure 1.1: MCM-41 nitrogen adsorption isotherms. Pore volume, SSA and PSD are reported in chapter 2.

Table 1.2: MCM-41 nitrogen adsorption results

OMS	Mean pore diameter (nm)	NLDFT SSA (m^2g^{-1})	NLDFT Volume (cm^3g^{-1})
MCM41-1	4.88	812	1.286
MCM41-2	4.88	585	1.100
MCM41-3	3.65	930	0.818
MCM41-4	2.94	840	0.598

The nitrogen adsorption analysis showed a good SSA and pore volume.

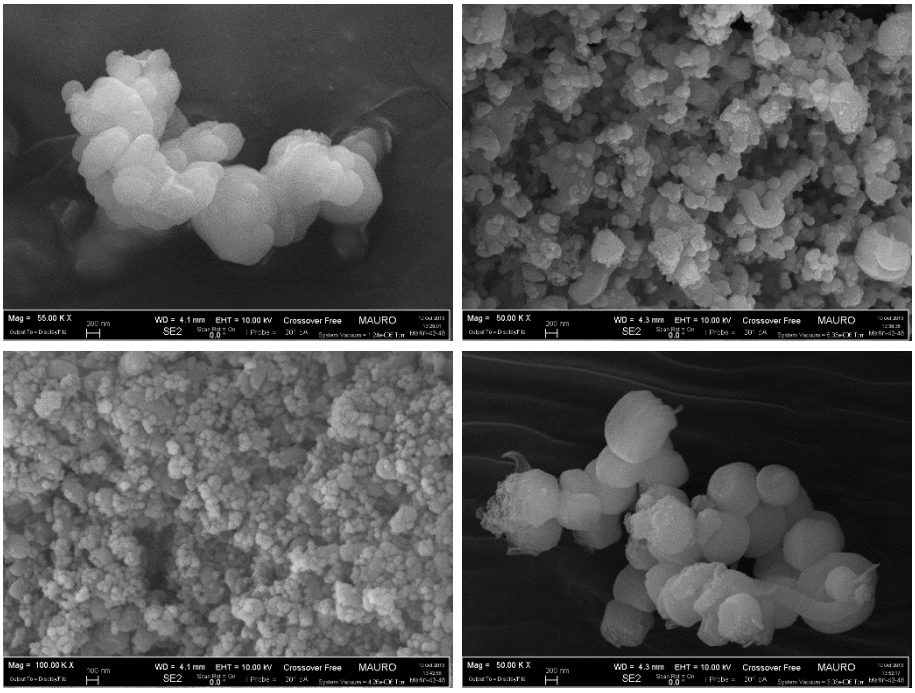

Figure 1.2: MCM-41 FESEM images. In the upper left image MCM41-1 is showed (mean particles size 360 nm). Upper right, MCM41-2 (210 nm). Lower left, MCM41-3 (100 nm). Finally, MCM41-4 (1090 nm).

The drug content with the $scCO_2$ was higher than for the MSU-H case. The higher loading was obtained with MCM41-1 with a CTZ content of 44% by mass. XRD and FTIR analysis reported a complete amorphization of the drug.

1.3 AMIKACIN SULFATE INCORPORATION

The drug loading was performed by the solution method and the IWI procedure. In the first case, 300 mg of AKS where solubilized in 5 ml of H_2O and stirred for 24h with 100 mg of MSU-H-F. The water content was removed trough filtration and drying. For IWI, typically, 1 ml of a water

saturated solution of AKS was added drop by drop to one gram of MSU-H-F (0.898 $cm^3 \cdot g^{-1}$) during mechanical agitation. The homogeneous wet powder obtained was vacuum dried for 24 hours to 0.1 Pa obtaining a dry powder.

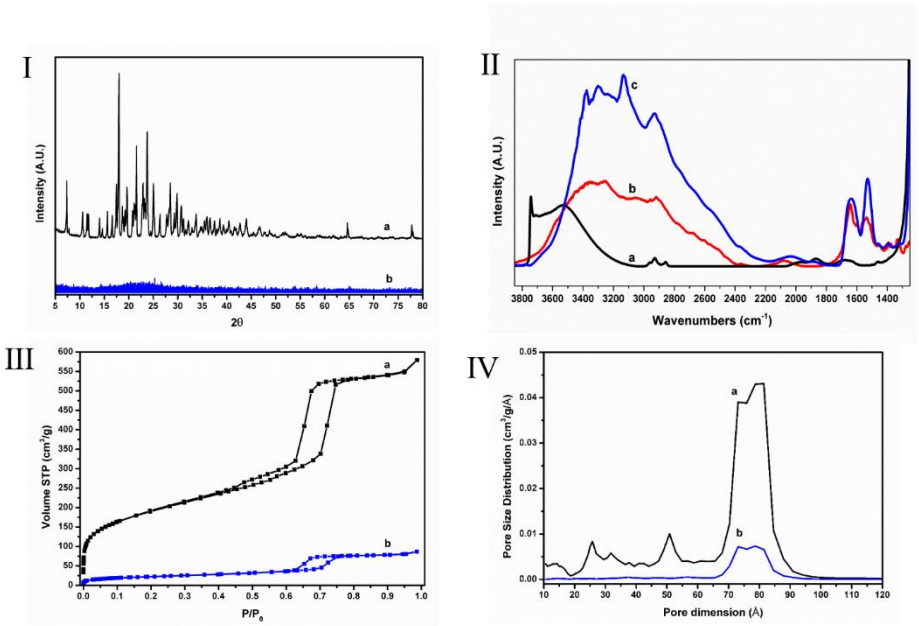

Figure 1.3: (I) XRD spectra of AKS powder (a) and MSU-H-F-AKS (47% by mass) (b). (II) FTIR spectra of MSU-H-F (a), AKS in KBr (b) and MSU-H-F-AKS (c). (III-IV) N_2 isotherms and PSD of MSU-H-F (a) and MSU-H-F-AKS (47% by mass) (b).

In order to control the physicochemical properties of our samples, a complete characterization of all samples has been done. XRD results shown a complete amorphization of APIs (Figure 1.3). The lack of crystallization in these materials is a very well reported and crucial phenomenon [40,99,100]. Indeed, such application that require a dissolution and diffusion rate in gels able to overcome the skin absorption it is even more essential; i.e. crystalline APIs could have a dissolution rate too slow in order to maintain the saturation point.

In figure 1.4 are shown the low angle XRD diffraction pattern presenting the typical (100), (110) and (200) peaks, related to the ordered hexagonal (P6mm) network of mesopores. The maintenance of the peaks after the incorporation process demostrate the mesostructure preservation. The differences in the peak intensity indicate the drug incorporation: less density differences from the silica wall to the mesoporous pore core due to the incorporated AKS reduce the intensity of the diffracted X-ray.

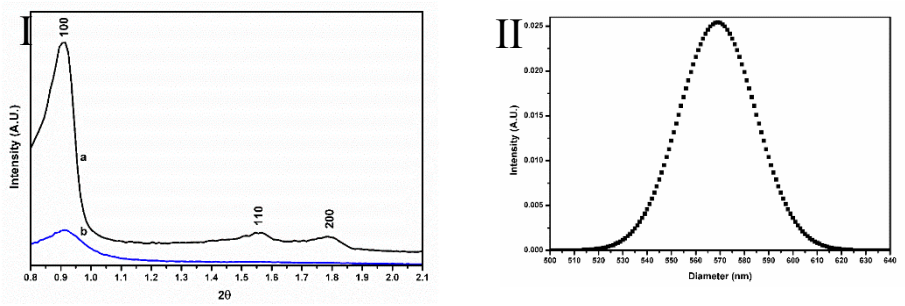

Figure 1.4: (I) Low angle XRD spectra of MSU-H-F (a) and MSU-H-F-AKS (47% by mass) (b). (II) DLS of MSU-H-F after 5 minute of high shear homogenization (30 krpm)

FTIR spectroscopy reveals that the APIs interact with the silica surface through Hydrogen bonds with silanols. The adsorption infrared spectra of figure 1.3.II describes direct interaction between MSU-H-F and AKS. The MSU-H-F as such shows two main band: free silanols at 3742 cm^{-1} and interacting silanols at 3520 cm^{-1}. The 2800-3000 cm^{-1} bands are the alkyl residual chain of the template after the calcination step required to produce MSU-H-F. AKS in KBr shows low adsorption between 3550 and 3160 cm^{-1} (-NH_2, -NH, -OH groups), 2927 and 2850 cm^{-1} (CH_2, CH groups) and strong mode at 1640 and 1550 cm^{-1} (-CONH- group) [67]. Other adsorption band of -CO group are under the silica cut-off. In the MSU-H-F-AKS sample no free silanols are observable (3742 cm^{-1}) suggesting a direct interaction between surface silanols and AKS. Moreover, some new broad absorption band are observable in

comparison with AKS in KBr. These are attributed to SiOH interacting with different groups of AKS.

TG analysis reports the API-incorporated quantities. UV-Vis spectroscopy results and HPLC quantification confirms these results. The TG measurements show in the best case (IWI) an incorporated quantity of 47% by mass, while with the incorporation by solution it was possible to reach only a 15% by mass.

Nitrogen adsorption isotherms (Figure 1.3.III) return the specific surface area, the specific pore volume and the pore size distribution of MSU-H-F and MSU-H-F-AKS (Figure 1.6.IV). In the case of IWI, NLDFT specific surface area decreased from 625 $m^2 \cdot g^{-1}$ to 69 $m^2 \cdot g^{-1}$. The pore volume decreased from 0.898 $cm^3 \cdot g^{-1}$ to 0,121 $cm^3 \cdot g^{-1}$. Using the TG analysis results, the volume excluded from N_2 adsorption, due to the incorporation of AKS in MSU-H-F, can be corrected, as already showed in a previous paper.[8] Dividing the API incorporated quantity with this corrected excluded volume the estimation of the amorphous AKS density is: 1.59 $g \cdot cm^{-3}$. The experimental density of crystalline AKS, evaluated with a helium pycnometer (Ultrapyc 1200e of Quantachrome) is 1.60 $g \cdot cm^{-3}$ that is in agreement with the unique literature data of Bau et al. [101], to the best of our knowledge. This correlation shows that AKS have almost the same density in the amorphous and crystalline state. In addition to this, the NLDFT PSDs show a reduction of the volume without a change in pore diameter (Figure 1.3.IV). These considerations, compared to other literature results [99], strongly suggest that AKS molecules are incorporated inside the mesopores but not uniformly distributed on the MSU-H-F surface. Consequently, with the IWI method, the homogeneity inside the mesopores is lost but no occlusion is present and the drug still in an amorphous state. This results are confirmed also with the incorporation by solution, but the incorporated quantity is much lower. On

the other hand, as observable in chapter 2, the $scCO_2$ process is able to homogenize the adsorbed drug.

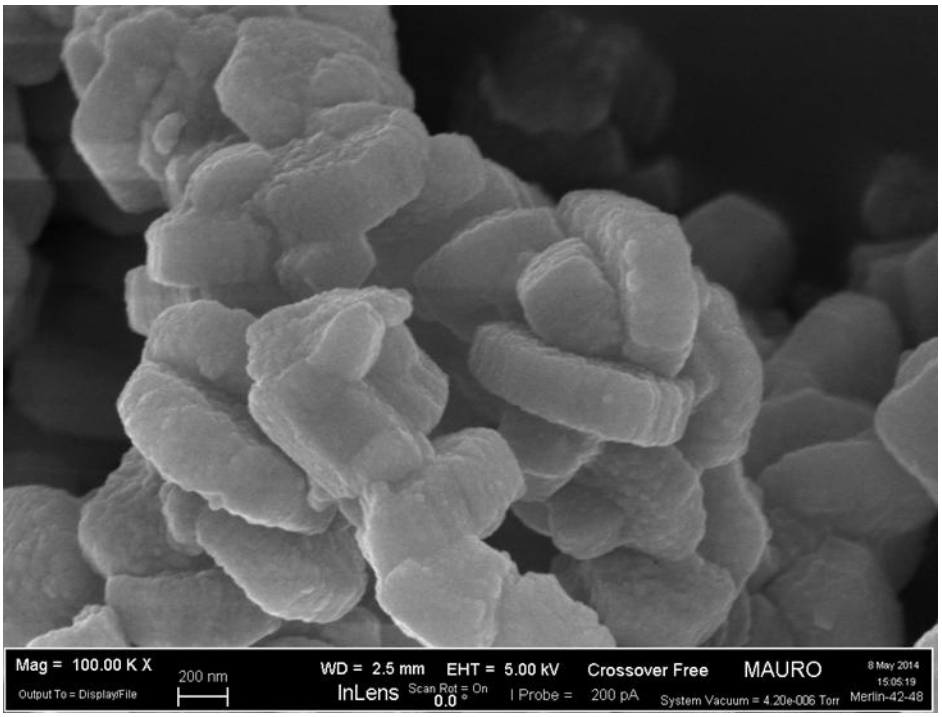

Figure 1.5: FESEM images of MSU-H-F aggregates.

Figure 1.5 reports a morphological image of MSU-H-F showing aggregates of microns composed by particles of about 500-600 nm. The primary particles resemble short prism of hexagonal base with striping along the height recalling the ordered hexagonal (P6mm) symmetry. The DLS measurements of MSU-H-F as such agree with the FESEM image, resulting in aggregates of 1300 nm mean value. Indeed, after high shear homogenization (5 min at 30 krpm), MSU-H-F particles results completely disaggregates (Figure 1.6.II). The mean value is 569±16 nm. The Zeta Potential measurements show an instability of the mixture (-12 mV) but the probable re-aggregation should be avoided in a future gel use due to viscosity.

The ions extracted from the MSU-H-F of MSU-H type were Cl^-, F^-, NO_3^- and SO_4^{2-}. Sulfate is the only one over 2 ppm (18 ppm). This is not a problem since the API used for in-vitro permeation studies is AKS.

CHAPTER 2: CLOTRIMAZOLE CHARACTERIZATION IN MSU-H & MCM-41

ABSTRACT

The knowledge of the specific interactions between the surface of mesoporous silica and drugs is necessary to guide development of new and improved drug delivery systems. However, such knowledge is still scarce, due to the arduous interpretation of experimental results. This chapter reports the complete characterization of the interaction of CTZ, inside OMS by means of a joint computational and experimental approach. Experimentally the drug was loaded through $scCO_2$ in MSU-H and MCM-41. Its adsorption was investigated through FTIR, N_2 adsorption measurements, TG analysis, SSNMR spectroscopy. Modelling involved static and dynamic Density Functional Theory simulations of CTZ adsorbed on realistic models of amorphous silica surfaces. In the first part, a more simplified approach is reported. The second part informs about the agreement between the computational and experimental results, concerning the energies of adsorption, the IR spectra and the distribution of drug inside the mesopores. Finally, a tentative description of the mobility at room temperature of CTZ on the silica surface was done using molecular dynamics simulations and SSNMR results.

2.1 DRUG DISTRIBUTION TYPES IN OMS

On the same sample of chapter 1 (MSU-H and MCM-41), nitrogen adsorption isotherms were measured to characterize the SSA, the specific pore volume and the PSD of OMS as such and OMS-CTZ. In figure 2.1

are reported the adsorption and desorption branches for OMS and OMS-CTZ.

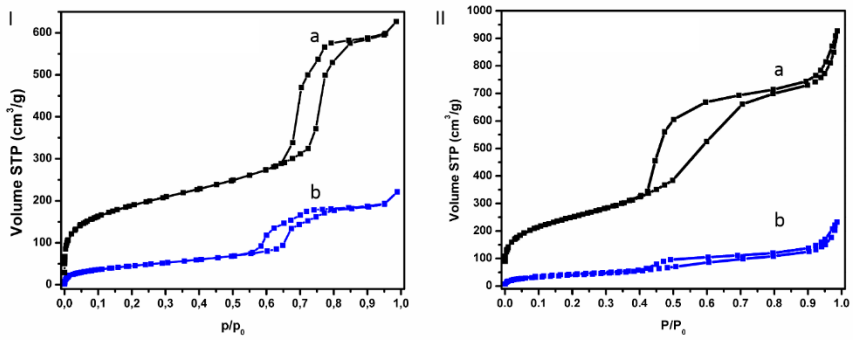

Figure 2.1: Isotherms of MSU-H (I) and MCM41-1 (II) before (a) and after (b) $scCO_2$.

Table 2.1: NLDFT and TGA elaborated data of the isotherms of figure 2.1

Sample	***SSA [m^2/g]***	***Volume [cm^3/g]***	***Loading [g_{CTZ}/g_{TOT}]***	***Residual Volume [cm^3/g]***
MCM41-1	813	1.28	46 %	0.29
MSU-H	597	0.90	34 %	0.32

As already described in a published article[8], from the grams of CTZ incorporated inside the sample, the volume occupied by CTZ can be calculated and the residual free mesopore volume in OMS-CTZ can be estimated. This estimation is strongly affected by the density considered for CTZ in the calculation. Assuming a density of 1.316 g/cm^3,[66] the mesopore volume in OMS-CTZ resulted equal to 0.336 cm^3/g. This value is in fair agreement with table 2.1. The discrepancy of 0.047 cm^3/g may arise from the value of CTZ density used in the calculation. Indeed, XRD pattern showed that CTZ in OMS lacks of crystalline form and its density

is likely to be lower than that of the crystalline phase. These considerations can be repeated for the MCM41-1 sample.

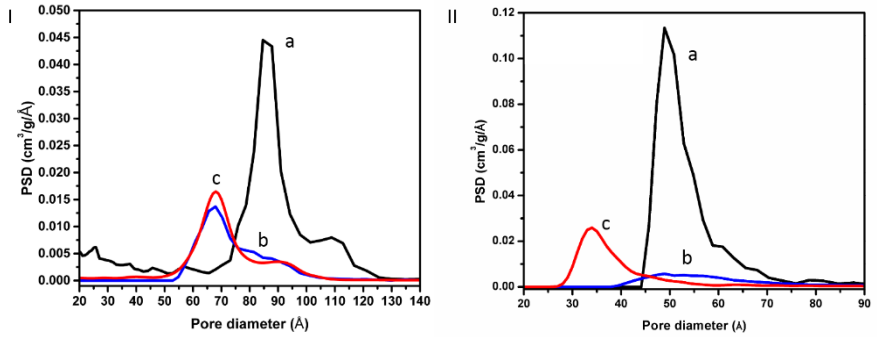

Figure 2.2: PSDs of MSU-H (I) and MCM41-1 (II) before (a) and after (b) $scCO_2$. The red curve (c) reports the mathematical model calculations.

Observing the PSDs reported in figure 2.2, obtained from the nitrogen sorption isotherms of figure 2.1, it can be said that, for OMS as such (a) a main family of pores with an average diameter of 8.5 nm and 5.0 nm are observable. On the other hand, after $scCO_2$ (b), these families of pores are not anymore present.

In the case of MSU-H, the presence of smaller mesopores, could describe a phenomenon of internal coverage of mesopores surfaces by CTZ molecules. Consequently, an attempt has been made to model the occupation of mesopores as a layer of CTZ molecules. The volume V_0 of a single cylindrical empty mesopore is given by

(1) $$\boldsymbol{V_0 = \frac{\pi}{4} \cdot d_0^{\,2} \cdot h}$$

where d_0 is the mesopore diameter and h is the mesopore elongation. The volume V_1 of a single cylindrical mesopore occupied by the clotrimazole layer is given by

(2) $$V_1 = \frac{\pi}{4} \cdot {d_1}^2 \cdot h$$

where d_1 is calculated as

(3) $$d_1 = d_0 - 2d_{clo}$$

and d_{clo} is the diameter of a clotrimazole molecule considered as a sphere. Combining equation 1 and 2, equation 4 is obtained, which, substituting d_1 as in equation 3, gives rise to equation 5.

(4) $$\frac{V_0}{V_1} = \frac{{d_0}^2}{{d_1}^2}$$

(5) $$V_1 = \frac{(d_0 - 2d_{clo})^2}{{d_0}^2} \cdot V_0$$

A new pore size distribution can be calculated from this equation, on the basis of the values of V_0 and d_0 of the pore size distribution of OMS as such (Figure 6a), experimentally obtained by the nitrogen adsorption isotherm. In order to do so, V_0 and V_1 in equation 5 have to be normalized to the same quantity of silica, because V_0 is a specific pore volume, expressed in $cm^3 \cdot g^{-1}$. This means that, if g_{sil} is the amount of OMS as such (silica), the amount of OMS-CTZ is g_{sil} + g_{clo}, where g_{clo} has been evaluated by TG analysis. Accordingly, equation 5 is rewritten as equation 6.

(6) $$V_1 = \frac{(d_0 - 2d_{clo})^2}{d_0^2} \cdot V_0 \cdot \frac{g_{sil}}{g_{sil}+g_{clo}}$$

This calculation is based on a simple modelization of CTZ molecules equally distributed inside MSU-H pores. Figure 2.3 represents schematically the above considered type of adsorption.

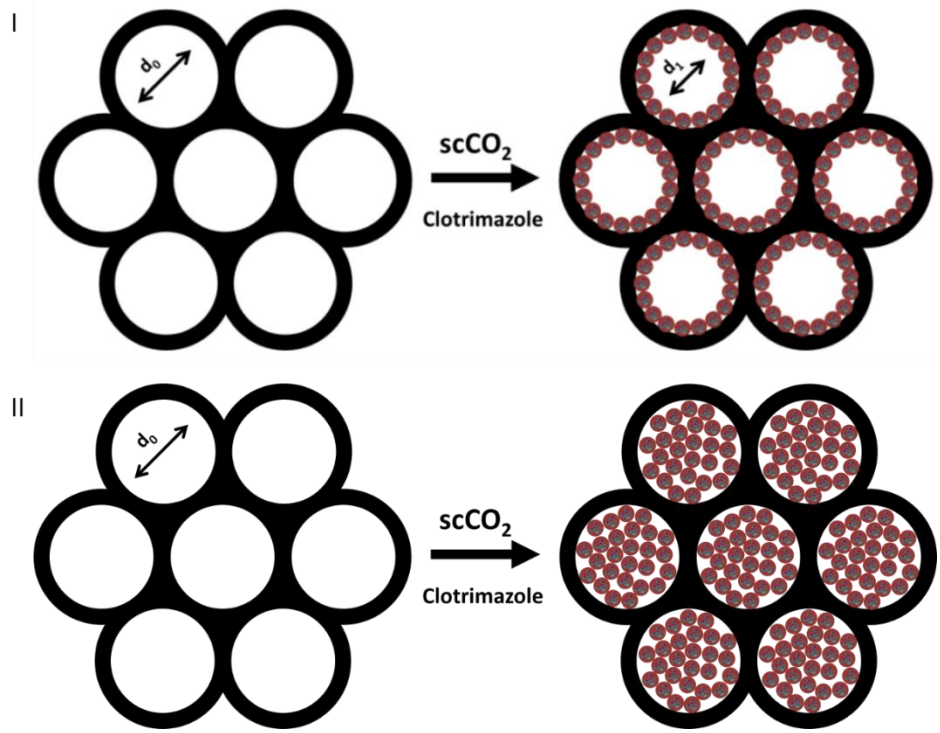

Figure 2.3: Pictorial representation of CTZ adsorption in mesopores; MSU-H (I) and MCM41-1 (II).

Using these assumptions, from the PSD of OMS as such a theoretical PSD, after the adsorption of drug, can be calculated. This is in agreement with previous data reported for itraconazole by Mellaerts et al.,[48] who observed a molecular dispersion of the drug in OMS.

On the other hand, these simplified distributions do not take into account roughness, density profiles and curvature of the channels surfaces.[102]

Consequently, a more detailed description have been done later in this chapter with the theoretical help.

In the case of MCM41-1, due to the fact that there is no residual PSD after the scCO2 process (Figure 2.2), these considerations are not valid. Indeed, the connection between nitrogen adsorption data and TG analysis demonstrate a complete filling of the mesopore channels. A detailed description will be reported in chapter 3. In any case, figure 2.3.II reports pictorially these differences.

2.2 EXPERIMENTAL AND THEORETICAL DATA

In order to describe better the drug-silica interactions the MSU-H and MCM41-1 incorporated samples were used as models, joining experimental and theoretical data. This work was done in collaboration with the Theoretical Chemistry Group of Prof. Piero Ugliengo, with Dr. Massimo delle Piane and Dr. Marta Corno.

CLOTRIMAZOLE: MOLECULE AND CRYSTAL

CTZ was modeled both in gas phase and as a crystal, before studying its adsorption on amorphous silica. The starting point was the X-ray experimental structure by Song et al.[66]

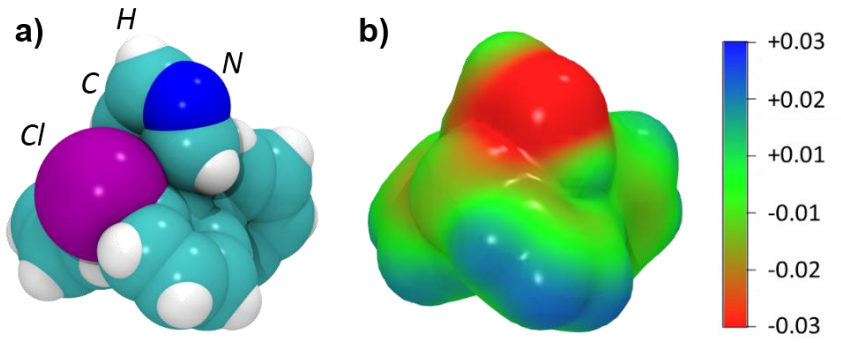

Figure 2.4: a) 3D space filling model of the CTZ tetrahedral. b) CTZ electrostatic potential mapped on the electron density.

The CTZ crystal has been optimized with and without Grimme's correction and compared to experimental results (Figure 2.5).

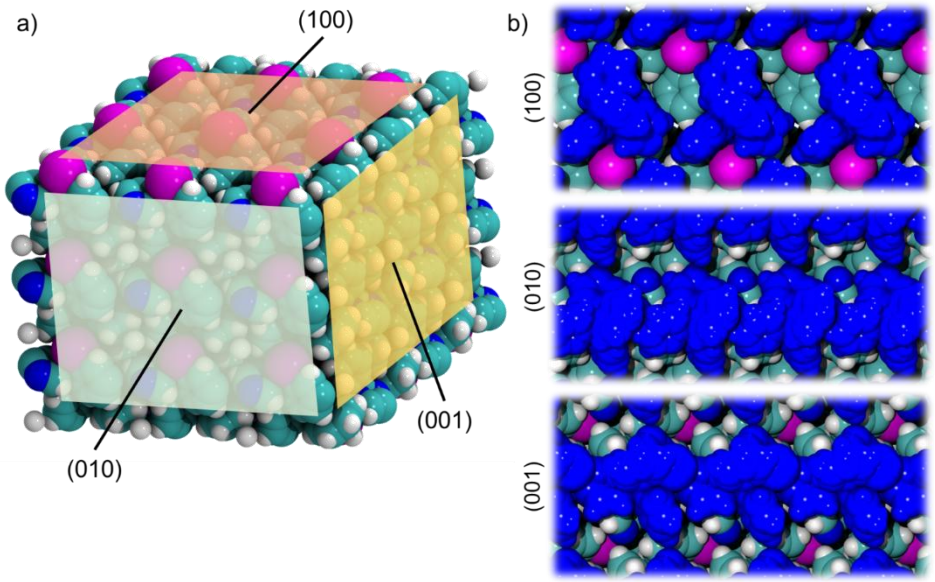

Figure 2.5: CTZ crystal and molecule-faces interactions: a, CTZ crystal with highlighted faces. b, c and d are the PBE-D2 optimized structures of (100) (010) and (001) crystal surfaces with one CTZ molecule per cell adsorbed, respectively. The added molecule is in blue to distinguish it from the clotrimazole crystal slab.

The structure is triclinic with two drug molecules per unit cell. The PBE-D2 cohesive energy of crystalline CTZ has been computed as -146.5 kJ·mol^{-1} (Table 1) and, unsurprisingly, the interactions occurring in the crystal are dominated by dispersion (78%).

Experimentally, the lack of crystallization of CTZ inside OMS is observed. This phenomenon has been described in literature both as a confinement effect[41,98,103,104] and as a competition between crystal cohesion and adsorption on the silica surface.[23] To describe this competition, we have modelled the interaction of CTZ molecules with three crystalline surfaces of the same CTZ crystal, figure 2.5. The added CTZ molecule maximizes the contact with the surface molecules mainly through dispersion and electrostatics interactions. Unsurprisingly, the interaction energies of CTZ with its crystal surfaces are comparable to each other with an average value of -113 kJ·mol^{-1}, lower than the crystal cohesive energy (-132 kJ·mol^{-1}). Experimental TG desorption analysis of crystalline CTZ shows an experimental enthalpy of vaporization of about 92 kJ·mol^{-1}, reasonably close to the theoretical values. The comparison between computed and experimental cohesive energy for the CTZ crystal shows some overestimation due to the PBE-D2 method.

CLOTRIMAZOLE ADSORPTION ON THE SILICA PORE WALL

Experimentally, CTZ was loaded into MSU-H through $scCO_2$, achieving a maximum drug loading of 34% by mass.

In the simulations, CTZ was adsorbed on a silica surface model described in a previous study by some of us.[105] This surface exhibits a silanol density of 4.5 OH·nm^{-2}, close to the experimentally measured value for fully hydroxylated surfaces (4.9 OH·nm^{-2}).[106] Of these silanols, only one is free, while the others are interacting through H-bonds. Particularly, three SiOHs cooperates in forming a stable H-bonded chain.

CTZ was manually docked on the surface, aiming at maximizing the interactions between exposed silanols and the different drug's functional groups. In order to match the experimental conditions, six main starting geometries have been studied. Four of them are characterized by one molecule per silica unit cell (drug loading ~13% by mass), while the other two simulate a molecular layer as observed in previous results[8] with two and three molecules per unit cell (drug loading ~27% and ~41% by mass, respectively) (Figure 2.6).

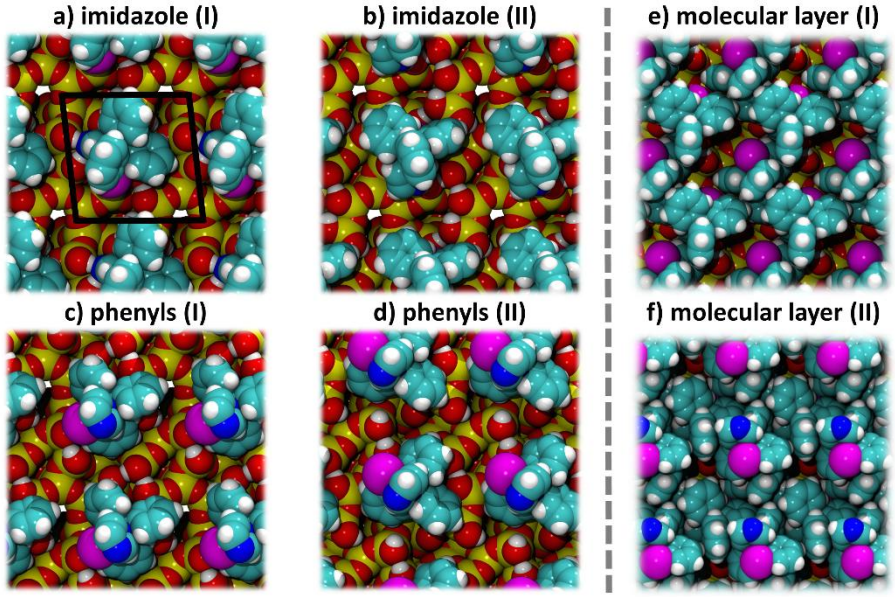

Figure 2.6: View along the z axis of the fully optimized six different geometries of adsorption. a) imidazole (I). b) imidazole (II). c) phenyls (I). d) phenyls (II). e) molecular layer (I): two molecules per silica unit cell. f) molecular layer (II): three molecules per unit cell.

INTERACTIONS AND ENERGETICS BETWEEN CLOTRIMAZOLE AND THE SILICA PORE WALL

From all the six geometries of figure 2.6, four main types of interaction between CTZ and silanols are observable, figure 2.7. The imidazole ring

can form both two (Figure 2.7.a) and one (Figure 2.7.b) H-bonds with the surface. H-bonds of the Si-O-H---Cl type (Figure 2.7.c) are weaker than those with imidazole. Several SiOH-π (surface-CTZ, Figure 2.7.d) have been observed in almost all the different structures, while π-π edge to face lateral interactions (CTZ-CTZ) characterize the molecular layer models.

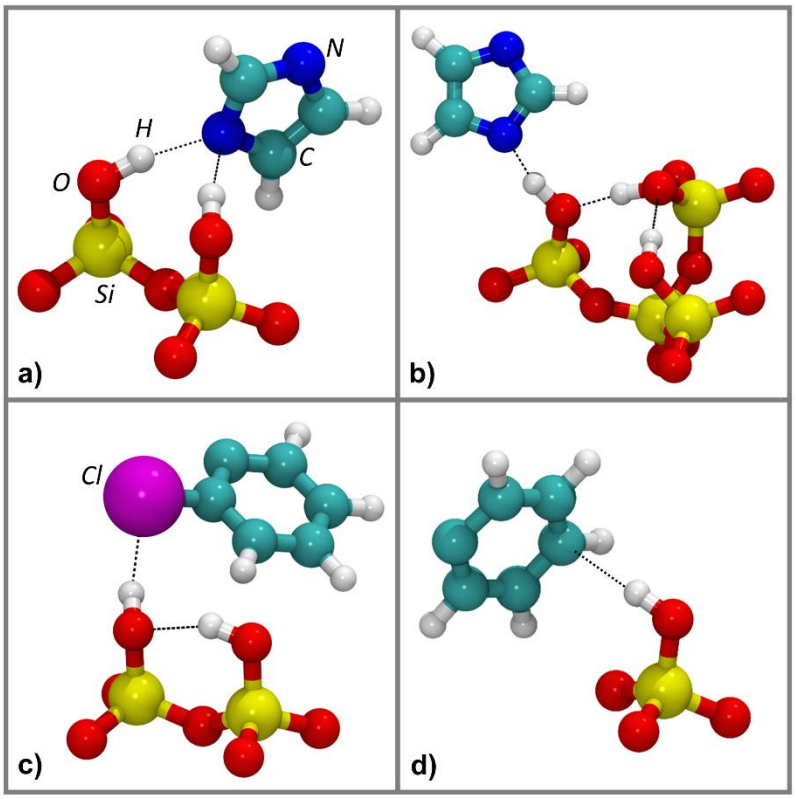

Figure 2.7: Silica-CTZ types of interactions.

An essential result that these considerations reveal is that all the computed interaction energies and enthalpies are close to each other, enlightening a possible competition between crystalline and adsorbed CTZ. Assuming that the supercritical incorporation is a step route controlled by dissolution and adsorption of single molecules, this process is almost isoenergetic, since for each adsorption on silica an average of 110 $kJ \cdot mol^{-1}$ are gained and for each desorption from the crystal 115

kJ·mol^{-1} are lost. This could be the explanation of the lack of crystallization in pores smaller than 20 times the molecule diameter explained by Sliwinska-Bartkowiak et al.[103] and observed by other authors.[41,98,104] In addition TG desorption analysis of CTZ in MSU-H (34% by mass) produces an enthalpy of vaporization of 91.6 kJ·mol^{-1}. As abovementioned, a similar analysis on crystalline CTZ results in a value of 91.8 kJ·mol^{-1}. Thus, also the experimental data suggest that the two processes are almost isoenergetic, supporting the hypothesis on silica-induced drug amorphization.

MODEL OF ADSORPTION: NITROGEN ADSORPTION AND TG ANALYSIS

As previously described, from the experimental N_2 adsorption isotherms, the PSDs, before and after the $scCO_2$ incorporation of CTZ, can be obtained. These show that the drug incorporation reduces the mean pore diameter from 86 Å of bare MSU-H to a lower value of 67 Å (figure 2.2). Clearly, with the above mentioned approach, the calculated PSDs are unable to describe correctly the experimental results.[8]

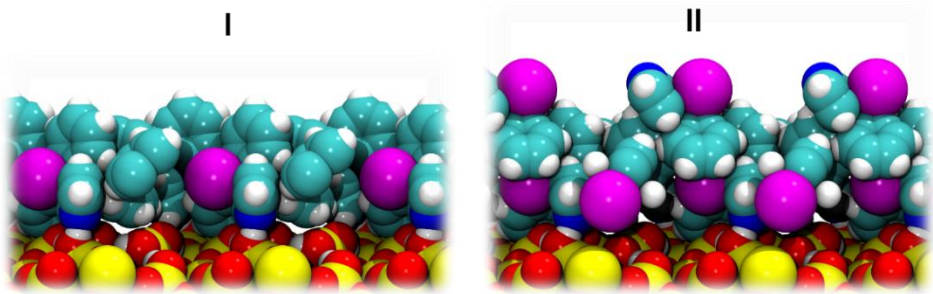

Figure 2.8: Adsorption model. (I) and (II) side views along the a direction of molecular layers (I) and (II), respectively.

On the other hand, experimental TG analysis reports an incorporated quantity of 34% by mass, which is in between the loading calculated for layer (I) and layer (II), which are ~27% and ~41% by mass, respectively.

By calculating the experimental planar concentration of CTZ (molecules per nm^2) and comparing it to our theoretical models of molecular layers (2 CTZs/cell, Figure 2.6.e and 3 CTZs/cell, Figure 2.6.f), it is shown that the real system can be described by a 50:50 mixture of the two molecular layer geometries. Indeed, the unit cell of the simulated silica surface has an area of 1.6 nm^2 and the experiment reports 2.5 CTZ molecules per 1.6 nm^2. As a consequence, a simulated MSU-H-CTZ PSD has to be calculated, starting from the experimental PSD of bare MSU-H, assuming thicknesses representative of both the molecular layer (I) and (II) models. These thicknesses have been evaluated following the Connolly surfaces[107] before and after CTZ adsorption of the computed models, with the purpose to take into account the vdW molecular volume and the roughness generated by the statistical distribution of 2 and 3 CTZ molecules per 1.6 nm^2. Therefore, the molecular layer surfaces have been discretized in 677 squares (0.25 $Å^2$) in order to evaluate the thicknesses, for each point, between the starting silica model and the molecular layers. Subsequently, a new PSD has been calculated for each couple of evaluated thicknesses and all curves have been combined together in the final theoretical PSD of figure 2.2.I.c. Such procedure results in an impressive agreement between simulation and experiment, validating the data interpretation.

INCREASING THE CTZ ADSORBED QUANTITY

Due to the prefect agreement of this modelization, three different samples with increasing fillings were prepared using $scCO_2$ process. The aim was to obtain information on CTZ interaction with silica pore wall at increasing loading. Through XRD analysis it was possible to evaluate the presence or not of CTZ crystals. None of the samples show diffraction peaks of CTZ.

Nitrogen adsorption isotherms, figure 2.9, evidence a linear decrease in comparison to the loaded quantity of SSA and pore volume. In table 2.3 are reported the detailed values. To the best of our knowledge, the only literature crystalline CTZ density data is a calculated number reported in the work of H. Song et al.[66] Using a helium picnometer, a value of 1.31 $g \cdot cm^{-3}$ has been obtained, in perfect agreement with the literature data. Interestingly the calculated CTZ density inside the mesopore, reported in Table 2.3, increase with the loading but never reach the crystalline number. As already demonstrated, the CTZ is amorphous but the linear increase of density with the loaded quantity could be due to a decreasing pore occlusion. In addition to this, as evidenced by the position and shape of the hysteresis loop, the mean pore diameter of the mesoporous channels decrease with the formation of the CTZ layer.

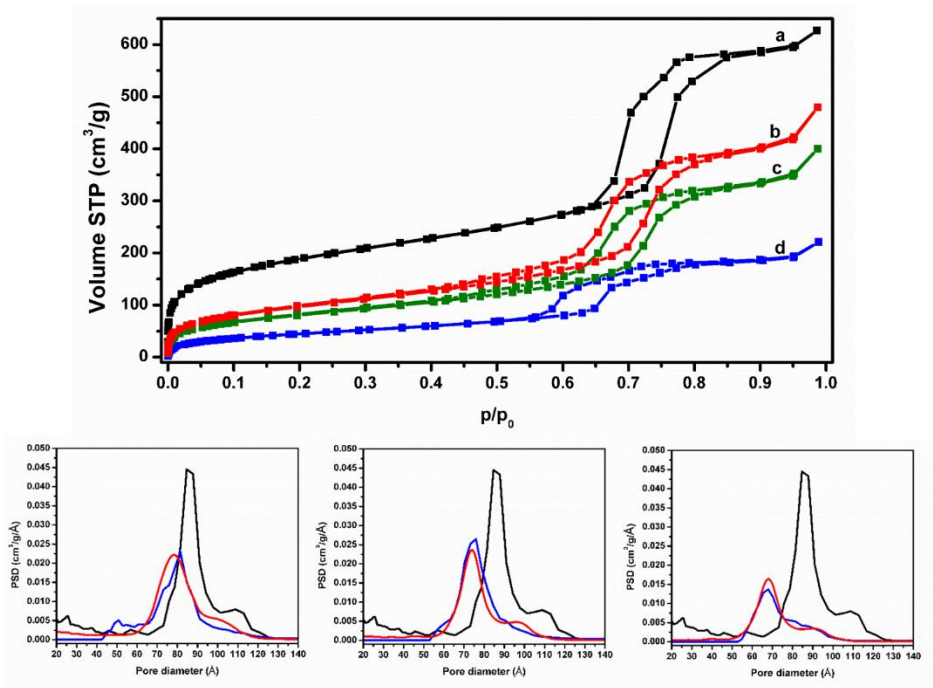

Figure 2.9: Nitrogen adsorption isotherms of bare MSU-H (a), MSU-H-CTZ-12 (b), MSU-H-CTZ-18 (c) and MSU-H-CTZ-34 (d). Below the PSD of bare MSU-H (black) in comparison to MSU-H-CTZ samples (blue); the red curve is

the theoretical PSD corresponding to the experimental loading; from left to right: MSU-H-CTZ-12, MSU-H-CTZ-18 and MSU-H-CTZ-34.

Through NLDFT the PSD of all samples have been calculated. Hypothesizing the adsorption of CTZ as a step process of single molecules that lead to the formation of a layer on the silica wall, the experimental PSD of MSU-H-CTZ can be calculated.[99] In order to evaluate the theoretical PSD of figure 2.9 (red), the theoretical docking structure previously described have been used. The same procedure has been changed with some correction in order to take into account the low loading configuration. Briefly, a new PSD has been calculated for each couple of evaluated thicknesses and all curves have been combined together in the final theoretical PSD representative of each different loading (red). For instance, to evaluate the theoretical PSD of MSU-H-CTZ-12, the four single docking geometries (Imidazole (I) and (II), phenyls (I) and (II)) combined to two clear silica surface (Silica as such) have been used as starting thicknesses, resulting in 4056 point of thicknesses. Then, more than 16 million of new PSD, one for each couple of thickness, have been calculated from the PSD of bare MSU-H and combined together in the left red curve of figure 2.9. The use of two clear silica surface is required to obtain the correct planar concentration of CTZ. As it is reported in table 2.3 a loading of 12% by mass corresponds to a surface coverage of 0.4 CTZ·Å^{-2}, that can be expressed using the theoretical model in a 0.64 CTZ molecule per silica unit cell.

Table 2.3: Nitrogen adsorption and TG numerical results compared to theoretical data

Samples	Pore volume[a]	Loaded quantity[b]	CTZ experimental density[c]	CTZ·1.606 nm^{-2} [d]
MSU-H	0.900	-	-	-

MSU-H-CTZ-12	0.650	12	1.0	0.64
MSU-H-CTZ-18	0.529	18	1.0	1.0
MSU-H-CTZ-34	0.290	34	1.2	2.5

[a]($cm^3 \cdot g^{-1}$). [b](% by mass). [c]($g \cdot cm^3$) obtained dividing the loss in pore volume for the loaded CTZ quantity, normalized to the grams of silica. [d](Number of CTZ molecules per theoretical surface area of the silica unit cell). For MSU-H-CTZ-12, Imidazole (I) and (II), phenyls (I) and (II) and two clear silica surface have been used, obtaining a theoretical planar concentration of 0.66 CTZ / 1.606 nm^2. For MSU-H-CTZ-18, Imidazole (I) and (II) and phenyls (I) and (II) have been used. For MSU-H-CTZ-34, molecular layer (I) and (II) have been used.

SOLID STATE NUCLEAR MAGNETIC RESONANCE

Solid-state NMR measurements were performed in order a) to evaluate the inclusion of CTZ in the OMS; b) to quantify the amount of included CTZ; c) to evaluate the mobility of CTZ inside the silica.

The ^{13}C CPMAS spectra of pure CTZ, MSU-H, MSU-H-CTZ-12, MSU-H-CTZ-18 and MSU-H-CTZ-34 are reported in Figure 2.10, while ^{1}H MAS spectra are reported in Figure 2.11. Selected ^{1}H and ^{13}C chemical shift values are reported in table 2.4.

The ^{13}C CPMAS spectra of MSU-H-CTZ-12, MSU-H-CTZ-18 and MSU-H-CTZ-34 are characterized by broad peaks with respect to pure CTZ whose spectrum presents sharp lines typical of highly crystalline systems. The strong overlapping of the signals in the aromatic region (110-150 ppm) prevents any possible assignment. However, the broadness of the resonances and the shift of the C_{sp3} atom on passing from pure CTZ to

loaded MSU-H clearly show that CTZ has been included in the cavities of the silica. Furthermore, the higher width of the peaks for MSU-H-CTZ-12, MSU-H-CTZ-18 and MSU-H-CTZ-34 with respect to pure CTZ proves the amorphous character of CTZ inside MSU-H, which is a positive characteristic since bioavailability usually increases with the amorphization.[97,108]

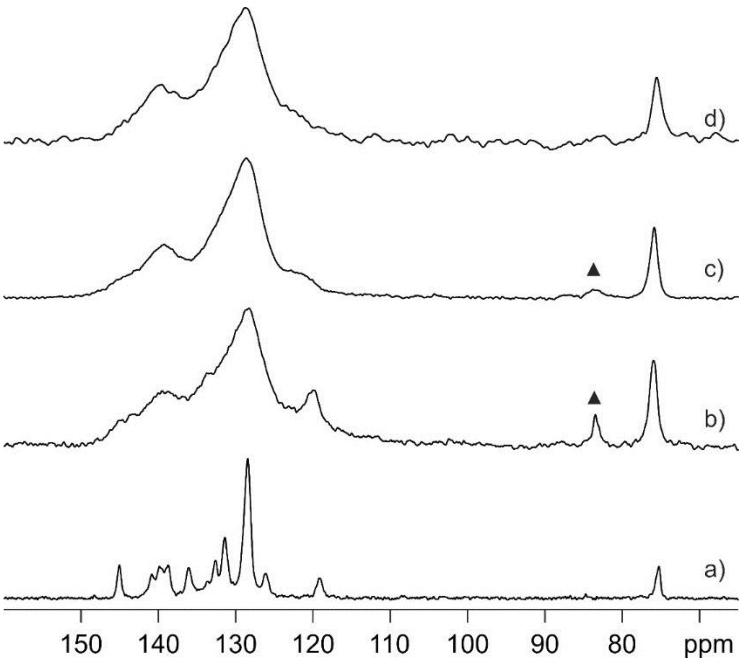

Figure 2.10: ^{13}C (100.65 MHz) CPMAS spectra of pure CTZ, MSU-H-CTZ-12, MSU-H-CTZ-18 and MSU-H-CTZ-34. The symbols ▲ denote residues of CH_2-CH_3 groups from surfactants involved in MSU-H preparation processes.

This agrees with the loss of periodicity associated to the inclusion process which allows for several possible adsorption ways of CTZ on the silica walls as predicted by NLDFT methods.[99] Moreover, at higher loading, the predicted formation of amorphous layers still is consistent with the observed line widths.

The ^1H MAS spectra are characterized by three main signals (see Table

2.4 and Figure 2.11): from spectrum **a**, the CTZ hydrogen atoms (H_{CTZ}) at 6-7 ppm (**III**); from spectrum **f**, free SiOH groups (**I**) at 1.8 ppm in accordance with the literature;[109] finally, from spectrum **b**, the SiOH groups in interaction with H_2O (SiOH-H_2O) at 4-5 ppm (**II**). The symbols ▲ denote the impurities derived from the silica synthesis (2-5 ppm). Indeed, as also showed by the FTIR spectra, in accordance with the literature,[110] these are -CH_2 and -CH_3 residues of the involved surfactants. The small differences in the chemical shifts among all samples are related to the different environment and crystal packing of the CTZ molecules in the silica, from isolated sites to layers.

Table 2.4: ^{1}H and ^{13}C selected chemical shifts (δ) with assignments for CTZ, MSU-H, outgassed MSU-H, MSU-H-CTZ-12, MSU-H-CTZ-18 and MSU-H-CTZ-34.

Compound	**^{13}C**		**^{1}H**			
	C-C-Cl	C-N	C_{sp3}	CH_{CTZ}	SiOH-H_2O	Free SiOH
CTZ	145.1	119.1	75.3	6.1	-	-
MSU-$H_{outgassed}$	-	-	-	-	4.0	1.8
MSU-H	-	-	-	-	4.2/ 6.0^{sh}	-
MSU-H-CTZ-12	145.0	120.4-119.8	75.9	6.4	4.3	-
MSU-H-CTZ-18	144.0^{sh}	121.6^{sh}	76.0	7.0	5.2	-
MSU-H-CTZ-34	not detectable	not detectable	75.6	6.5	3.8^{sh}	-

^{sh} shoulder. ^{bb} broad band.

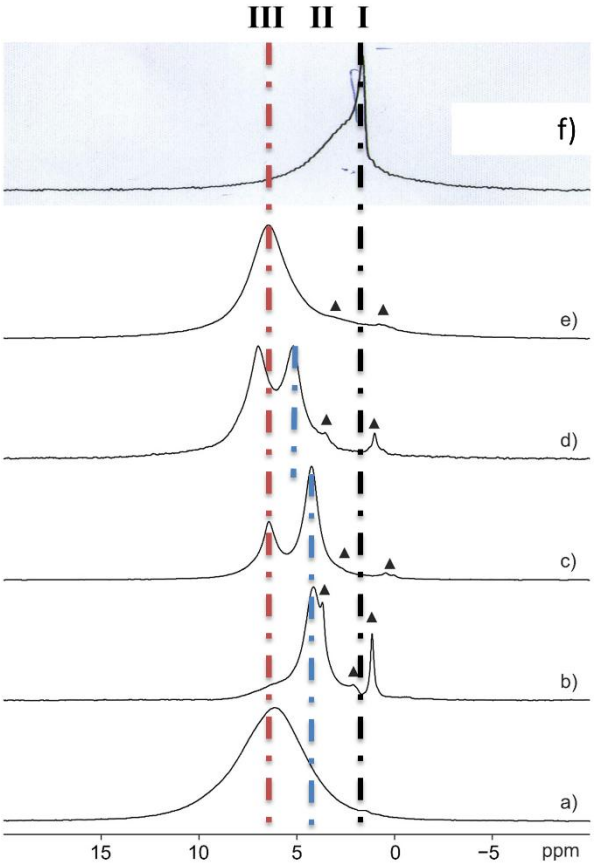

Figure 2.11: ^{1}H (400.23 MHz) MAS spectra of pure CTZ (a), MSU-H ($scCO_2$ treatment) (b), MSU-H-CTZ-12 (c), MSU-H-CTZ-18 (d), MSU-H-CTZ-34 (e) and MSU-H (outgassed) (f).

The most important information can be extracted from the variation of the relative intensities of the signals. Indeed, while the MSU-H spectrum (**b**) is almost completely dominated by the SiOH-H_2O signal, the spectra of MSU-H-CTZ-12, MSU-H-CTZ-18 and MSU-H-CTZ-34 are characterized by a progressively enhancement of the signal around 6-7 ppm attributed

to H_{CTZ} atoms. Furthermore, the SiOH peaks reduce their intensity on passing from pure MSU-H to MSU-H-CTZ-34, from lowest to highest loading.

As already reported in table 2.4, from the experimental TG results, in comparison to the N_2 adsorption measurements, the number of CTZ per theoretical surface area of the silica unit cell (1.606 nm^2) can be evaluated. This value, in table 2.5, has been reported as molecules per square nanometre. With the same approach, also the H_2O content has been calculated.

Table 2.5: Correlation between experimental TG analysis, N2 isotherms, theoretical molecule distribution and SSNMR.

TG[a]	CTZ·1.606 nm^{-2} [b]	CTZ[c]	H_2O[d]	H_{CTZ} [e]	$H_{SiOH-H2O}$ [f]	SSNMR [g]
0	0.00	0.00	4.5	0.0	13.5	-
12	0.64	0.40	3.0	7.0	10.5	1.0:1.6
18	1.00	0.62	3.0	10.6	10.5	1.0:1.0
34	2.50	1.56	0.0	26.5	4.5	-

[a](% by mass) obtained from TG analysis (Figure S1), [b](Number of CTZ molecules per theoretical surface area of the silica unit cell), [c](CTZ molecules per nm^{-2}) obtained from TG results and NLDFT elaboration of experimental nitrogen adsorption isotherms, [d] (H_2O molecules per nm^{-2}) obtained from TG results and NLDFT elaboration, [e](H_{CTZ}·nm^{-2}), [f](H_{H2O}·nm^{-2}), [g]SSNMR ratio between the peaks attributed to H_{CTZ} and $H_{SiOH-H2O}$. As free SiOH surface concentration the value of 4.5 SiOH·nm^{-2} has been used, in agreement with the theoretical model surface concentration.[99]

The obtained value of 3.0 H_2O·nm^{-2} from thermogravimetric analysis, compared to the chemical shift of 4.2 ppm, is in agreement with the literature.[111] Indeed, Grünberg et al. reported a value of 4.0 ppm with a surface coverage of 3.6 H_2O·nm^{-2}.

The integral values, obtained from the deconvolution analysis of

quantitative ^{1}H spectra, of the CTZ and SiOH-H_2O signals at 6.1-7.0 and 3.8-6 ppm, respectively result to be consistent with the previously reported CTZ-silica ratios per unit cell.[99] Indeed, for instance, the ^{1}H spectrum of MSU-H-CTZ-12 is characterized by a relative intensity of the $H_{SiOH\text{-}H2O}$ and the H_{CTZ} resonances of 1.6 to 1. This is consistent with the reported data of 0.64 CTZ·1.606 nm^{-2}, experimentally obtained and theoretically confirmed. Accordingly, in the MSU-H-CTZ-18 situation the H_{CTZ} and $H_{SiOH\text{-}H2O}$ signal intensities are comparable (1:1). This, again, is coherent with the experimental and theoretical evidenced mode of interaction. On the other hand, a slight chemical shift of the MSU-H OH peaks is evident. This small shift has been attributed to an increase of H-bonds between SiOH and CTZ, as evidenced by FTIR and theoretical calculations. Indeed, other SSNMR analysis of guest molecules evidenced this chemical shift. Of particular interest is the work of Shenderovich et al.[112] reporting the chemical shift of SiOH in interaction with pyridine (9.9 ppm). For the same reason, hypothesizing a higher chemical shift, in the case of MSU-H-CTZ-34, no ratio has been evaluated.

It can be concluded that, during the $scCO_2$ process, the CTZ molecules slowly replace H_2O molecules in the H-bond interaction with SiOH. Indeed, the number of H-bonds formed remains constant, changing the guest molecule. The reasons should be a stronger interaction of the SiOH-CTZ, as evidenced by higher FTIR redshift, theoretical energy of interaction and experimental energy of desorption.[99] On the other hand, has been evidenced by theoretical calculation that an interaction between SiOH and guest molecule is favoured by the H_2O presence.[113] Consequently, the cause remains uncertain and could include the hydrophobicity nature of CTZ that, during $scCO_2$ process, builds up a hydrophobic molecular layer.

Since, often, the ability of the controlled release of a host molecule inside a guest is also related to its mobility, the dynamic of CTZ inside the silica

has been probe through relaxation measurements. Thus, ^{1}H T_1 relaxation time measurements were performed on all the samples. Indeed, in the solid state, the T_1 is strongly related to the strength of the dipolar interaction, which directly depends on the presence of fluctuating magnetic fields generated by the dynamic behaviors of the whole molecule or of parts of it.

MOBILITY OF ADSORBED CLOTRIMAZOLE

Ab-Initio Molecular Dynamics (AIMD) has been performed on the different statically optimized geometries in order to evaluate the stability of the local minimum structures of figure 2.6. Detailed data are reported in a published article.[99] AIMD simulation on the molecular layer (II) structure shows high mobility of the three CTZs (per unit cell) on the surface. The RMSD of the atomic positions along the AIMD simulation shows a large movement between 4 and 7 ps that results in a new configuration, with a RMSD value of 4.3 Å with respect to the starting CTZ conformation after 11 ps. The process is described in Figure 2.12, where the exposed nitrogen atoms of the imidazole rings of the three adsorbed molecules in each unit cell are referred as N1, N2 and N3. The graph in Figure 2.12.a, reporting the N1-SiOH_III and N1-SiOH_I distances, clearly shows a transition state where the chain is lost and the imidazole's nitrogen (N1) is equidistant from SiOH(I) and (III). Looking at the potential energy fluctuations during this simulation, we estimate, in a very approximate way, the electronic activation energy of this process as 29.7 $kJ \cdot mol^{-1}$ that can be considered an upper limit for the real value.

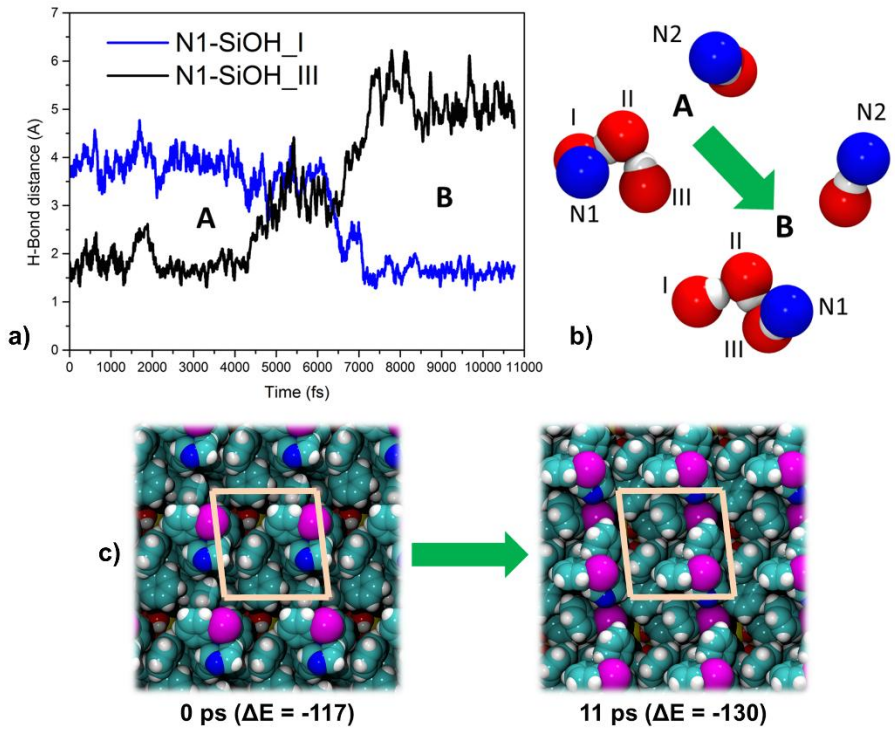

Figure 2.12: AIMD of the molecular layer (II) structure: a) N1-SiOH(I) and N1-SiOH(III) bond distances in time. b) starting (A) and final (B) positions of N1 and N2 with respect to the involved SiOHs. c) Top views of the initial (left) and final (right) configurations in the AIMD simulation, with the corresponding interaction energies per CTZ molecule (kJ·mol^{-1}); cell borders in pink.

These AIMD results are in accordance with the experimental finding of a "liquid like" behavior of ibuprofen adsorbed in MCM-41.[42,43] Considering that CTZ is much more hydrophobic than ibuprofen it is no surprise that CTZ molecular layers are very mobile, despite the significant underneath interactions. This mobility can be represented as a walking step process guided by local changes in the H-bond interactions, helped by a high flexibility of the silica surface silanols.

From an experimental point of view, the ^{1}H T_1 relaxation time of SSNMR increases from 0.1 s to 80 s by increasing the CTZ loading from MSU-H-CTZ-12 to MSU-H-CTZ-34. This can be attributed to a reduction of

mobility of CTZ inside the silica on passing from the isolated CTZ molecules (higher mobility for low loading) to the formation of a layer (lower mobility for high loading) as previously described.[99] Conversely, pure CTZ is characterized by a ^{1}H T_1 of 90 s, typical of very rigid crystal packing. Summarizing, the evidenced mobility in the molecular dynamics simulations obtained by some of use[99] follows frankly the SSNMR relaxation times. Indeed, in the case of single docking (Imidazole (I) and (II), phenyls (I) and (II)) high energetics phenomena are observed like lose and acquire of H-bonds due to CTZ movement or rotation in place. On the other hand, the molecular layers (I) and (II) show higher cooperation moving as a layer on the silica surface but not among them.

EXPERIMENTAL AND THEORETICAL FTIR INTERPRETATION

Experimental and theoretical vibrational spectra of CTZ in molecular, crystalline and adsorbed environments have been obtained[99]

Figure 2.13 reports both the experimental (blue line) and the theoretical (red line) IR spectra of CTZ in interaction with silica at low and high coverage. The low coverage experimental spectrum has been acquired on a MSU-H-CTZ sample with a drug loading of 18% by mass, while the high coverage corresponds to a drug loading of 34% by mass. As regards the simulated spectra, the CTZ modes have been obtained in both cases from a vibrational analysis in the harmonic approximation of the drug in the four single molecule configurations, combined by Boltzmann weighting their contribution to the infrared intensity according to the computed interaction energies.

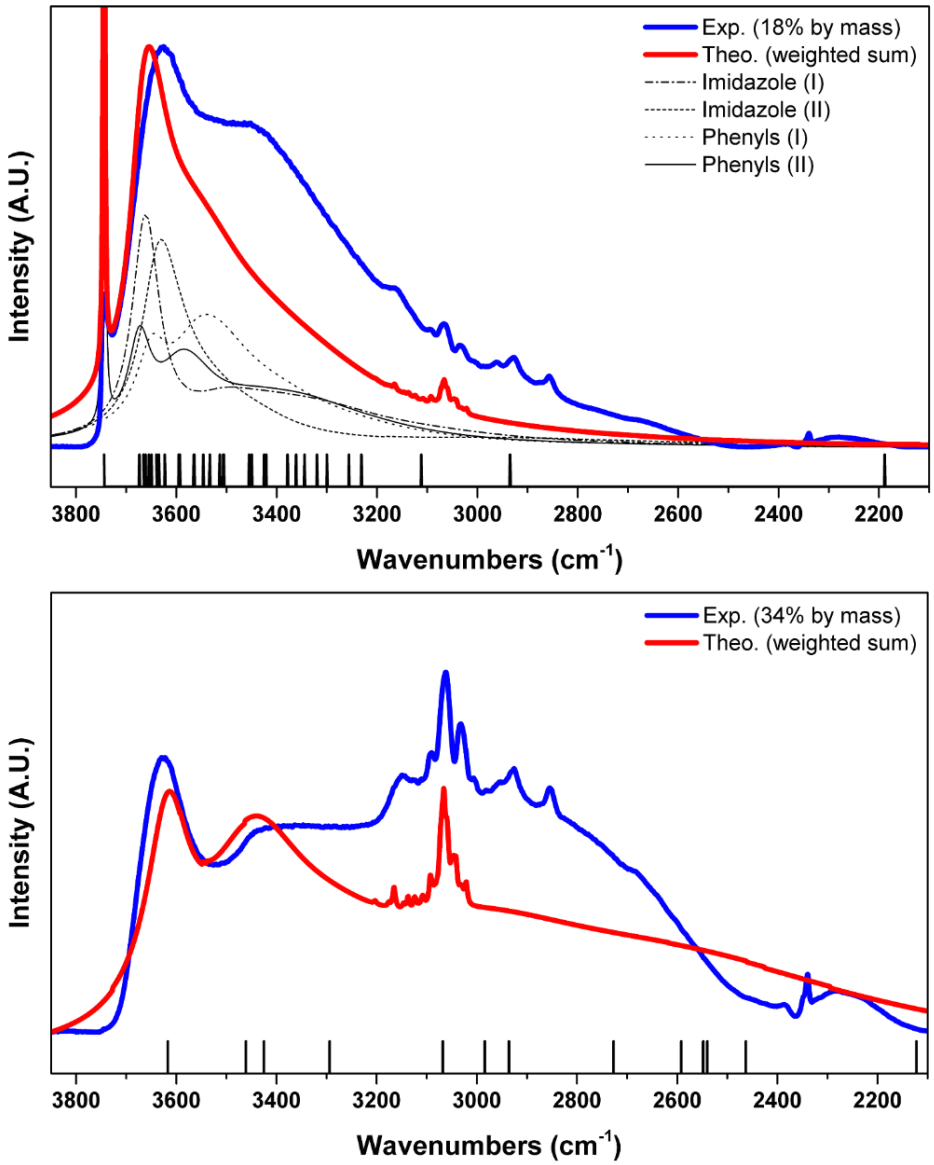

Figure 2.13: Experimental and simulated IR: experimental FTIR spectrum of MSU-H-CTZ (blue); theoretical IR spectrum of CTZ combined with SiOH vibrational contribution (red); simulated IR spectrum of SiOH vibrational contribution of: imidazole (I) (dot-dashed black line); imidazole (II) (dashed black line); phenyls (I) (dotted black line); phenyls (II) (black line). At the bottom of the graph, sticks represent the theoretical SiO-H stretching frequencies without Pimentel's correction.

For both the low and high loading cases, the agreement between theory and experiment is remarkable and helps the interpretation of the signals. A more detailed description can be read elsewhere.[99]

As can be deducted from figure 2.13, increasing the CTZ loading results in an increasing number of H-bonds between SiOH and CTZ molecules. Indeed, the 3750 cm^{-1} sharp band, decrease gradually while the 3500-2600 cm^{-1} broad band increase. At the highest loading obtained there are no free silanols. This shift is attributed to the formation of H-bonds between SiOH and CTZ through the exposed nitrogen of the imidazole ring. At the same time, other types of H-bonds are formed with the CTZ molecules (SiOH-π, SiOH-Cl) that are responsible to the change in the 3700-3500 cm^{-1} band. Starting from SiOH-SiOH interaction in the bare MSU-H, they evolve gradually in a mixture of the same H-bonds mixed to interactions with CTZ (SiOH-π and SiOH-Cl). To demonstrate this, the broad background at 3700-3500 cm^{-1} responsible to the increase of the 3620 cm^{-1} peak, more substantial in MSU-H-CTZ-12, almost disappears in MSU-H-CTZ-34. These conclusions reveal the direct interaction between CTZ and mesoporous silica wall until the formation of a CTZ molecular layer.

2.3 MCM-41 FILLING MODEL

TG analysis and nitrogen adsorption measurement comparison applied to MCM41-1 do not lead to the same conclusions. While FTIR analysis presents the same adsorption band, the mesopores of MCM41-1 results filled of CTZ molecules without homogeneity. Indeed, no empty pore are visible after the $scCO_2$ process. In chapter 3 a more detailed description is given, but here are reported preliminary theoretical discussion of a new

model of incorporation.

As mentioned above, in the case of MSU-H, the pore diameter (8.5 nm) allows us to consider the silica surface as flat when CTZ is docked. For MCM-41 this assumption is not anymore satisfied. Consequently, the surface model has been modified following the MCM-41 model presented in the article of Delle Piane et al.[84]

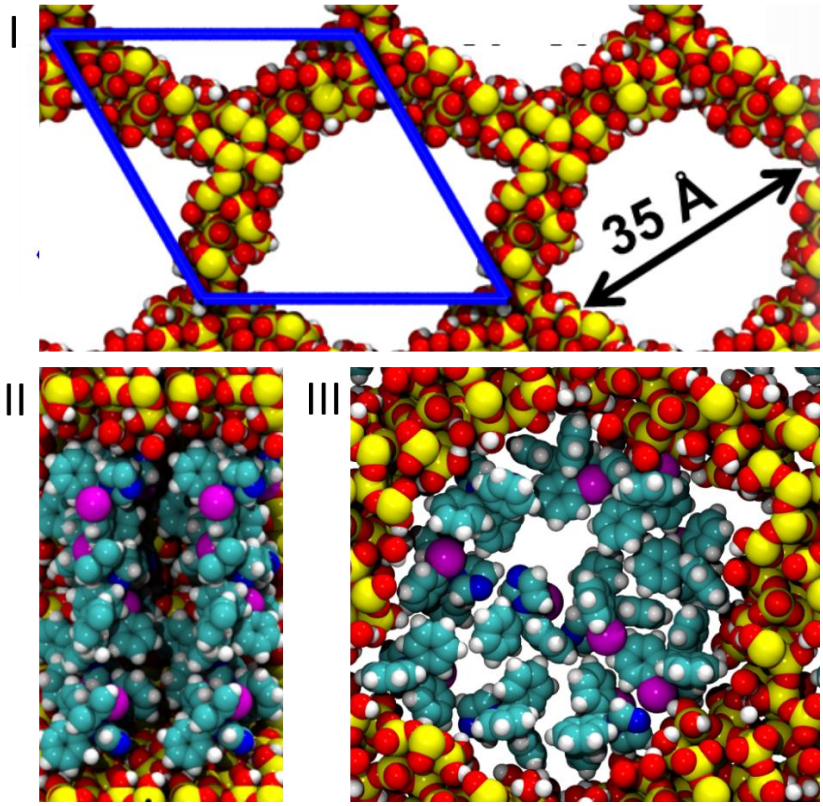

Figure 2.14: Longitudinal view of the MCM-41 model (I). (II) and (III) simulation of the filled CTZ channel.

The MCM41-CTZ model has been optimized at PBE-D2 level of theory. The basilar information that can be extracted is that 9, out of 11 CTZ molecules, are interacting with the silica surface. The last 2 are in a position similar to the molecular layer (I) and (II). In addition, the number and energies of interactions are higher. This discussion reveals in a

simplified way the motivations of the MCM41-1 filling during the $scCO_2$ incorporation process.

CHAPTER 3: SILICAS DETERMING FACTORS IN THE INCORPORATION PROCESS

ABSTRACT

The knowledge of the specific interactions between the surface of mesoporous silica and drugs took to comprehend the different type of adsorption geometries depending on the pore size dimension. However, such knowledge is still preliminary.

In this chapter a complete experimental description on these factor have been argued. Fourteen mesoporous silica have been incorporated trough $scCO_2$ process and completely characterized in order to understand the experimental discriminant factors. In the first part, a characterization of all OMS as such is reported; after that, the different behaviors are described; finally, some argumentation are stated.

3.1 OMS CHARACTERISTICS

The 14 mesoporous (Table 3.1) silicas were selected for different characteristics and considerations. One mesoporous silica is, to be correct, a disordered microporous silica, Syloid. Four MCM-41, were synthesized to screen low pore diameter silicas. One commercial MCM-41 was necessary to avoid laboratory behaviors. Four KIT-6 were manufactured to control if Ia3d silicas have the same behavior. Two commercial and one synthetic SBA-15 were used to point out the conduct with high pore dimension. The MSU-H was reprocessed to control the supercritical process and the reproducibility of the results.

Table 3.1: NLDFT parameter of all the OMS used. They have been ordered according to the mean pore diameter that is not ever the maximum of the PSD.

OMS	Mean pore diameter (nm)	NLDFT SSA (m^2g^{-1})	NLDFT Volume (cm^3g^{-1})
Syloid	1.37	1157	0.378
MCM41-4	2.94	840	0.598
MCM41-3	3.65	930	0.818
MCM41-ACS	4.57	843	0.901
MCM41-1	4.88	812	1.286
MCM41-2	4.88	585	1.100
KIT6-50	5.28	678	0.560
KIT6-80	6.55	603	0.690
SBA15	6.79	763	0.697
KIT6-100	7.86	788	1.157
MSU-H-F	8.14	643	0.836
SBA15-ACS	8.14	424	0.884
MSU-H	8.46	596	0.900
KIT6-130	10.13	525	1.300

From table 3.1 and figure 3.1.I it can be evidenced that the OMS are mainly divided in two categories: silicas with mean pore diameter lower than 4.88 nm and silicas higher than this. Indeed, two main straight line can be verified from the graph 3.1.I. This categorization is due to the wall thickness. It is well clear that MCM-41 and SBA-15 silicas have this differences. It is strange that also Syloid and KIT-6 respects this condition.

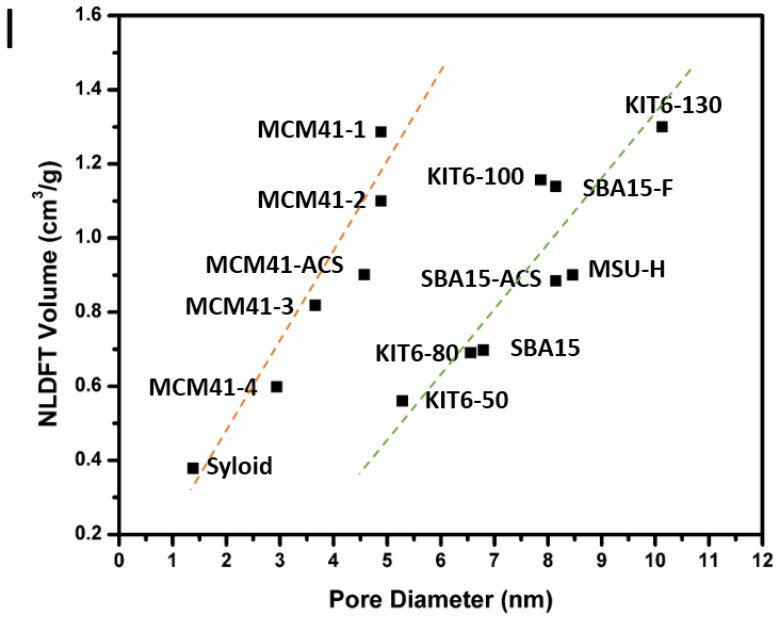

Figure 3.1: Distribution of OMS in function of mean pore diameter and pore volume (I).

All the OMSs have been characterized by TG, XRD, FESEM analysis. No important result for this correlation have been noted.

3.2 CHARACTERIZATION OF INCORPORATED OMS

All the OMS have been incorporated through $scCO_2$ at 250 bar and 373K for 18 hours. No further incorporation was possible increasing the total time. All the characterization analysis already described were repeated on the incorporated materials. Absolute data are, first of all, the maximum incorporated quantity: 46% by mass obtained with MCM41-1. Secondly, in no circumstances crystalline CTZ was observed. Thirdly, all the N_2 adsorption measurements reported a decrease of SSA and pore volume. In some cases, also the mean pore diameter was decreased.

Figure 3.2 reports some of the nitrogen adsorption measurements done. It can be observed that for Syloid and MCM-41, after the supercritical process, there is almost no residue porosity (no step or hysteresis) and very lower surface area (lower inclination). On the other hand, MSU-H and KIT6-130 still have large empty porosity. A border case is the KIT6-50.

According to chapter 2, it can be argued that the first OMSs are filled of CTZ as the theoretical modelization of figure 2.14, while in the second group CTZ is adsorbed as a molecular layer, figure 2.8. Trying to understand the limiting pore size dimension, a further analysis has been done. Figure 3.3 reports the incorporated quantity in function of the NLDFT pore volume. In this case the incorporated quantity is calculated as the CTZ content on the silica content.

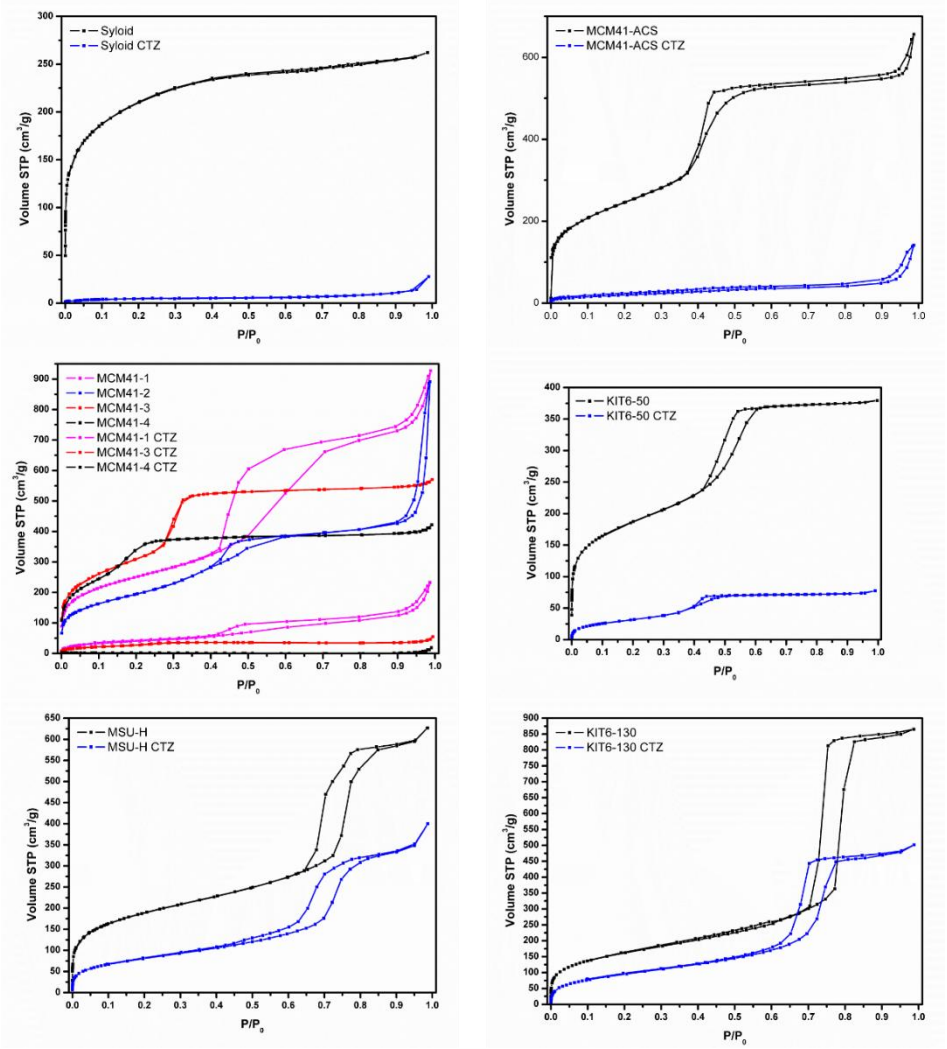

Figure 3.2: Nitrogen adsorption measurements before (OMS) and after the $scCO_2$ process (OMS-CTZ).

This correlation evidences which OMSs follows the filling model. On the other hand, an R^2 of 0.93 is not a good report; but, considering the error bars, all the data are consistent. The linear equation has been selected without constant term thinking to the fact that the mesopore could be filled or empty. On the contrary, in no cases the external SSA was taken into account. Indeed, this correlation do not consider the external surface coverage that it is hardly estimable.

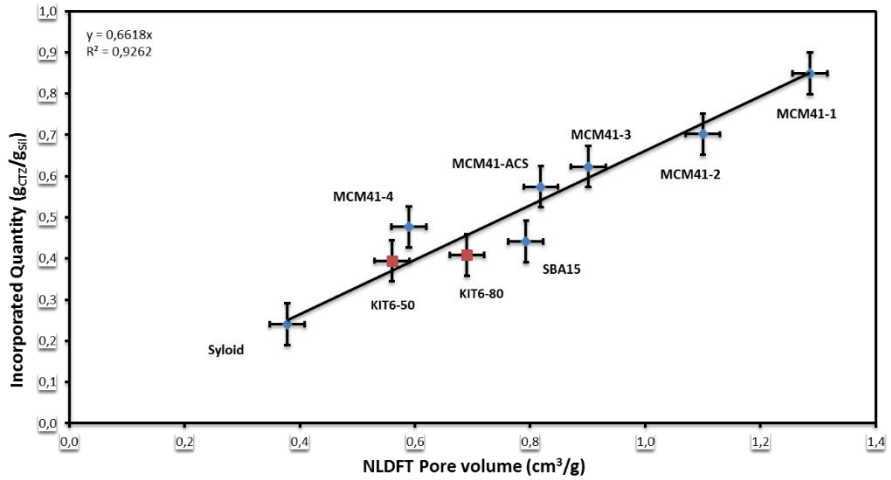

Figure 3.3: OMS correlations: Incorporated Quantity (g_{CTZ}/g_{sil}) versus NLDFT Pore Volume (cm^3/g_{sil}). The red dot reports a border linearity.

At the same time, the correlation of NLDFT SSA with incorporated quantity has been done and reported in figure 3.4.

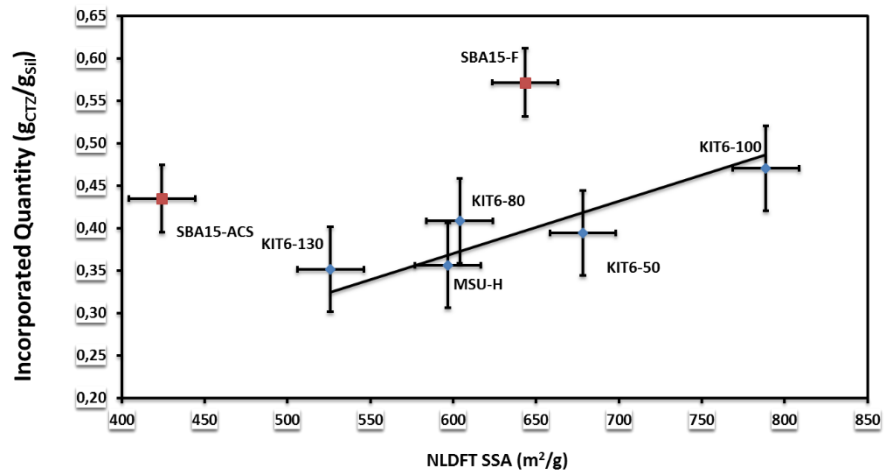

Figure 3.4: OMS correlations: Incorporated Quantity (g_{CTZ}/g_{sil}) versus NLDFT SSA (m^2/g_{sil}).

In this case R^2 is 0.95 and the slope (m) of the linear equation is directly correlated to the number of CTZ·nm^{-2}. The results, reported to the surface area of the silica theoretical cell (chapter 2), is 1.7 CTZ·$cell^{-1}$. This result

is lower than the presented one of chapter 2 but also the $scCO_2$ conditions are lower (250 bar).

As it is possible to observe, not all the silica follows perfectly these relationships. For instance, KIT6-50 and KIT6-80 follow both correlations. Consequently, in order to correctly distinguish all cases, the PSD simulations have been applied for all the OMSs, taking into account the number of CTZ extrapolated from the linear correlation. If it works, it can be defined as a molecular layer; on the contrary, it could follow the filling correlation.

The results, reported in figures 3.5 – 3.6 – 3.7, shows three conditions:

- Figure 3.5: OMSs perfectly filled, without residual porosity.
- Figure 3.7: OMSs with a molecular layer of about 1.7 CTZ/cell;
- Figure 3.6: a condition in between.

Therefore, it seems reasonable conclude that from a mean pore radius of 5.2 to 6.8 nm the behavior is mixed. Probably, also the Ia3d structure of KIT-6 silicas is important. Indeed, the SBA15, which has the bigger mean pore diameter, seems to follows better the filling model, but it suffers more than the others of low diffusivity (2D pore structure versus 3D.)

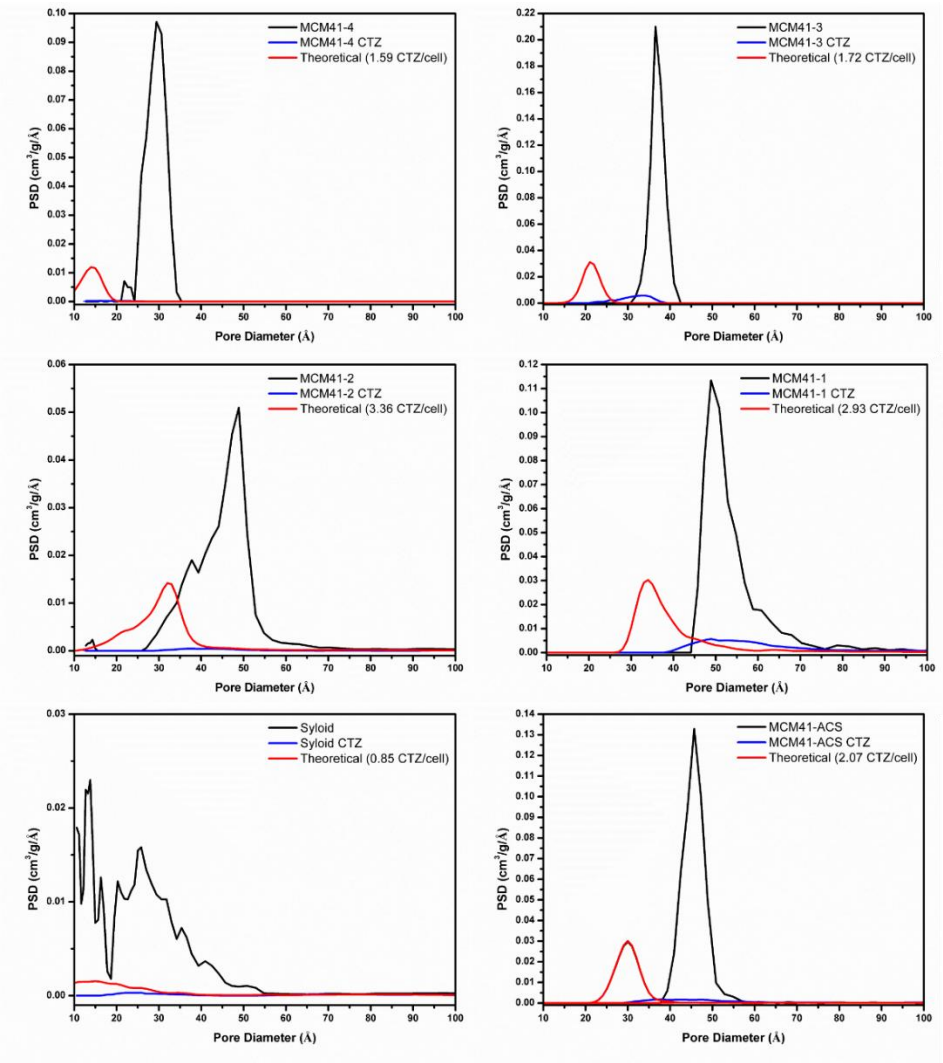

Figure 3.5: PSD of OMS as such (black), OMC-CTZ (blue) and the calculated PSD (red). In brackets the number of CTZ per unit cell used for the model. These are the silicas that follows a filling theory.

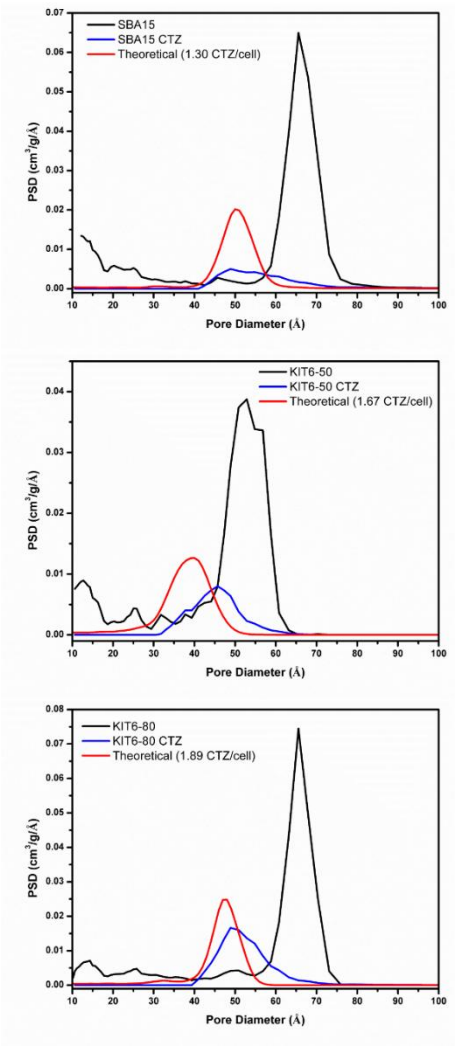

Figure 3.6: PSD of OMS as such (black), OMC-CTZ (blue) and the calculated PSD (red). In brackets the number of CTZ per unit cell used for the model. These are the silicas border line.

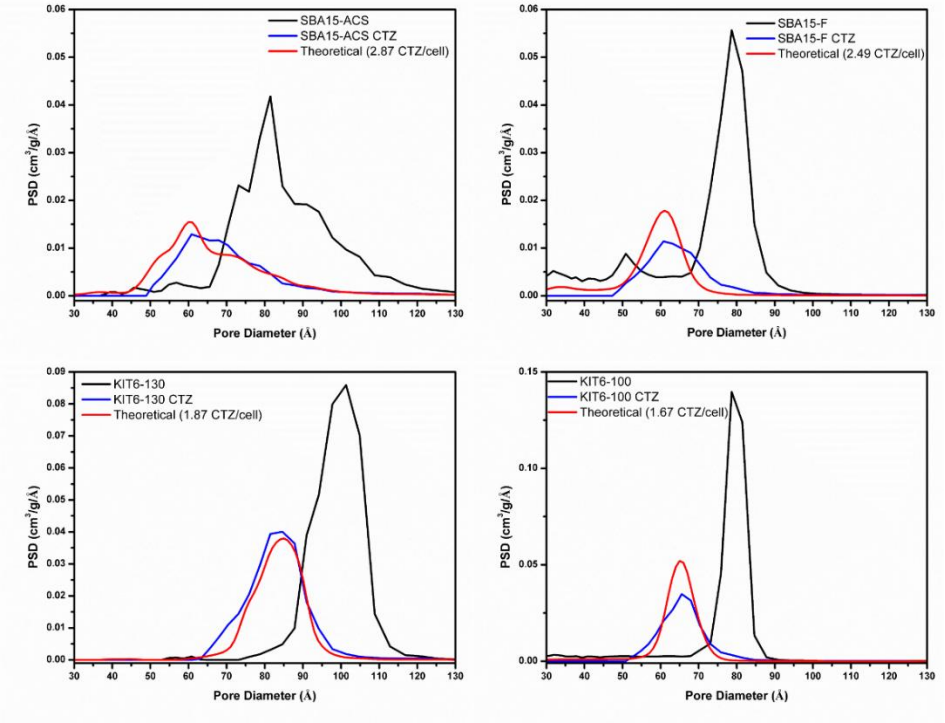

Figure 3.7: PSD of OMS as such (black), OMC-CTZ (blue) and the calculated PSD (red). In brackets the number of CTZ per unit cell used for the model. These are the silicas that follows the molecular layer theory.

Table 3.2: OMS correlations resume.

OMS	Mean Pore Diameter	Correlation
Syloid	1.37	Pore Volume
MCM41-4	2.94	Pore Volume
MCM41-3	3.65	Pore Volume
MCM41-ACS	4.57	Pore Volume
MCM41-1	4.88	Pore Volume
MCM41-2	4.88	Pore Volume
KIT6-50	5.28	Both
KIT6-80	6.55	Both
SBA15	6.79	Both
KIT6-100	7.86	SSA
MSU-H-F	8.14	SSA
SBA15-ACS	8.14	SSA
MSU-H	8.46	SSA
KIT6-130	10.13	SSA

In conclusion, one more correlation need to be reported. From the NLDFT pore volume data and the TG analysis the density of CTZ inside the mesoporous volume can be evaluated. The next equation resumes this correlation:

$$Incorporated\ Quantity\ \left[\frac{g_{CTZ}}{g_{sil}}\right] = V'\left[\frac{cm^3}{g_{sil}}\right] - \left\{V''\left[\frac{cm^3}{g_{sil+CTZ}}\right] \cdot \left(\frac{g_{sil+CTZ}}{g_{sil}}\right)\right\}$$

where *V'* is the OMS NLDFT pore volume as such and *V''* after the $scCO_2$ process. The incorporated quantity and the ratio $\left(\frac{g_{sil+CTZ}}{g_{sil}}\right)$ are obtained through TG analysis.

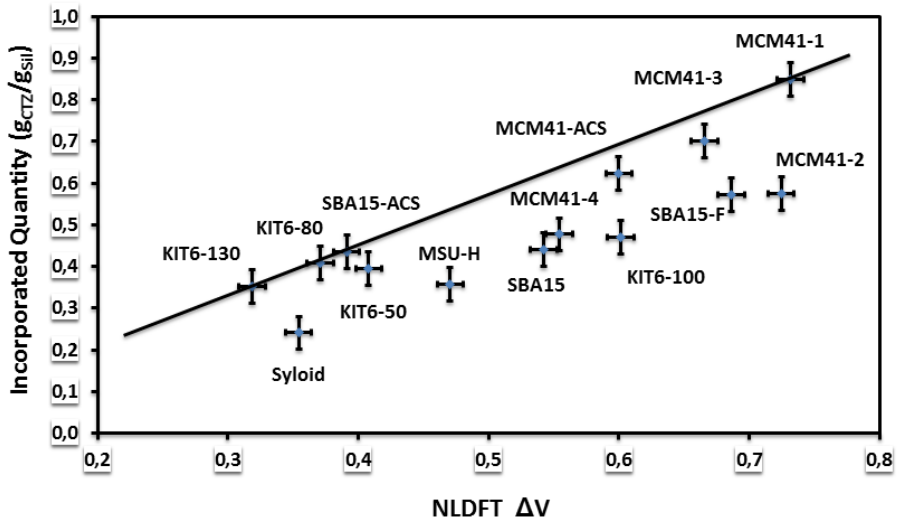

Figure 3.8: Incorporated quantity ($g_{CTZ} \cdot g_{sil}^{-1}$) versus NLDFT ΔV ($cm^3 \cdot g_{sil}^{-1}$): the density correlation.

The straight line has a slope coefficient (*m*) of 1.14 $g_{CTZ} \cdot cm^{-3}$. This result matches perfectly with all other correlations (chapter 2). In addition to this, it can be said that all the OMSs that are not on the straight line suffers of pore occlusion. None of these have large amount of CTZ outside the mesoporous volume.

CHAPTER 4: AKS-OMS GEL

ABSTRACT

A possible and promising area of application for Ordered Mesoporous Silica (OMS) is the topical therapy of dermatological diseases and wounds. It is widely known that Active Pharmaceutical Ingredient (API) incorporated in OMS based materials are adsorbed in the volume in an amorphous state and in some cases well distributed on the surface as a single molecular layer. This feature is crucial for many aspects: from the bioavailability enhancement of molecule poorly soluble in water to the effects of reservoir that can be tuned in cream for topical application. Indeed, the use of OMS incorporated of API in a saturated vehicle to the therapeutic concentration develops a controlled and constant release system on the skin site.

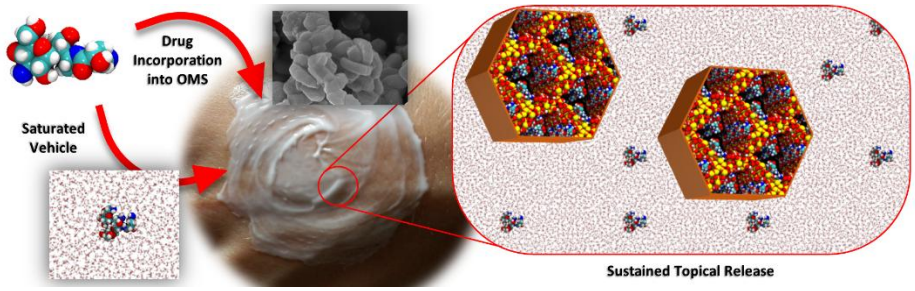

Figure 4.1: Ideal description of AKS-OMS gel.

This chapter describes the development of topical composition able to release drug in a sustained and prolonged manner. Incipient Wetness Impregnation procedure has been used to load AKS in commercial OMS of MSU-H type. The incorporated OMS characterization (XRD, FESEM, etc.) are reported in chapter 1. A series of different release test has been performed to validate the new release technology (UV-Vis spectroscopy). As a result, a semisolid formulation with AKS has been developed. The

stability, pH and rheological properties were investigated overtime. In vitro release and permeation studies were assessed using an open chamber diffusion cell system (Franz cell), fitted with semi-permeable membrane or porcine ear skin. All the results emphasize the reservoir effect of OMS incorporated of API. In addition, they demonstrate the availability of a new topical release technology able to reduce the number of administrations.

4.1 SUSTAINED RELEASE FROM OMS-AKS IN AKS SATURATED SOLUTIONS

In order to confirm the reservoir effect of the incorporated OMS in a saturated solution composed by two solvents, AKS, a hydrophilic API, has been studied. Commercially, the more used topical creams which contains AKS have a composition at 5% by mass of API, that corresponds to 6,67% by mass of AKS [114,115]. Therefore, in order to obtain a solvent with a saturation point toward AKS equal to the therapeutic concentration, a solution of glycerol and water has been explored. The best composition is 45% water and 55% glycerol by mass. The saturation point of this solution is 71 $mg \cdot ml^{-1}$ that correspond to 62 $mg \cdot g^{-1}$ of AKS. Consequently, the API content is 4.8% by mass. In this case two different AKS saturated solution has been done. In a solution, 80 mg of OMS-AKS (27.5 % by mass) has been added under agitation. Every hour, for 4 times, 100 µl has been withdraw and substituted with the same amount of pure solvent. Figure 4.2 reports the measured concentration in the four withdraw for each sample. The saturated concentration is preserved as long as there is drug that can be solubilized from the OMS. In fact, 22 mg of drug where presents as reservoir and in the three subsequent dilution 21.3 mg where withdraw: 100 µl contains 7.1 mg of API.

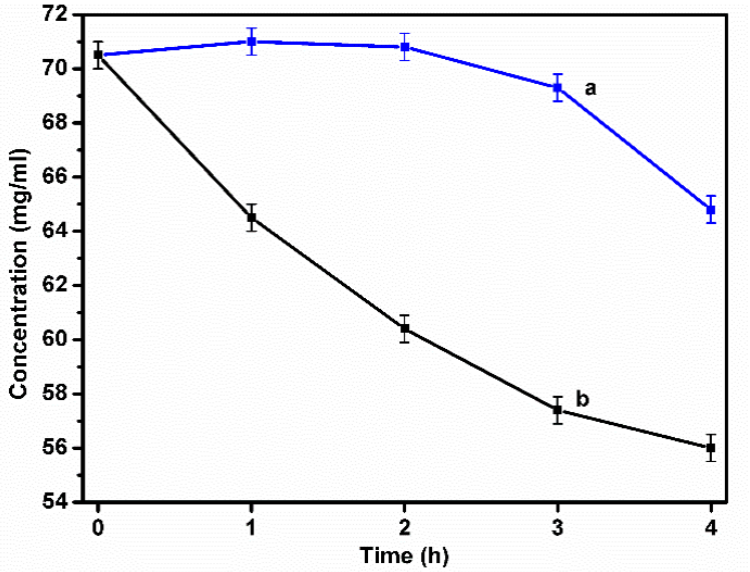

Figure 4.2: AKS sustained release with 21.3 mg of API contained in OMS-AKS (a) and without reservoir (b).

4.2 COMPOSITION, RHEOLOGICAL AND pH STABILITY OF AKS-OMS GEL

As previously described an innovative topical semisolid formulation has been prepared and compared to a commercial formulation. All the results here presented are referred to the gel named AKS-OMS gel. Among all the semisolid preparations, a hydrophilic gel was developed, consisting of a liquid phase within a polymeric matrix composed by a suitable gelling agent. Firstly, AKS was added in a solution of glycerol (45% by mass) and water (55% by mass) under magnetic stirring obtaining a saturated solution of the drug. When AKS was completely dissolved, 15% by mass OMS-AKS powder was added to the medium and then the liquid dispersion was purposely homogenized with a high shear homogenizer for 5 min at maximum velocity. Hydroxyethyl cellulose was selected as gelling agent, because it is primarily used in topical pharmaceutical

formulations and it is generally considered as an essentially non-toxic and non-irritant material [116]. With this purpose, 2% by mass of hydroxyethyl cellulose was added to the homogeneous dispersion and it was gently stirred for one hour at room temperature.

The gel shows rheological characteristic of shear-thinning fluid. Over one month the viscosity at low shear rate is halved but preserve is pseudoplastic behaviour. The Farrow's constant was 3.4 n and remain the same over the month, going out of linearity only for low shear rate (3.9 n).

During the same period, the pH oscillates from 4.75 to 5.0 without the addition of any correctors. It should be noted that this pH is equal to the pH of the commercial formulation.

4.3 IN-VITRO RELEASE STUDIES

Figure 4.3 reports the release curves obtained. In the first 100 minutes, AKS-OMS gel follows the commercial formulation. After, the commercial formulation release rate decrease since the AKS dissolved quantity is ending. In that moment, the OMS-AKS reservoir starts to make a difference in the AKS-OMS gel. Indeed, the release rate of AKS-OMS gel remains constant until 200-250 minutes. Finally, also the OMS-AKS reservoir end and the release rate decrease.

The constant release rate in the first 100 minutes proves that the starting dissolved concentration of AKS inside AKS-OMS gel and commercial formulation is the same. The preservation of a constant release rate after 100 minutes of AKS-OMS gel proves that the dissolved concentration of AKS is sustained to the therapeutics concentration until 200-250 minutes. These demonstrate the feasibility of this application as a method to reduce the number of applications during the day.

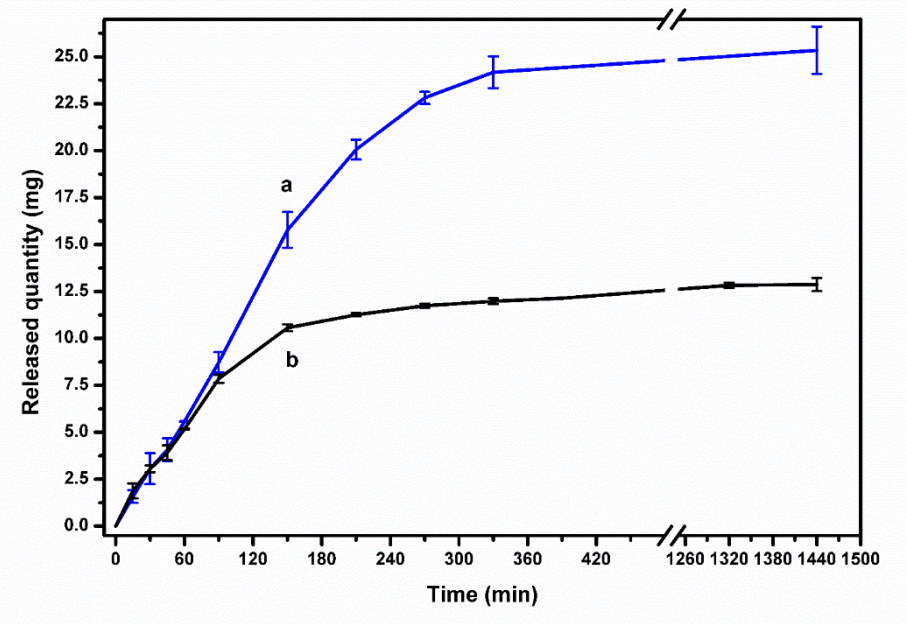

Figure 4.3: In-vitro release test of AKS-OMS gel (a) and the commercial formulation (b). Each point is the mean value of three different release tests. The error bars include the maximum variation obtained from all the different trials.

4.4 IN-VITRO PERMEATION STUDIES

In order to evaluate differences in permeation of the two semisolid formulation on a skin site, a slice of porcine ear skin has been mounted on the Franz cells (Figure 4.4). Until 100 minutes, as the release test, the permeated quantities are small and similar. After, the AKS permeated from AKS-OMS gel exceed the commercial formulation quantity. This is in agreement with the release studies that show the depletion of the commercial formulation after 100 minutes. Consequently, the permeation of AKS is influenced from the depletion of the commercial formulation. On the other hand, the constant concentration present in the AKS-OMS gel develop an increase in the permeated quantity. The complete permeation of AKS from the commercial formulation requires 24 h, while for AKS-

OMS gel it exceeds 48 h. After 4 days, no more AKS permeation is observed.

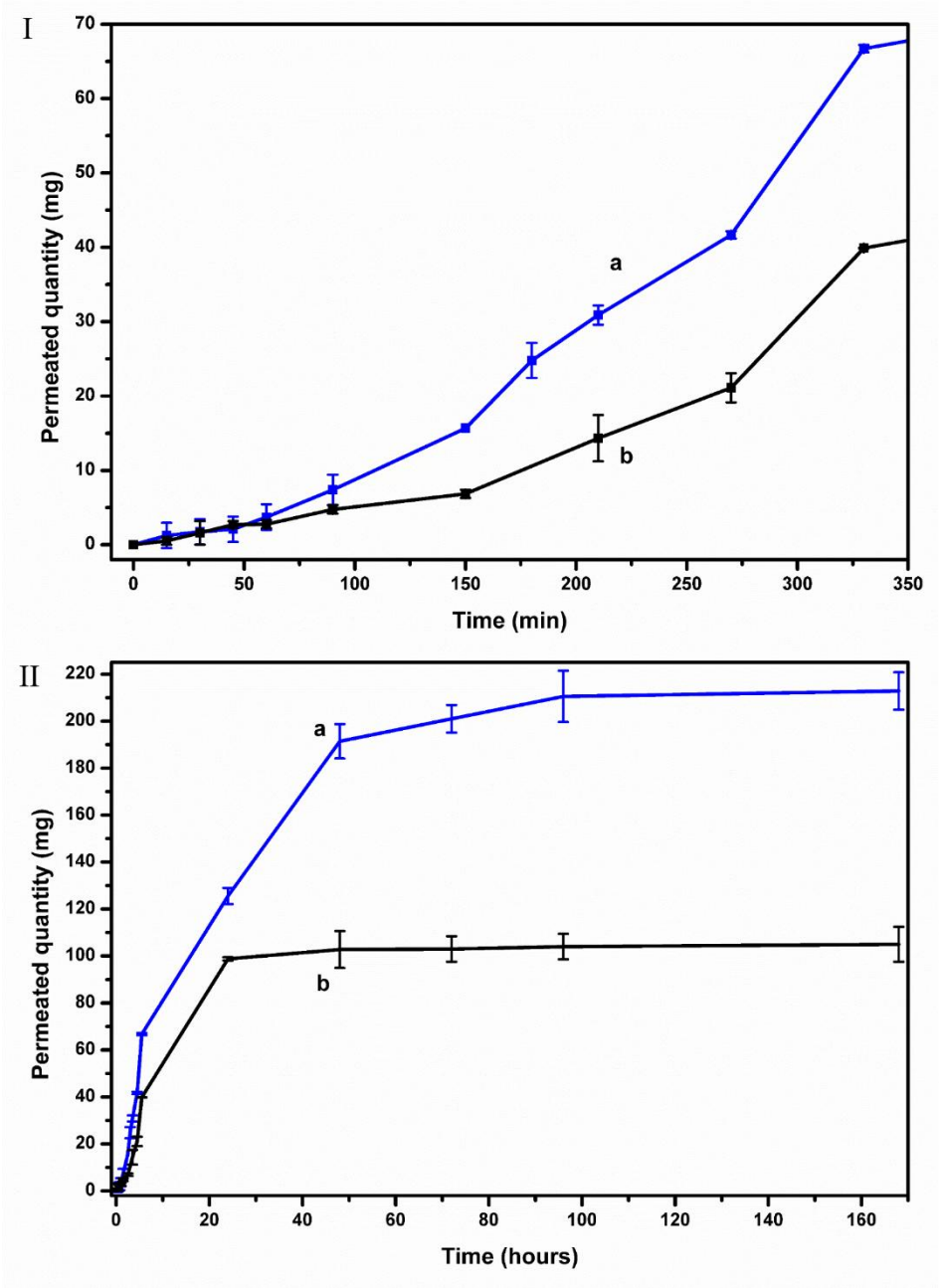

Figure 4.4: In-vitro permeation test of AKS-OMS gel (a) and the commercial formulation (b). On the left (I) the first 350 minutes; on the right (II) the

subsequent 168 h. Each point is the mean value of three different release tests. The error bars include the maximum variation obtained from all the different trials.

These results show that a constant concentration over the skin site for a prolonged time extend and enhance the permeation of API. The first result was intended. On the other hand, the enhancement could produce an overtreatment, solvable reducing the saturation point of the vehicle. This solution leads to more improvement of the new semisolid formulation. Indeed, reducing the dissolved starting therapeutic concentration will increase directly the duration of the stored AKS. Secondly, the same antibiotic effect could be achieved with less dosage on the application site.

4.5 TOPOLOGICAL INFORMATION ON OMS PERMEATION

Numerous works study the possible permeation of OMS through the skin site of application [117–119]. To the best of our knowledge, none of these papers reports a direct permeation of particles greater than 10 nm. On the other hand, it is well labelled the possibility for these particles to enter skin pores and hair follicles, enhancing the drug release [117]. In order to observe the OMS-Skin interactions, during the permeation studies, different experiments were stopped at 6, 24, 48 and 72 h (Figure 4.5). Between 6 to 48 h, the OMS particles are in aggregate on the skin. These aggregates are formed during samples preparation for FESEM analysis. However, after 72h, OMS are dispersed in the first 200 μm of thickness and are hardly to be distinguished. Therefore, OMS-Skin interaction is weakly and a long period is required to OMS particles to stick to skin pores and hair follicles.

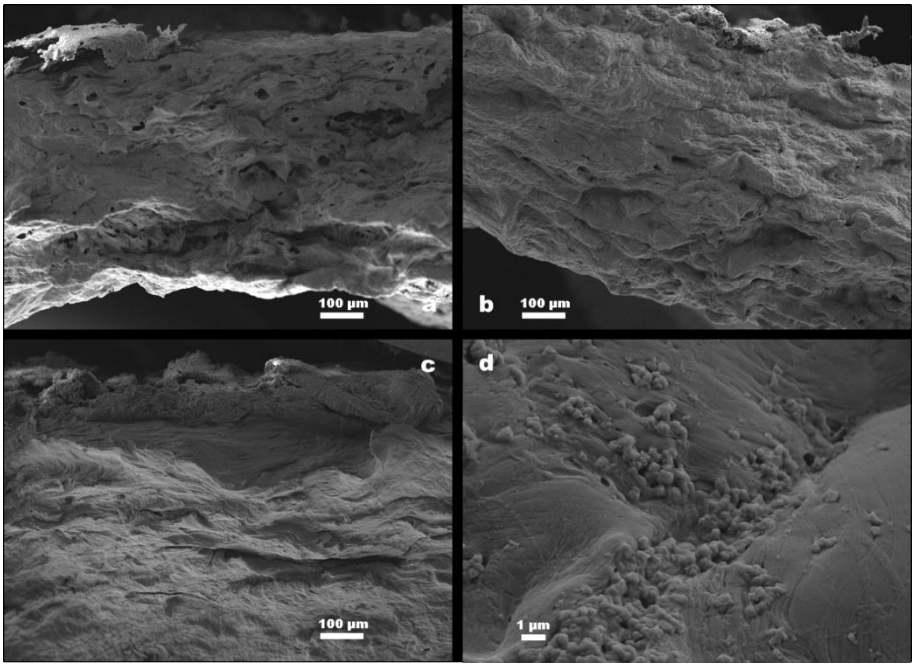

Figure 4.5: FESEM image of the In-vitro permeation test of AKS-OMS gel: 6, 24, 48 and 72h. OMS particles in the form of aggregates are observable very bright in the upper left part of 6h (a), bright in the upper right of 24h (b), hardly visible in the upper part of 48h (c). Image (d) reports the OMS dispersion on the skin after 72h.

CHAPTER 5: CTZ-OMS GEL

ABSTRACT

Controlled drug delivery from Ordered Mesoporous Silica (OMS) platforms represents the possibility to achieve sustained or prolonged drug release in different administration routes widely used, from the oral to the parenteral one [93]. Nevertheless, exploring the literature it is quite evident that much research work have been addressed to investigate OMS nanoparticles as drug delivery system for the oral route, in particular for poorly-water soluble molecules, or for parenteral systems releasing active pharmaceutical ingredients after a triggered external stimuli [10,30,97,120]. To the best of our knowledge, only few papers have been published about the possibility to use silica-based mesoporous nanoparticles for topical application [121–126]. Skin is generally used as route of delivery for local and systemic drugs.

This chapter presents the development and application of the new controlled release system with CTZ. The complete physicochemical characterization of the OMS incorporated with API has been totally described in the previous chapter. Subsequently, in this section are reported only the release tests of different saturated vehicle to ensure the effectiveness of the controlled system. Afterwards, the preparation and characterization of an innovative topical semisolid formulation for CTZ comparable to commercial formulations. Finally, sustained release of CTZ has been developed and outlined with vertical glass diffusion cells.

5.1 SUSTAINED RELEASE OF OMS-CTZ IN CTZ SATURATED SOLUTIONS

In parallel with the sustained release test of AKS, also CTZ has been tested. For CTZ the typical topical creams are between 1 and 2,5% by mass of API content [65]. Therefore, a solution of 1,2-propandiol and water has been studied. The best conditions were with 85% 1,2-propandiol and 15% water by mass. This solution has a saturation point of 25 mg·ml^{-1} that corresponds to 2,4% by mass of API. The same procedure used for AKS has been followed and in figure 5.1 are reported the measured concentration. The concentration decrease only after the complete solubilisation of the incorporated API. Each withdraw of 100 µl contains 2.5 mg of API and the reservoir of OMS-CTZ was 7 mg (70 mg of OMS-CTZ at 10%)

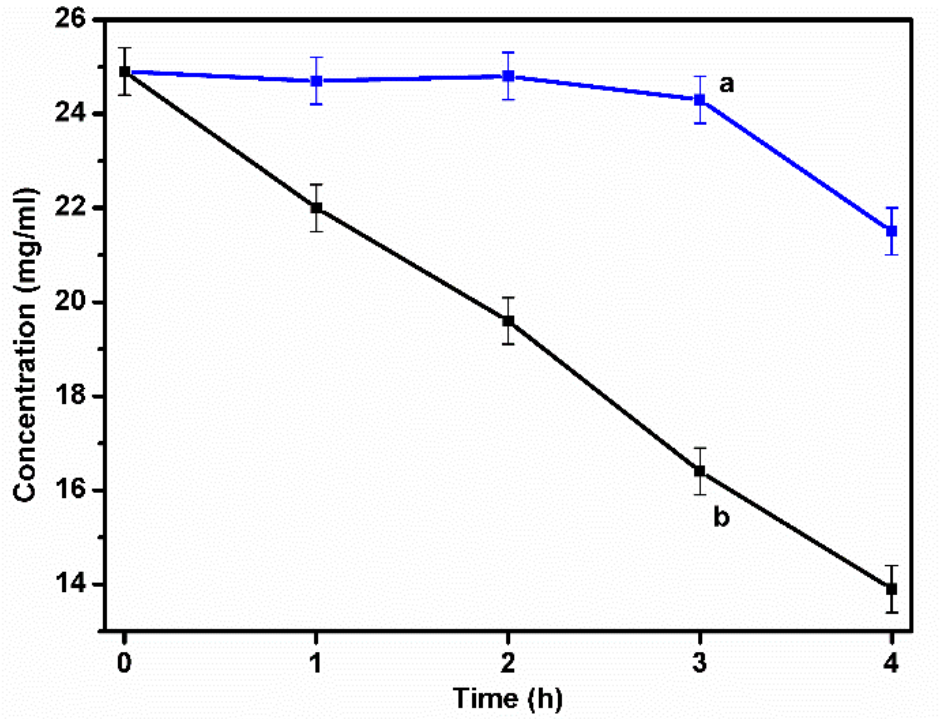

Figure 5.1: CTZ sustained release with 7 mg of API contained in OMS-CTZ (a) and without reservoir (b).

5.2 COMPOSITION AND IN-VITRO RELEASE TEST

A topical semisolid formulation has been prepared and compared to a commercial formulation. In this case the CTZ gel, named CTZ-OMS gel, is a hydrophobic semisolid preparation. It consists of 85% 1,2-propandiol and 15% of bidistilled water. When CTZ is dissolved, 10% by mass OMS-CTZ powder was added to the medium. In this case MSU-H-CTZ-34 has been used. Then, the liquid dispersion was purposely homogenized with a high shear homogenizer for 5 min at maximum velocity. As gelling agent hydroxyethyl cellulose was selected as gelling agent, 2% by mass. The gel shows rheological characteristic of shear-thinning fluid.

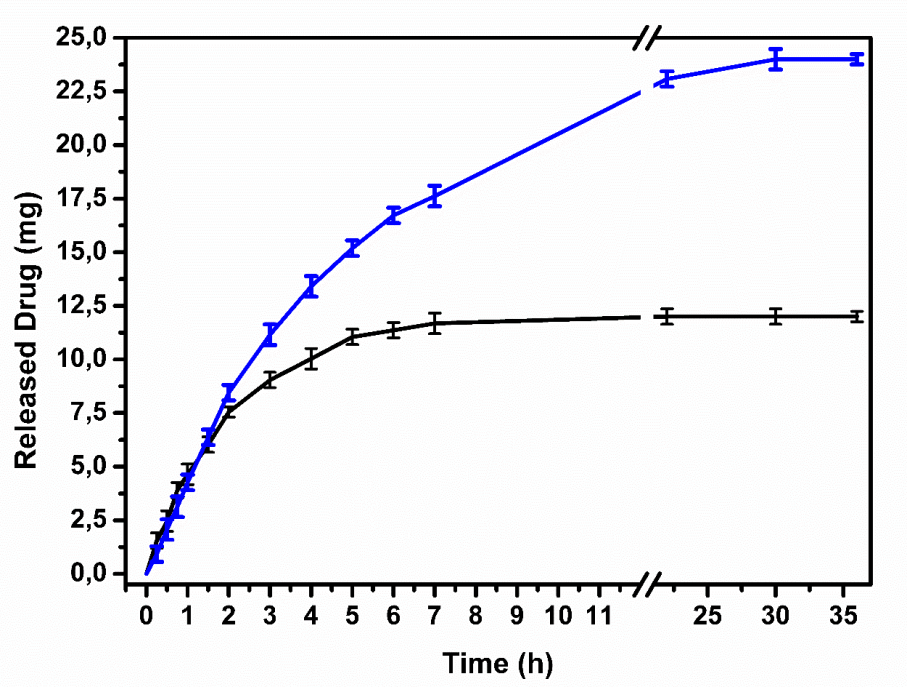

Figure 5.2: In-vitro release test of CTZ-OMS gel (a) and the commercial

formulation (b). Each point is the mean value of three different release tests. The error bars include the maximum variation obtained from all the different trials.

Figure 5.2 reports the in-vitro release curves obtained. In this case, for the first 2h, CTZ-OMS gel follows the commercial formulation. The commercial formulation release rate bends and stops around 5h from the start. On the other hand, CTZ-OMS gel continues almost linearly until 24h.

The constant release rate in the first 2 hours verifies that the starting free concentration of CTZ inside CTZ-OMS gel and the commercial formulation is the same. The preservation of a constant release rate until 5-6 hours proves the capability for CTZ-OMS gel of a sustained release to the therapeutics concentration. Unfortunately, the release rate seems to decrease gradually and not uniformly like the commercial formulation. Probably more tests should be done from 7 to 24 hours in order to control better the release profile of CTZ-OMS gel.

CONCLUSIONS

In this PhD work Ordered Mesoporous Silica has been studied and used for a new controlled release technology for topical applications: starting from the physicochemical characterization to the development of real formulations.

In the first chapter, has been shown the positive and negatives aspects of different incorporation techniques based on hydrophilicity/hydrophobicity of Clotrimazole and Amikacin Sulfate. This have been correlated with dissimilar type of OMS.

With Clotrimazole a theoretical-experimental comparison between results has been done tackling phenomena like: mobility, solubility, bioavailability, etc. All the theoretical and experimental results were in line each other.

Strong of this correlation the differences between types of OMS have been highlighted trying to explain the spatial assembly of drug inside the mesoporous channels of OMS in function of pore dimensions.

Finally, the new controlled release technology has been discussed and demonstrated in its functionality for Clotrimazole and Amikacin Sulfate. Both systems have demonstrated double release time without leaving the therapeutic concentration.

BIBLIOGRAPHY

[1] K. K. Jain, Ed. , *Drug Delivery System*, Springer New York, New York, NY, **2014**.

[2] Y. Perrie, T. Rades, *Pharmaceutics: Drug Delivery and Targeting*, Pharmaceutical Press, **2012**.

[3] N. S. Downing, J. A. Aminawung, N. D. Shah, J. B. Braunstein, H. M. Krumholz, J. S. Ross, *N. Engl. J. Med.* **2012**, *366*, 2284.

[4] M. R. Prausnitz, R. Langer, *Nat. Biotechnol.* **2008**, *26*, 1261.

[5] G. Tiwari, R. Tiwari, B. Sriwastawa, L. Bhati, S. Pandey, P. Pandey, S. K. Bannerjee, *Int. J. Pharm. Investig.* **2012**, *2*, 2.

[6] Y. Ozsoy, S. Gungor, E. Cevher, *Molecules* **2009**, *14*, 3754.

[7] M. Vallet-Regí, F. Balas, D. Arcos, *Angew. Chem. Int. Ed. Engl.* **2007**, *46*, 7548.

[8] A. Gignone, L. Manna, S. Ronchetti, M. Banchero, B. Onida, *Micropor. Mesopor. Mat.* **2014**, *200*, 291.

[9] J. W. Rasmussen, E. Martinez, P. Louka, D. G. Wingett, *Expert Opin. Drug Deliv.* **2010**, *7*, 1063.

[10] R. J. Ahern, J. P. Hanrahan, J. M. Tobin, K. B. Ryan, A. M. Crean, *Eur. J. Pharm. Sci.* **2013**, *50*, 400.

[11] B. A. Lipsky, C. Hoey, *Clin. Infect. Dis.* **2009**, *49*, 1541.

[12] S. C. Gad, *Pharmaceutical Manufacturing Handbook: Production and Processes*, Wiley, **2008**.

[13] F. Hashim, M. El-Ridy, M. Nasr, Y. Abdallah, *Drug Deliv.* **2010**, *17*, 282.

[14] A. H. Faraji, P. Wipf, *Bioorg. Med. Chem.* **2009**, *17*, 2950.

[15] C. Koike, R. Noguchi, H. Chihara, H. Suto, O. Ohtaka, Y. Imai, T. Matsumoto, A. Tsuchiyama, *Astrophys. J.* **2013**, *778*, 60.

[16] V.-P. Lehto, T. Heikkilä, J. Riikonen, E. Mäkilä, J. Salonen, J. Hirvonen, T. Laaksonen, L. Peltonen, H. Santos, **n.d.**

[17] Q. Cai, Z.-S. Luo, W.-Q. Pang, Y.-W. Fan, X.-H. Chen, F.-Z. Cui, *Chem. Mater.* **2001**, *13*, 258.

[18] W. Li, D. Zhao, *Chem. Commun. (Camb).* **2013**, *49*, 943.

[19] S. S. Kim, A. Karkamkar, T. J. Pinnavaia, M. Kruk, M. Jaroniec, *J. Phys. Chem. B* **2001**, *105*, 7663.

[20] M. Grün, K. K. Unger, A. Matsumoto, K. Tsutsumi, *Microporous Mesoporous Mater.* **1999**, *27*, 207.

[21] F. Kleitz, M. Thommes, V. La, **2010**, *19*, 9344.

[22] M. Thommes, R. Köhn, M. Fröba, M. Fro, M. Thommes, R. Ko, *Appl. Surf. Sci.* **2002**, *196*, 239.

[23] D. Zhao, J. Feng, Q. Huo, N. Melosh, G. H. Fredrickson, B. F. Chmelka, G. D. Stucky, *Science (80-.).* **1998**, *279*, 548.

[24] L. Cao, M. Kruk, *J. Colloid Interface Sci.* **2011**, *361*, 472.

[25] T. Seki, T. Ikariya, *Phys. Chem. Chem. Phys.* **2009**, *11*, 10073.

[26] L. F. Giraldo, B. L. López, L. Pérez, S. Urrego, L. Sierra, M. Mesa, *Macromol. Symp.* **2007**, *258*, 129.

[27] I. I. Slowing, J. L. Vivero-Escoto, C.-W. Wu, V. S.-Y. Lin, *Adv. Drug Deliv. Rev.* **2008**, *60*, 1278.

[28] M. Vallet-Regí, *Chem.- Eur. J.* **2006**, *12*, 5934.

[29] I. Izquierdo-Barba, A. Martinez, A. L. Doadrio, J. Pérez-Pariente, M. Vallet-Regí, *Eur. J. Pharm. Sci.* **2005**, *26*, 365.

[30] M. Manzano, V. Aina, C. O. Areán, F. Balas, V. Cauda, M. Colilla, M. R. Delgado, M. Vallet-Regí, *Chem. Eng. J.* **2008**, *137*, 30.

[31] C.-Y. Lai, B. G. Trewyn, D. M. Jeftinija, K. Jeftinija, S. Xu, S. Jeftinija, V. S.-Y. Lin, *J. Am. Chem. Soc.* **2003**, *125*, 4451.

[32] A. Yamamoto, T. Iseki, M. Ochi-Sugiyama, N. Okada, T. Fujita, S. Muranishi, *J. Control. Release* **2001**, *76*, 363.

[33] M. Vallet-Regì, A. Rámila, R. P. Del Real, J. Pérez-Pariente, *Chem. Mater.* **2001**, *13*, 308.

[34] F. Balas, M. Manzano, P. Horcajada, M. Vallet-Regí, *J. Am. Chem. Soc.* **2006**, *128*, 8116.

[35] J. C. Doadrio, E. M. B. Sousa, I. Izquierdo-Barba, A. L. Doadrio, J. Perez-Pariente, M. Vallet-Regí, *J. Mater. Chem.* **2006**, *16*, 462.

[36] S. Giri, B. G. Trewyn, M. P. Stellmaker, V. S.-Y. Lin, *Angew. Chem. Int. Ed. Engl.* **2005**, *44*, 5038.

[37] F. Torney, B. G. Trewyn, V. S.-Y. Lin, K. Wang, *Nat. Nanotechnol.* **2007**, *2*, 295.

[38] N. K. Mal, M. Fujiwara, Y. Tanaka, *Nature* **2003**, *421*, 350.

[39] J. Lu, M. Liong, J. I. Zink, F. Tamanoi, *Small* **2007**, *3*, 1341.

[40] R. Mellaerts, C. a Aerts, J. Van Humbeeck, P. Augustijns, G. Van

den Mooter, J. a Martens, *Chem. Commun.* **2007**, 1375.

[41] V. Ambrogi, F. Marmottini, C. Pagano, *Micropor. Mesopor. Mat.* **2013**, *177*, 1.

[42] T. Azais, C. Tourne-Peteilh, F. Aussenac, N. Baccile, C. Coelho, J. M. Devoisselle, F. Babonneau, M. Curie, L. Chimie, D. Matie, B. Biospin, T. Azais, C. Tourne-Peteilh, F. Aussenac, N. Baccile, C. Coelho, J. M. Devoisselle, F. Babonneau, *Chem. Mater.* **2006**, *18*, 6382.

[43] F. Guenneau, K. Panesar, A. Nossov, M.-A. Springuel-Huet, T. Azaïs, F. Babonneau, C. Tourné-Péteilh, J.-M. Devoisselle, A. Gédéon, *Phys. Chem. Chem. Phys.* **2013**, *15*, 18805.

[44] J. M. Rosenholm, M. Lindén, *J. Control. Release* **2008**, *128*, 157.

[45] H. A. Santos, E. Mäkilä, A. J. Airaksinen, L. M. Bimbo, J. Hirvonen, *Nanomedicine (Lond).* **2014**, *9*, 535.

[46] J. Salonen, A. M. Kaukonen, J. Hirvonen, V.-P. Lehto, *J. Pharm. Sci.* **2008**, *97*, 632.

[47] J. Haber, J. H. Block, B. Delmon, *Pure Appl. Chem.* **1995**, *67*, 1257.

[48] R. Mellaerts, J. a G. Jammaer, M. Van Speybroeck, C. Hong, J. Van Humbeeck, P. Augustijns, G. Van Den Mooter, J. a. Martens, *Langmuir* **2008**, *24*, 8651.

[49] M. E. M. Braga, M. T. V. Pato, H. S. R. C. Silva, E. I. Ferreira, M. H. Gil, C. M. M. Duarte, H. C. de Sousa, *J. Supercrit. Fluids* **2008**, *44*, 245.

[50] R. Span, W. Wagner, *J. Phys. Chem. Ref. Data* **1996**, *25*, 1509.

[51] P. York, *Pharm. Sci. Technolo. Today* **1999**, *2*, 430.

[52] J. Fages, H. Lochard, J.-J. Letourneau, M. Sauceau, E. Rodier, *Powder Technol.* **2004**, *141*, 219.

[53] I. Pasquali, R. Bettini, *Int. J. Pharm.* **2008**, *364*, 176.

[54] N. L. Rozzi, R. K. Singh, *Compr. Rev. Food Sci. Food Saf.* **2002**, *1*, 33.

[55] J. L. Silva, A. C. Oliveira, T. C. R. G. Vieira, G. A. P. de Oliveira, M. C. Suarez, D. Foguel, *Chem. Rev.* **2014**, *114*, 7239.

[56] M. D. A. Saldaña, R. S. Mohamed, M. G. Baer, P. Mazzafera, *J. Agric. Food Chem.* **1999**, *47*, 3804.

[57] I. Smirnova, J. Mamic, W. Arlt, **2003**, 8521.

[58] V. KUMAR, N. P. SUH, *Polym. Eng. Sci.* **n.d.**, *30*, 1323.

[59] M. Bhamidipati, A. M. Scurto, M. S. Detamore, *Tissue Eng. Part B. Rev.* **2013**, *19*, 221.

[60] K. S. Paudel, M. Milewski, C. L. Swadley, N. K. Brogden, P. Ghosh, A. L. Stinchcomb, *Ther. Deliv.* **2010**, *1*, 109.

[61] P. Gupta, S. Garg, *Pharm. Technol.* **2002**.

[62] W. Montagna, *The Structure and Function of Skin 3E*, Elsevier, **2012**.

[63] W. Arnould-Taylor, *A Textbook of Anatomy and Physiology*, Nelson Thornes, **1998**.

[64] R. J. Scheuplein, I. H. Blank, *Physiol. Rev.* **1971**, *51*, 702.

[65] P. R. Sawyer, R. N. Brogden, R. M. Pinder, T. M. Speight, Avery, *Drugs* **1975**, *9*, 424.

[66] H. Song, H.-S. Shin, *Acta Crystallogr. Sect. C Cryst. Struct. Commun.* **1998**, *54*, 1675.

[67] P. M. Monteleone, N. Muhammad, R. D. Brown, J. P. McGrory, S. A. Hanna, in *Anal. Profiles Drug Subst.* (Ed: K. Florey), Academic Press, **1983**, pp. 37–71.

[68] S. K. Jana, R. Nishida, K. Shindo, T. Kugita, S. Namba, *Microporous Mesoporous Mater.* **2004**, *68*, 133.

[69] F. Kleitz, S. H. Choi, R. Ryoo, *Chem. Commun. (Camb).* **2003**, 2136.

[70] S. P. Verevkin, R. V. Ralys, D. H. Zaitsau, V. N. Emel'yanenko, C. Schick, *Thermochim. Acta* **2012**, *538*, 55.

[71] D. M. Price, *Thermochim. Acta* **2001**, *367*, 253.

[72] J. S. Chickos, S. Hosseini, D. G. Hesse, J. F. Liebman, *Struct. Chem.* **1993**, *4*, 271.

[73] O. N. Antzutkin, S. C. Shekar, M. H. Levitt, *J. Magn. Reson. Ser. A* **1995**, *115*, 7.

[74] O. N. Antzutkin, Y. K. Lee, M. H. Levitt, *J. Magn. Reson.* **1998**, *135*, 144.

[75] M. Banchero, L. Manna, S. Ronchetti, P. Campanelli, A. Ferri, *J. Supercrit. Fluids* **2009**, *49*, 271.

[76] R. Dovesi, R. Orlando, A. Erba, C. M. Zicovich-Wilson, B. Civalleri, S. Casassa, L. Maschio, M. Ferrabone, M. De La Pierre, P. D'Arco, Y. Noël, M. Causà, M. Rérat, B. Kirtman, *Int. J.*

Quantum Chem. **2014**, *114*, 1287.

[77] R. Orlando, M. Delle Piane, I. J. Bush, P. Ugliengo, M. Ferrabone, R. Dovesi, *J. Comput. Chem.* **2012**, *33*, 2276.

[78] M. Delle Piane, M. Corno, P. Ugliengo, *J. Chem. Theory Comput.* **2013**, *9*, 2404.

[79] J. P. Perdew, K. Burke, M. Ernzerhof, *Phys. Rev. Lett.* **1996**, *77*, 3865.

[80] S. Grimme, *J. Comput. Chem.* **2006**, *27*, 1787.

[81] A. Schafer, H. Horn, R. Ahlrichs, *J. Chem. Phys.* **1992**, *97*, 2571.

[82] R. Nada, J. B. Nicholas, M. I. McCarthy, A. C. Hess, *Int. J. Quantum Chem.* **1996**, *60*, 809.

[83] E. Apra, M. Causa, M. Prencipe, R. Dovesi, V. R. Saunders, *J. Phys. Condens. Matter* **1993**, *5*, 2969.

[84] M. Delle Piane, M. Corno, A. Pedone, R. Dovesi, P. Ugliengo, *J. Phys. Chem. C* **2014**, *118*, 26737.

[85] S. Dall'Olio, R. Dovesi, R. Resta, *Phys. Rev. B* **1997**, *56*, 10105.

[86] J. Hutter, M. Iannuzzi, F. Schiffmann, J. VandeVondele, *Wiley Interdiscip. Rev. Comput. Mol. Sci.* **2014**, *4*, 15.

[87] J. VandeVondele, M. Krack, F. Mohamed, M. Parrinello, T. Chassaing, J. Hutter, *Comput. Phys. Commun.* **2005**, *167*, 103.

[88] S. Goedecker, M. Teter, J. Hutter, *Phys. Rev. B* **1996**, *54*, 1703.

[89] J. VandeVondele, J. Hutter, *J. Chem. Phys.* **2007**, *127*, 114105.

[90] G. Bussi, D. Donadio, M. Parrinello, *J. Chem. Phys.* **2007**, *126*, 014101.

[91] A. Herskowitz, N. Ishii, H. Schaumburg, *N. Engl. J. Med.* **1971**, *285*, 82.

[92] P. S. S. Spencer, H. H. H. Schaumburg, *Proc. R. Soc. Med.* **1977**, *70*, 37.

[93] C. Charnay, S. Bégu, C. Tourné-Péteilh, L. Nicole, D. a. Lerner, J. M. Devoisselle, *Eur. J. Pharm. Biopharm.* **2004**, *57*, 533.

[94] F. Belhadj-Ahmed, E. Badens, P. Llewellyn, R. Denoyel, G. Charbit, *J. Supercrit. Fluids* **2009**, *51*, 278.

[95] M. Ni, Q.-Q. Xu, J.-Z. Yin, *J. Mater. Res.* **2012**, *27*, 2902.

[96] J. G. Hoogerheide, B. E. Wyka, in *Anal. Profiles Drug Subst.*, **1982**, pp. 225–255.

[97] R. Mellaerts, R. Mols, J. a G. Jammaer, C. A. Aerts, P. Annaert, J. Van Humbeeck, G. Van den Mooter, P. Augustijns, J. A. Martens, *Eur. J. Pharm. Biopharm.* **2008**, *69*, 223.

[98] V. Ambrogi, L. Perioli, F. Marmottini, O. Accorsi, C. Pagano, M. Ricci, C. Rossi, *Micropor. Mesopor. Mat.* **2008**, *113*, 445.

[99] A. Gignone, M. Delle Piane, M. Corno, P. Ugliengo, B. Onida, *J. Phys. Chem. C* **2015**, *119*, 13068.

[100] K. K. Qian, R. H. Bogner, *J. Pharm. Sci.* **2012**, *101*, 444.

[101] R. Bau, I. Tsyba, *Tetrahedron* **1999**, *55*, 14839.

[102] M. Impéror-Clerc, P. Davidson, A. Davidson, *J. Am. Chem. Soc.* **2000**, *122*, 11925.

[103] M. Sliwinska-Bartkowiak, G. Dudziak, R. Gras, R. Sikorski, R. Radhakrishnan, K. E. Gubbins, *Colloids Surfaces A Physicochem. Eng. Asp.* **2001**, *187-188*, 523.

[104] K. K. Qian, W. Zhou, X. M. Xu, T. J. Udovic, *Pharm. Res.* **2012**, *29*, 2432.

[105] P. Ugliengo, M. Sodupe, F. Musso, I. J. Bush, R. Orlando, R. Dovesi, *Adv. Mater.* **2008**, *20*, 4579.

[106] L. T. Zhuravlev, *Langmuir* **1987**, *3*, 316.

[107] M. L. Connolly, *J. Am. Chem. Soc.* **1985**, *107*, 1118.

[108] W. S. Cheow, T. Y. Kiew, Y. Yang, K. Hadinoto, *Mol. Pharm.* **2014**, *11*, 1611.

[109] Y. K. Bae, O. H. Han, *Microporous Mesoporous Mater.* **2007**, *106*, 304.

[110] F. Carniato, G. Paul, C. Bisio, S. Caldarelli, L. Marchese, *RSC Adv.* **2012**, *2*, 1153.

[111] B. Grünberg, T. Emmler, E. Gedat, I. Shenderovich, G. H. Findenegg, H.-H. Limbach, G. Buntkowsky, *Chemistry* **2004**, *10*, 5689.

[112] I. G. Shenderovich, G. Buntkowsky, A. Schreiber, E. Gedat, S. Sharif, J. Albrecht, N. S. Golubev, G. H. Findenegg, H.-H. Limbach, *J. Phys. Chem. B* **2003**, *107*, 11924.

[113] M. Delle Piane, S. Vaccari, M. Corno, P. Ugliengo, *J. Phys. Chem. A* **2014**, *118*, 5801.

[114] F. R. Hu, I. J. Wang, *Curr. Eye Res.* **1998**, *17*, 478.

[115] J. El-On, G. P. Jacobs, E. Witztum, C. L. Greenblatt, *Antimicrob.*

Agents Chemother. **1984**, *26*, 745.

[116] "Handbook of Pharmaceutical Excipients Seventh edition," can be found under http://www.pharmpress.com/product/9780857110275/excipients, **n.d.**

[117] T. W. Prow, J. E. Grice, L. L. Lin, R. Faye, M. Butler, W. Becker, E. M. T. Wurm, C. Yoong, T. A. Robertson, H. P. Soyer, M. S. Roberts, *Adv. Drug Deliv. Rev.* **2011**, *63*, 470.

[118] C. S. J. Campbell, L. R. Contreras-Rojas, M. B. Delgado-Charro, R. H. Guy, *J. Control. Release* **2012**, *162*, 201.

[119] A. C. Watkinson, A. L. Bunge, J. Hadgraft, M. E. Lane, *Pharm. Res.* **2013**, *30*, 1943.

[120] M. Manzano, M. Colilla, M. Vallet-Regí, *Expert Opin. Drug Deliv.* **2009**, *6*, 1383.

[121] S. Sapino, E. Ugazio, L. Gastaldi, I. Miletto, G. Berlier, D. Zonari, S. Oliaro-Bosso, *Eur. J. Pharm. Biopharm.* **2015**, *89*, 116.

[122] C. Dianzani, G. P. Zara, G. Maina, P. Pettazzoni, S. Pizzimenti, F. Rossi, C. L. Gigliotti, E. S. Ciamporcero, M. Daga, G. Barrera, *Biomed Res. Int.* **2014**, *2014*, 13.

[123] M. Pilloni, G. Ennas, M. Casu, A. M. Fadda, F. Frongia, F. Marongiu, R. Sanna, A. Scano, D. Valenti, C. Sinico, *Pharm. Dev. Technol. 18*, 626.

[124] G. Berlier, L. Gastaldi, E. Ugazio, I. Miletto, P. Iliade, S. Sapino, *J. Colloid Interface Sci.* **2013**, *393*, 109.

[125] Y. Antsiferova, N. Sotnikova, E. Parfenyuk, *Biomed Res. Int.* **2013**, *2013*, 10.

[126] L. Gastaldi, E. Ugazio, S. Sapino, P. Iliade, I. Miletto, G. Berlier, *Phys. Chem. Chem. Phys.* **2012**, *14*, 11318.

APPENDIX I – LIST OF PUBBLICATIONS AND CONGRESS

PUBLICATIONS

- Gignone, A.; Manna, L.; Ronchetti, S.; Banchero, M.; Onida, B. Incorporation of clotrimazole in Ordered Mesoporous Silica by supercritical CO_2. Microporous and Mesoporous Materials, 2014, 200, 291-296.
- Gignone, A.; Delle Piane, M.; Corno, M.; Ugliengo, P.; Onida, B. Simulation and Experiment Reveal a Complex Scenario for the Adsorption of an Antifungal Drug in Ordered Mesoporous Silica
- Sustained release of Active Pharmaceutical Ingredients from Ordered Mesoporous Silica (in Preparation)
- Topical administration of Amikacin through OMS (in Preparation)

CONGRESS

- Sustained Release of Amikacin from Ordered Mesoporous Silica. International Congress: Euro-Asia 2015 Zeolite Conference. Nice (France) 25-28 January 2015
- Theoretical and experimental investigation of clotrimazole inside SBA-15. International Congress: 6th International FEZA Conference. Leipzig (Germany) 08-11 September 2014
- Incorporation of Clotrimazole in Ordered Mesoporous Silica by Supercritical CO_2. National Congress: XVII National Congress of Catalysis GIC 2013 and XI National Congress of Zeolites Science and Technology. Riccione (Italy) 15-18 September 2013

THE JOURNAL OF PHYSICAL CHEMISTRY C

Article

pubs.acs.org/JPCC

Simulation and Experiment Reveal a Complex Scenario for the Adsorption of an Antifungal Drug in Ordered Mesoporous Silica

Andrea Gignone,[†] Massimo Delle Piane,[‡] Marta Corno,[‡] Piero Ugliengo,*[,‡] and Barbara Onida*[,†]

[†]Department of Applied Science and Technology, Politecnico di Torino, Corso Duca degli Abruzzi 24, 10129 Torino, Italy

[‡]Department of Chemistry and NIS, University of Torino, via Pietro Giuria 7, 10125, Torino, Italy

Supporting Information

ABSTRACT: Ordered mesoporous silicas have been widely investigated as drug carriers in several fields, from tissue engineering to cancer therapy. The knowledge of the specific interactions between the surface of mesoporous silicas and drugs is necessary to guide development of new and improved drug delivery systems. However, such knowledge is still scarce, due to the arduous interpretation of experimental results. In this work, we characterize the incorporation of clotrimazole, a common antifungal drug, inside ordered mesoporous silica by means of a joint computational and experimental approach. Experimentally the drug was loaded through supercritical CO_2 and its adsorption investigated through infrared spectroscopy, N_2 adsorption isotherms, and thermogravimetric analysis. Modeling involved static and dynamic Density Functional Theory simulations of clotrimazole adsorbed on realistic models of amorphous silica surfaces. A good agreement between the computational and the experimental results was obtained, concerning the energies of adsorption, the infrared spectra, and the distribution of drug inside the mesopores. However, a complete interpretation of the experimental results was possible only when simultaneously considering all the complex aspects of the drug−silica interaction. Indeed, the combination of both approaches allowed us to describe the drug−silica interface as a mix of multiple interaction configurations, based on a subtle balance of hydrogen bonding and dispersion interactions. Furthermore, at high drug loading, clotrimazole molecules are statistically distributed on the pore walls, forming an adsorbed molecular layer. Finally, notwithstanding the stable interactions, the drug still exhibits a significant mobility at room temperature, moving on a complex potential energy surface, as revealed by molecular dynamics simulations.

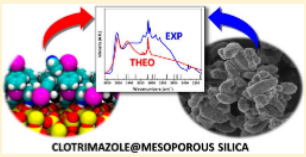

INTRODUCTION

Over the past three decades, a rapid growth has affected the research area of drug delivery, aiming at optimizing drug efficiency while simultaneously reducing adverse collateral effects.[1] Several studies have reported that pharmacokinetics, drug efficiency and suppression of undesired side effects in different pathological conditions can be improved by correct timing of drug administration and controlled kinetics of drug release.[2]

Recently, the interest has concerned the use of mesoporous materials as controlled drug delivery matrixes thanks to their uniform mesoporous structures, high surface areas, tunable pore sizes, and well-defined surface properties.[3−6]

In this context, Ordered Mesoporous Silicas (OMSs) have been widely investigated as drug carriers in several fields, from tissue engineering to cancer therapy.[7] Initially, the research on OMSs for drug delivery was focused on the achievement of controlled release formulations. The release kinetics of drugs by OMSs depends on several carrier properties, including pore size, pore connectivity, and the chemical composition of the surface.[8] A recent emerging feature of OMS carriers is the enhanced oral bioavailability of molecules poorly soluble in water.[9] It has been shown that both small and large molecular drugs can be entrapped within the mesopores by an impregnation process and liberated via a diffusion controlled mechanism.[10]

In the first pioneering work by Vallet-Regi et al.,[4] drug incorporation in MCM-41 was carried out by adsorption from a solution using hexane as solvent. Since the long-term toxicity of *n*-hexane in humans is well-known,[11,12] many other solvents have been studied for the incorporation. The incorporation by supercritical carbon dioxide ($scCO_2$) is an alternative to adsorption or impregnation from a liquid solution.[13−15] Carbon dioxide is one of the most commonly used fluids in supercritical fluid technology. Its main advantages are a critical temperature close to ambient temperature (304.25 K) and a not too high critical pressure (7.39 MPa).[16] In addition, it is nonflammable, has low cost, and has low toxicity. Being a supercritical fluid, its physical properties are halfway between a gas and a liquid; in particular, it has a solvent power like a liquid and a high diffusivity like a gas. At pressures and temperatures not too far from its critical point, a supercritical fluid has a high compressibility; therefore, its density and hence its solvent power are easily adjustable over a wide range with a minimal change in temperature or pressure.

Received: March 19, 2015

DOI: 10.1021/acs.jpcc.5b02666
J. Phys. Chem. C XXXX, XXX, XXX−XXX

When a drug is incorporated inside a material, such as mesoporous silica, the interactions occurring at its surface are of great importance. They can deeply influence stability, absorption, and manufacturability of the formulation[17] and, for drug delivery systems, are essential for determining the final performance of the product, that is, maximum loading, release profile, and shelf life. For these reasons, the development of improved pharmaceutical formulations requires a thorough knowledge of the physicochemical features of these interactions. However, despite the scientific and technological relevance of this topic, the atomistic details of the implied interactions are rarely investigated. Experimentally, most studies deal with ibuprofen as a model drug incorporated in OMSs.[18,19] Nevertheless, the observed ibuprofen behavior might not be applicable to other drugs and this may become a serious problem in the translation from basic research to clinical. Indeed, to our knowledge only few papers deal with the details of other drug−silica interactions.[20,21] Molecular modeling can be an important tool in addressing the problem of studying drug−silica interactions.[22] Some of us have already simulated, through ab initio calculations, ibuprofen interacting with both silica surfaces and a realistic mesoporous silica model, providing a detailed description of the system and some clues to the interpretation of ambiguous experimental results.[23−25]

One of the characteristics of mesoporous silica materials is the presence of a high concentration of silanol groups (SiOH) exposed on the pore walls. It has been shown that the adsorption of molecules on a silica surface (such as the pore walls) is mainly guided by the formation of H-bonds with silanols, but, especially with hydrophobic molecules, also London-type interactions (dispersion) can play an important role.[23]

MSU-H is a two-dimensional, hexagonally OMS with large uniform mesopores synthesized through a nonionic supramolecular assembly pathway using sodium silicate as a silica source and the triblock copolymer Pluronic P123 ($EO_{20}PO_{70}EO_{20}$) as a structure-directing agent. The framework structure of MSU-H is analogous to that of SBA-15 and consists of large ordered pores connected by micropores in the pore walls. Morphology of MSU-H differs from that of SBA-15, in that SBA-15 mesostructures usually assemble into larger and more monolithic particles.[26]

Clotrimazole (CTZ) is an active principle ingredient poorly soluble in water and present in antifungal topical medications for the treatment of fungal infections (of both humans and animals).[27] It is commonly available as an over-the-counter drug in various forms including creams, vaginal tablets, and as troche or throat lozenge. Topically, CTZ is used for vulvovaginal candidiasis (yeast infection) or skin yeast infections. Troche or throat lozenge preparations are used for oropharyngeal candidiasis (oral thrush) or prophylaxis against oral thrush in neutropenic patients. CTZ is usually used 5× daily for 14 days for oral thrush, twice daily for 2−8 weeks for skin infections, and once daily for 3 or 7 days for vaginal infections. For these reasons, finding controlled release system can give a good improvement to pharmaceutical formulations reducing the number of needed applications.[28]

The aim of this work is the investigation of clotrimazole (1-[(2-chlorophenyl)(diphenyl)methyl]-1*H*-imidazole) incorporated inside MSU-H ordered mesoporous material, by means of a joint computational and experimental approach.

In the present work, CTZ is incorporated into MSU-H with $scCO_2$ following a previous work[15] and characterized through Fourier transform infrared spectroscopy (FTIR), N_2 adsorption isotherms, and thermogravimetric analysis (TG). These results are compared and interfaced with static and dynamic quantum mechanical simulations, focused on the interactions between silanols groups and CTZ, evaluating also the contribution of dispersive forces being CTZ a highly hydrophobic molecule. Quantum mechanical modeling is used to help the interpretation of the experimental data, and to obtain a complete description of the MSU-H-CTZ system. Finally, our broader aim is to exploit the knowledge gained on this system for explaining the amorphization, stabilization, and interaction phenomena of drugs on silica surfaces.

■ COMPUTATIONAL AND EXPERIMENTAL DETAILS

Materials. CTZ and Ordered Mesoporous Silica (MSU-H type) were purchased from Sigma-Aldritch. Carbon dioxide with a purity of 99.5% was supplied by SIAD.

Drug Loading. The drug was loaded by the $scCO_2$ incorporation process at 373 K, 50 MPa for 12 h. More details on the $scCO_2$ process are reported in a previous work.[15]

Computational Details. All the calculations were performed within the Density Functional Theory (DFT). Concerning static calculations, the developmental version of the CRYSTAL14 code[29] in its massively parallel version[30] was adopted and the computational approach is the same as ref 23. Briefly, the chosen functional was the Perdew, Burke, and Enzerhof GGA (Generalized Gradient Approximation) exchange-correlation functional (PBE),[31] including the empirical Grimme's D2 correction,[32] to describe the dispersive interactions (vdW). In the following, the superscript D means that Grimme's correction is included. Split valence double- (for Si atoms) and triple-ζ (for other atoms) Gaussian type basis sets plus polarization functions were used to describe the systems.[33,34] Chlorine atoms were represented with a 86-311G* basis set.[35] Only the atomic coordinates of the two more superficial layers of each silica slab in the docking geometries were optimized to compensate for the reduced thickness of the models. Starting geometries were generated so to maximize the interactions between the drug and the surface. Interaction energies, per unit cell per adsorbate molecule (ΔE), were calculated and corrected for the basis set superposition error (BSSE) according to the counter-poise methodology described in previous papers by Delle Piane et al.[23,25] and reported in Supporting Information.

Harmonic frequencies were calculated with CRYSTAL14 at Γ point and the infrared intensity for each normal mode was obtained by computing the dipole moment variation along the normal mode, adopting the Berry phase method.[36] For the simulation of the IR spectra of the different structures, only a fragment consisting of the most interesting chemical groups has been considered for constructing the Hessian matrix and will be defined for each case in Results and Discussion.

Enthalpies (ΔH) of adsorption at standard temperature (298 K) were obtained from the vibrational partition functions, by applying the Zero Point Energies (ΔZPE) and thermal (ΔE_T) corrections to the BSSE corrected electronic adsorption energies (ΔE^C) as $\Delta H = \Delta E^C + \Delta ZPE + \Delta E_T$.

Ab initio molecular dynamics (AIMD) simulations were performed using the CP2K code.[37] The Quickstep technique[38] with a mixed plane wave and Gaussian basis set methodology (Gaussian and Plane Wave method, GPW) was employed to calculate the electronic structure. We used the PBE functional, with the Goedecker−Teter−Hutter pseudopotentials[39] and a

DOI: 10.1021/acs.jpcc.5b02666
J. Phys. Chem. C XXXX, XXX, XXX−XXX

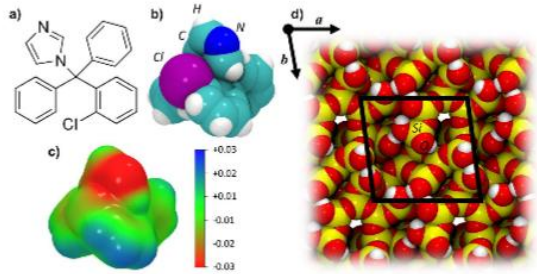

Figure 1. (a) Chemical structure of the CTZ molecule ($H_{17}N_2C_{23}Cl$). (b) 3D space filling model of the CTZ tetrahedral structure with the three phenyl rings almost perpendicular to the imidazole ring. (c) CTZ electrostatic potential mapped on the electron density showing the high electronegativity nature of the external nitrogen in the imidazole ring group. Blue, green, and red colors correspond to positive, neutral, and negative values of the electrostatic potential (range values: MIN, −0.03 au; MAX, +0.03 au). (d) Top view of the amorphous silica surface model used in this paper, cell borders in black (a = 12.6 Å, b = 12.8 Å, and α = 83.1°, $H_{22}O_{63}Si_{26}$).

triple-ζ basis set with polarization functions (TZVP)[40] augmented with the empirical Grimme's D2 correction.[32] The cutoff for the plane wave basis was set to 400 Ry. AIMD simulations were run at 300 K in the NVT ensemble using the Canonical Sampling through Velocity Rescaling (CSVR) thermostat.[41] A time step of 0.5 fs was chosen. All simulations were equilibrated at 300 K with a more stringent thermostat (time constant: 10 fs) for about 1 ps and then the production phase was run for at least 10 ps with a more relaxed thermostat (time constant: 50 fs). Since CP2K requires 3D periodic systems, a value of c = 35 Å was chosen to separate the slab replicas with enough vacuum. In all cases, only the superficial layer of the silica slab and the drug molecules were allowed to move.

Characterization. Samples were characterized by means of Fourier transform infrared spectroscopy (FTIR), nitrogen adsorption isotherms and thermogravimetry (TG) analysis. For FTIR measurements, powders were pressed in self-supporting wafers and spectra were recorded at room temperature with a Bruker Tensor 27 spectrometer operating at 2 cm^{-1} resolution, after outgassing the sample at 373 K for 1 h (residual pressure equal to 0.1 Pa). FTIR spectrum of crystalline CTZ was recorded on the powder dispersed in potassium bromide (KBr). FTIR spectrum of CTZ in solution was recorded on a diluted carbon tetrachloride (CCl_4) solution (1 $g{\cdot}L^{-1}$). Nitrogen adsorption isotherms were measured using a Quantachrome AUTOSORB-1 instrument after degassing at 373 K for 2 h. Brauner−Emmet−Teller (BET) specific surface areas (SSA) were calculated in the relative pressure range 0.04−0.1 and the pore size distribution was determined through the NLDFT (Non Linear Density Functional Theory) method, using the NLDFT equilibrium model for cylindrical pores.[42] TG analyses were carried out between 298 and 1073 K in air (flow rate 100 $mL{\cdot}min^{-1}$ with a heating rate of 10 $K{\cdot}min^{-1}$) using a SETARAM 92 instrument to evaluate the quantity of incorporated drug. The desorption analysis were performed using a SETARAM 92 instrument following the procedure explained by Verevkin et al.[43] and Price et al.[44] Using the Clausius−Clapeyron relation, eq 1, the enthalpies of vaporization (ΔH_{vap}) at the average temperature of investigation were obtained.

$$\ln\left(\sqrt{T}\frac{dm}{dt}\right) = A + \frac{\Delta H_{vap}}{RT} \quad (1)$$

where dm/dt is the mass loss rate at the specified temperature, $kg{\cdot}s^{-1}$, R is the universal gas constant, $J{\cdot}mol^{-1}{\cdot}K^{-1}$, and T is the temperature of the isothermal experiment, K. Subsequently, vaporization enthalpies were reported to 298.15 K using a general methods of correction, reported by Chickos et al. (the Sidgwick's rule):[45]

$$\Delta H_{vap}(298.15) = \Delta H_{vap}(T) + 0.0545(T - 298.15) \quad (2)$$

In eq 2, T is the temperature of measurement or mean temperature of measurement if $\Delta H_{vap}(T)$ has been obtained from a Clausius−Clapeyron treatment of vapor pressures. The experimental conditions used for the reliable determination of vaporization enthalpies of low volatile molecular compounds are following the references of Verevkin at al.[45] A calibration curve with phenol has been done. The uncertainty of temperature calibration was less than 1 K.

RESULTS AND DISCUSSION

Clotrimazole: Molecule and Crystal. CTZ was modeled both in gas phase and as a crystal, before studying its adsorption on amorphous silica. The starting point was the X-ray experimental structure by Song et al.[46] CTZ has a tetrahedral structure (Figure 1a), with the central sp^3 carbon linked to two phenyl rings, one chlorophenyl ring and one imidazole ring. The CTZ molecule, optimized at PBE-D2 level of theory, is reported in Figure 1b. The electrostatic potential mapped on the PBE electron density (Figure 1c) clearly shows the nucleophilic character of the external nitrogen in the imidazole ring group, which is expected to behave as H-bond acceptor when interacting with the surface silanols. The rest of the molecule is generally apolar, as reflected by the experimentally measured low solubility in water (less than 0.01 $g{\cdot}L^{-1}$),[27] and is

DOI: 10.1021/acs.jpcc.5b02666
J. Phys. Chem. C XXXX, XXX, XXX−XXX

expected to engage in dispersive interactions with the silica surface.

The CTZ crystal has been optimized with and without Grimme's correction and compared to experimental results (Figure S1.a and Table S1, in Supporting Information). The structure is triclinic ($P\bar{1}$, a = 8.76 Å, b = 10.55 Å, c = 10.61 Å, and α = 114.1°, β = 97.0°, γ = 97.5°) with two drug molecules per unit cell. If dispersion is not included in the calculation, the cell volume is overestimated by +25.2%, while inclusion of dispersive contributions leads to a cell contraction of −8.4% with respect to single crystal X-ray data.[46] The PBE-D2 cohesive energy of crystalline CTZ has been computed as −146.5 kJ·mol^{-1} (Table 1) and, unsurprisingly, the interactions occurring in the crystal are dominated by dispersion (78%). Indeed, the plain PBE cohesive energy is only −31.8 kJ·mol^{-1}. The corresponding ΔH^{D} at 298 K, including dispersion (obtained from the full set of harmonic frequencies of the crystal), is −131.7 kJ·mol^{-1}.

Table 1. Energetics of the Clotrimazole and MSU-H-CTZ Systems

system	ΔE^{a}	ΔE^{Db}	ΔH^{298c}
clotrimazole bulk^{d}	−31.8	−146.5	−131.7
clotrimazole @ (100)^{e}		−111.3	−104.7
clotrimazole @ (010)		−124.5	−117.1
clotrimazole @ (001)		−118.9	−111.9
imidazole (I)^{f}	−61.5	−134.1	−126.8
imidazole (II)	−58.4	−102.6	−99.1
phenyls (I)	−19.7	−87.6	−80.0
phenyls (II)	−12.3	−78.4	−73.6
molecular layer (I)		−117.1	−101.7
molecular layer (II)		−116.8	−99.5
CTZ bulk EXP. ($-\Delta H_V^{298}$)^{g}			−91.6
CTZ incorporated EXP. ($-\Delta H_V^{298}$)^{h}			−91.8

^{a}Computed (only for selected systems) electronic interaction energy, without accounting for dispersion, corrected for BSSE. ^{b}As ^{a} including dispersion. ^{c}Computed enthalpy of adsorption (dispersion included), at T = 298 K. ^{d}Cohesive energy of crystalline CTZ, computed with respect to a free molecule in gas phase. ^{e}Interaction of one CTZ molecule adsorbed on the (100), (010), and (001) faces of the CTZ crystal. ^{f}CTZ/silica systems: for naming, refer to Figure 2. ^{g}Experimentally measured vaporization enthalpy of CTZ bulk, extrapolated at T = 298 K. ^{h}Experimentally measured vaporization enthalpy of CTZ incorporated in MSU-H, extrapolated at T = 298 K. All values are in kJ·mol^{-1}.

Experimentally, the lack of crystallization of CTZ inside mesoporous silica is observed. Furthermore, mesoporous materials are known to cause amorphization of crystalline drugs. This phenomenon has been described in literature both as a confinement effect[47−50] and as a competition between crystal cohesion and adsorption on the silica surface.[23] To describe this competition, we have modeled the interaction of CTZ molecules with three crystalline surfaces of the same CTZ crystal. The three chosen surfaces were the (100), (010), and (001), which have been modeled through a periodic slab approach with a slab thickness equal to two unit cells. These surfaces represent the three main defect-free crystal faces and were optimized at the PBE-D2 level. The surface energies were 0.10, 0.11, and 0.09 J·m^{-2}, respectively. The adsorption of CTZ on the three crystal surfaces has been simulated by adding one drug molecule in interaction with the slab in the same position occupied in the bulk structure and reoptimizing the structure (Figure S1.b in Supporting Information). The added CTZ molecule maximizes the contact with the surface molecules mainly through dispersion and electrostatics interactions. These are in particular $\pi-\pi$ edge to face interactions of phenyls and chlorophenyls. Other $\pi-\pi$ interactions (e.g., face to face) are not present due to steric hindrance and rigidity of the molecule. Table 1 reports the computed interaction energies of CTZ on the three crystal surfaces together with the corresponding enthalpies at 298 K. Unsurprisingly, the interaction energies of CTZ with its crystal surfaces are comparable to each other with an average value of −113 kJ·mol^{-1}, lower than the crystal cohesive energy (−132 kJ·mol^{-1}) due to the reduced number of intermolecular interactions of the adsorbed drug with the surface compared to those in the bulk.

TG desorption analysis of crystalline CTZ (Table 1) shows an experimental enthalpy of vaporization of about 92 kJ·mol^{-1}, reasonably close to the theoretical values. The comparison between computed and experimental cohesive energy for the CTZ crystal shows some overestimation due to the PBE-D2 method. We proved in the past that the same applies to B3LYP-D2 in the case of molecular crystals and we proposed a slightly different formulation known as B3LYP-D2* which brings computed cohesive energy in better agreement with the experiment. Unfortunately, this correction is not available for PBE-D2 so that we should be aware of a somehow systematic overestimation of the computed data also for the interaction with the surface.[51]

Clotrimazole adsorption on the silica pore wall. Experimentally, CTZ was loaded into MSU-H through $scCO_2$, achieving a maximum drug loading of 34% by mass (vide infra).

In the simulations, CTZ was adsorbed on a silica surface model described in a previous study by some of us[52] and already employed to simulate the adsorption of ibuprofen and aspirin.[23] The use of a flat surface in the present work, at variance with an explicit model of MSU-H, is justified by the curvature of the MSU-H pore, whose diameter (8.5 nm) is much larger than the CTZ molecule: indeed, a flat surface model represents a very good approximation of what the drug is "seeing" inside the pores. This surface is represented in Figure 1d and exhibits a silanol density of 4.5 OH·nm^{-2}, close to the experimentally measured value for fully hydroxylated surfaces (4.9 OH·nm^{-2}).[53] The silica surface model contains 111 atoms in the unit cell (a = 12.6 Å, b = 12.8 Å, and α = 83.1°, cell composition: $H_{22}O_{63}Si_{36}$). The surface exposes eight silanols per unit cell. Of these, only one is free, while the others are interacting through H-bonds. Particularly, three SiOHs cooperates in forming a stable H-bonded chain.

CTZ was manually docked on the surface, aiming at maximizing the interactions between exposed silanols and the different drug's functional groups. In order to match the experimental conditions, six main starting geometries have been studied. Four of them are characterized by one molecule per silica unit cell (drug loading ∼13% by mass), while the other two simulate a molecular layer as observed in previous results[15] with two and three molecules per unit cell (drug loading ∼27% and ∼41% by mass, respectively). All models are shown in top view in Figure 2: (a) imidazole (I) and (b) imidazole (II) are structures with CTZ interacting through its imidazole ring, while in (c) phenyls (I) and (d) phenyls (II), the molecule is adsorbed through its apolar portion; (e) molecular layer (I) and (f) molecular layer (II) are the highest loading structures. The 13% loading models (a−d) have been optimized both with and

DOI: 10.1021/acs.jpcc.5b02666
J. Phys. Chem. C XXXX, XXX, XXX−XXX

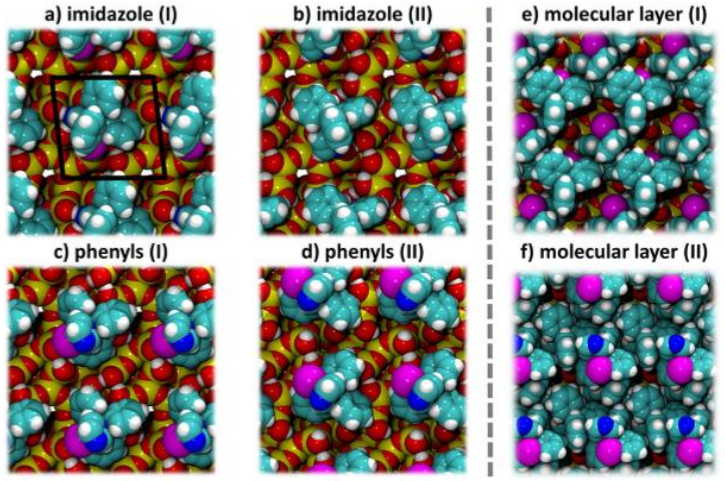

Figure 2. View along the z axis of the fully optimized six different geometries of adsorption. (a) Imidazole (I): Imidazole ring pinched by two silanols; this structure started as chlorine interacting with a silanol, and evolved in a shifted position during geometry optimization, due to the high H-bond acceptor character affinity of imidazole's nitrogen. (b) Imidazole (II): imidazole ring interacting with one ending chain silanol. (c) Phenyls (I): phenyl rings relating with silanols and one SiOH-Cl weak H-bond. (d) Phenyls (II): phenyl rings interacting with silanols. (e) Molecular layer (I): two molecules per silica unit cell. (f) Molecular layer (II): three molecule per unit cell.

without Grimme's dispersion correction to measure the role of dispersion, while for the high loadings, only PBE-D2 has been used.

Interactions between Clotrimazole and the Silica Pore Wall. Figure 3 reports the main types of interactions between CTZ and silanols, as resulted from the simulations. Both the imidazole ring and the chlorophenyl group of CTZ can be involved in H-bonds with the surface hydroxyls (Figure 3a–c), but silanol–π bond interactions are also established (Figure 3d).

The imidazole ring can form both two (Figure 3a) and one (Figure 3b) H-bonds with the surface. In the first case (observed only in the imidazole (I) structure), the imidazole's nitrogen is pinched between two silanols, and the two H-bonds have the same length (1.84 Å, for the imidazole (I) case), suggesting an equivalency of the two interactions. In most cases (imidazole (II) and in the molecular layer geometries), however, CTZ forms only one H-bond through its imidazole ring, usually with the terminal silanol of a H-bonded chain, since these terminal groups are known to be good H-bond donors due to their increased acidity.[22,23,25] Notably, the H-bond length in the imidazole (II) case (1.51 Å) is shorter (and the interaction stronger) than in the imidazole (I) situation (1.84 Å).

In agreement with previous results for other more polar drugs,[25] the pattern of mutual H-bonds between surface silanols

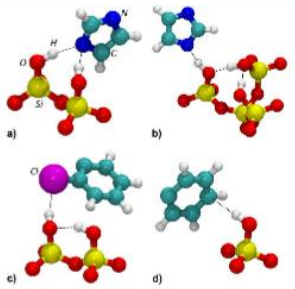

Figure 3. Types of interactions: (a) Imidazole–CTZ double H-bonds (extracted from the imidazole (I) structure). (b) Imidazole–CTZ single H-bond (extracted from the imidazole (II) structure). (c) Chlorophenyl–CTZ interaction (extracted from the phenyls (I) structure). (d) SiOH–π interaction (extracted from the phenyls (II) structure).

DOI: 10.1021/acs.jpcc.5b02666
J. Phys. Chem. C XXXX, XXX, XXX–XXX

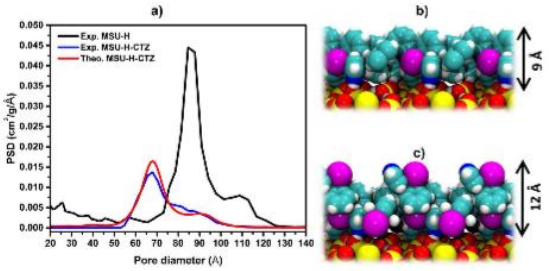

Figure 4. Adsorption model. (a) Comparison of Pore Size Distributions (PSDs) as calculated from the two molecular layer models (red) and as measured before (black) and after (blue) the $scCO_2$ incorporation. (b and c) Side views along the *a* direction of molecular layers (I) and (II), respectively.

is restructured in response to the approach of molecules rich in H-bond donors/acceptors functional groups. This feature is present in all the explored dockings. For instance, in the imidazole (I) case (represented in the local view of Figure 3a), originally the two silanols were interacting with each other. Since a H-bond interaction between vicinal silanols is known to be quite weak,[22] this mutual interaction is easily broken by the incoming CTZ molecule. On the other hand, in cases that include an interaction as reported in Figure 3b, the effect is more subtle: the H-bond with CTZ is able to enhance the interactions toward the imidazole ring along the whole silanol chain.

H-bonds of the Si−O−H···Cl type (Figure 3c) are weaker than those with imidazole (2.24 Å in the phenyls (I) case). Interestingly, in phenyls (I) the distance between the two SiOHs is not perturbed by the new interaction.

Several SiOH−π (surface−CTZ, Figure 3d) have been observed in almost all the different structures, while $\pi-\pi$ edge to face lateral interactions (CTZ−CTZ) characterize the molecular layer models. The mean value of SiOH−π bonds is 2.10 Å, and according to Tsuzuki et al.,[54] the $\pi-\pi$ bonds have a mean value of 4.60 Å. Comparing bond lengths in the different models, we suggest that SiOH−π interactions are halfway between SiOH-N and SiOH-Cl H-bonds, as regards interaction strength.

Energetics of the Clotrimazole−Silica Interaction. Table 1 reports the computed interaction energies with (ΔE^0) and without (ΔE) dispersion (when available) and the adsorption enthalpies at standard temperature (ΔH^{298}), including dispersion.

All simulations reveal that the adsorption of CTZ on amorphous silica is a strongly exothermic process. Nevertheless, different geometries and consequently interaction types correspond to different energies of adsorption, ranging from −134.1 kJ·mol^{-1} for the imidazole (I) case to −78.4 kJ·mol^{-1} for the phenyls (II) geometry.

Comparing ΔE and ΔE^0, London forces constitute the predominant contribution to the interaction in all systems, except for the imidazole (I) case. Of particular interest are the phenyls (I) and (II) structures: in these cases, the interaction energies without dispersion are small, while including vdW interactions increases these energies by more than +400 and +600%, respectively. Dispersion plays a more important role in CTZ adsorption on hydrophilic silica than it has been reported for more polar drugs such as ibuprofen and aspirin.[23,25] For the molecular layer geometries, the average interaction energies (and enthalpies) per molecule have very similar values despite the fact that the third additional molecule in the molecular layer (II) is not involved in H-bonds with the surface. This is a further evidence that, for an apolar molecule, the lateral self-interaction (dispersion-driven) is similar to that of the molecule with the surface. In all cases, the CTZ deformation energies are negligible due to the rigidity of the molecule, with a mean value of 7 kJ·mol^{-1}.

Table 1 reveals that all the computed interaction energies and enthalpies are close to each other, enlightening a possible competition between crystalline and adsorbed CTZ. Assuming that the supercritical incorporation is a step route controlled by dissolution and adsorption of single molecules, this process is almost isoenergetic, since for each adsorption on silica, an average of 110 kJ·mol^{-1} are gained, and for each desorption from the crystal, 115 kJ·mol^{-1} are lost. This could be the explanation of the lack of crystallization in pores smaller than 20× the molecule diameter explained by Sliwinska-Bartkowiak et al.[47] and observed by other authors.[48−50]

TG desorption analysis of CTZ in MSU-H (34% by mass) produces an enthalpy of vaporization of 91.6 kJ·mol^{-1}, as reported in Table 1. As above-mentioned (and also reported in Table 1), a similar analysis on crystalline CTZ results in a value of 91.8 kJ·mol^{-1}. Thus, also the experimental data suggest that the two processes are almost isoenergetic, supporting the hypothesis on silica-induced drug amorphization.

The experimental enthalpy of vaporization for the MSU-H-CTZ case is very close (in absolute value) to the computed adsorption enthalpies for both CTZ molecular layers (−101 kJ·mol^{-1}). The comparison of the experimental value (91.6 kJ·mol^{-1}) with the data obtained for the different low loading geometries suggests which interaction reported in Figure 3 is more represented in the real sample. The closest value is obtained for the imidazole (II) case, that is, adsorption driven by one H-bond between the imidazole group and a surface silanol. On the other hand, situations like imidazole (I),

DOI: 10.1021/acs.jpcc.5b02666
J. Phys. Chem. C XXXX, XXX, XXX−XXX

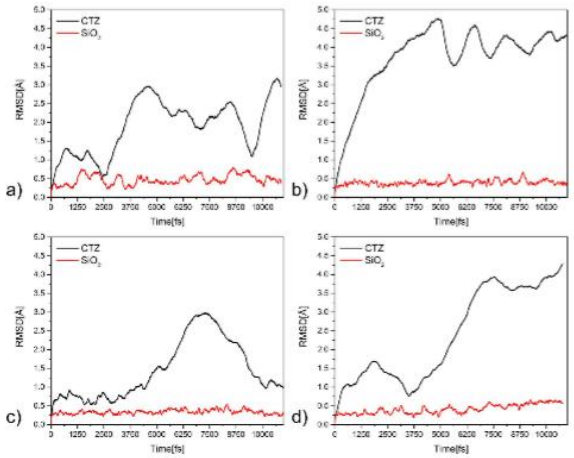

Figure 5. Silica (SiO_2) and clotrimazole (CTZ) RMSD (in Å) with respect to the initial structure for all AIMD simulations. For the silica surface, only the atoms free to move in the simulation have been considered: (a) imidazole (I); (b) phenyls (I); (c) phenyls (II); (d) molecular layer (II). See Figure 3 for the corresponding structural details.

although theoretically very stable, seem to be rarer events in the real material due to the lower hydrophilicity of the experimental silica, the steric hindrance of the molecules, and the low configurational entropy content of this unique configuration. Interestingly, the computed interaction enthalpy of the phenyls (I) model is also quite close to the experimental value, suggesting that phenyls-driven interactions may be present in a significant portion of the adsorbed CTZ population. In summary, all configurations of Figure 3a–d are probably represented in the real sample since their average ΔH^D (−94.9 $kJ \cdot mol^{-1}$) is very close to the experimental measure.

Model of Adsorption: Nitrogen Adsorption and TG Analysis. Experimental N_2 adsorption isotherms (Figure S2.a in Supporting Information), through NonLinear Density Functional Theory (NLDFT), allow the calculation of the experimental pore size distributions (PSDs) before and after the $scCO_2$ incorporation of CTZ. The results are reported in Figure 4a. As expected, drug incorporation reduces the pore diameter from the 86 Å value of bare MSU-H (black line) to a lower value of 67 Å (blue line).

As already described in a previous work by some of us,[15] the drug can be assumed as adsorbed mainly in the form of a molecular layer. Using a bare value of thicknesses of the single molecular layers I and II (Figure 4b,c), the corresponding new PSDs can be calculated (Figure S2.b). Clearly, with this approach, the calculated PSDs are unable to describe the experimental results.

On the other hand, experimental TG analysis reports an incorporated quantity of 34% by mass, which is in between the loading calculated for layer (I) and layer (II), which are ~27% and ~41% by mass, respectively. By calculating the experimental planar concentration of CTZ (molecules per nm^2) and comparing it to our theoretical models of molecular layers (2 CTZs/cell, Figure 2e, and 3 CTZs/cell, Figure 2f), it is shown that the real system can be described by a 50:50 mixture of the two molecular layer geometries. Indeed, the unit cell of the simulated silica surface has an area of 1.6 nm^2 and the experiment reports 2.5 CTZ molecules per 1.6 nm^2. As a consequence, a simulated MSU-H-CTZ PSD has to be calculated, starting from the experimental PSD of bare MSU-H, assuming thicknesses representative of both the molecular layer (I) and (II) models. These thicknesses have been evaluated following the Connolly surfaces[55] before and after CTZ adsorption of the computed models, with the purpose to take into account the vdW molecular volume and the roughness generated by the statistical distribution of 2 and 3 CTZ molecules per 1.6 nm^2. Therefore, the molecular layer surfaces have been discretized in 677 squares (0.25 $Å^2$) in order to evaluate the thicknesses, for each point, between the starting silica model and the molecular layers. Subsequently, a new PSD has been calculated for each couple of evaluated thicknesses and all curves have been combined together in the final theoretical PSD of Figure 4a (red). Such procedure results in an impressive agreement between simulation and experiment, validating the data interpretation.

Mobility of Adsorbed Clotrimazole. Ab Initio Molecular Dynamics (AIMD) has been performed on the different statically optimized geometries in order to evaluate the stability

DOI: 10.1021/acs.jpcc.5b02666
J. Phys. Chem. C XXXX, XXX, XXX−XXX

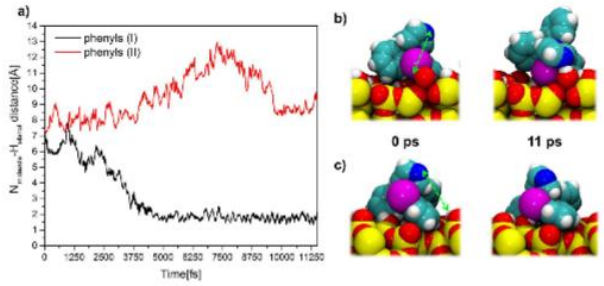

Figure 6. AIMD of phenyls (I) and (II): (a) exposed nitrogen−SiOH distance over time: phenyls (I) in red, phenyls (II) black. (b) 3D space filling models of phenyls (I) at 0 and 11 ps. (c) 3D space filling model of phenyls (II) at 0 and 11 ps. The nitrogen−SiOH distance plotted in the graph is highlighted in green.

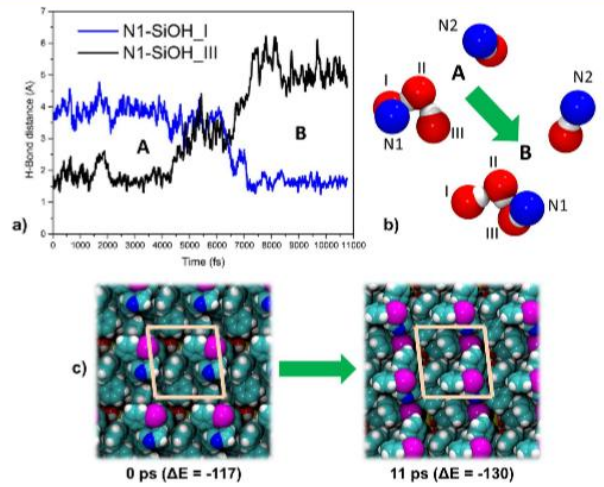

Figure 7. AIMD of the molecular layer (II) structure: (a) N1-SiOH(I) and N1-SiOH(III) bond distances in time. (b) Starting (A) and final (B) positions of N1 and N2 with respect to the involved SiOHs. (c) Top views of the initial (left) and final (right) configurations in the AIMD simulation, with the corresponding interaction energies per CTZ molecule (kJ·mol^{-1}); cell borders in pink.

of the local minimum structures of Figure 2. In Figure 5 the Root Mean Square Deviations (RMSD) of the atomic positions, during the production, with respect to the first frame, are reported for the four AIMD simulations (imidazole (I), phenyls (I), phenyls (II), and molecular layer (II)). RMSDs are separated in the CTZ and silica contributions. In all cases, the mobility of the adsorbed drugs is higher than that of the silica surface. The latter seems equilibrated during all simulations.

The imidazole (I) structure, which is the most stable configuration of CTZ on silica according to Table 1, shows a general stability of the adsorbed molecule during the 11 ps

DOI: 10.1021/acs.jpcc.5b02666
J. Phys. Chem. C XXXX, XXX, XXX−XXX

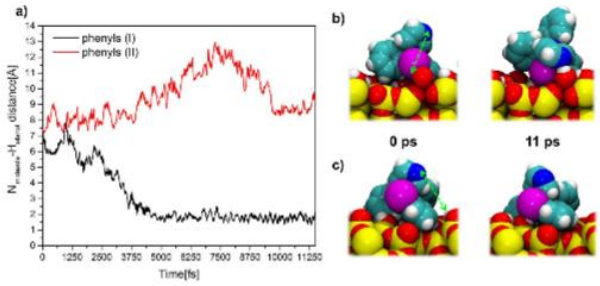

Figure 6. AIMD of phenyls (I) and (II): (a) exposed nitrogen−SiOH distance over time: phenyls (I) in red, phenyls (II) black. (b) 3D space filling models of phenyls (I) at 0 and 11 ps. (c) 3D space filling model of phenyls (II) at 0 and 11 ps. The nitrogen−SiOH distance plotted in the graph is highlighted in green.

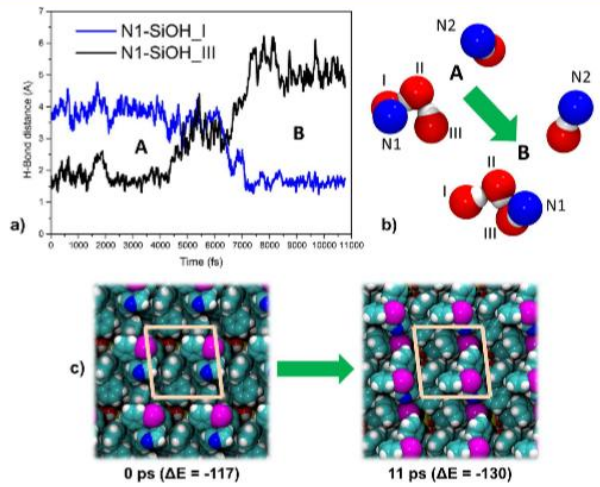

Figure 7. AIMD of the molecular layer (II) structure: (a) N1-SiOH(I) and N1-SiOH(III) bond distances in time. (b) Starting (A) and final (B) positions of N1 and N2 with respect to the involved SiOHs. (c) Top views of the initial (left) and final (right) configurations in the AIMD simulation, with the corresponding interaction energies per CTZ molecule (kJ·mol^{-1}); cell borders in pink.

of the local minimum structures of Figure 2. In Figure 5 the Root Mean Square Deviations (RMSD) of the atomic positions, during the production, with respect to the first frame, are reported for the four AIMD simulations (imidazole (I), phenyls (I), phenyls (II), and molecular layer (II)). RMSDs are separated in the CTZ and silica contributions. In all cases, the mobility of the adsorbed drugs is higher than that of the silica surface. The latter seems equilibrated during all simulations.

The imidazole (I) structure, which is the most stable configuration of CTZ on silica according to Table 1, shows a general stability of the adsorbed molecule during the 11 ps

DOI: 10.1021/acs.jpcc.5b02666
J. Phys. Chem. C XXXX, XXX, XXX−XXX

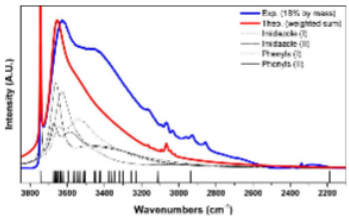

Figure 8. Experimental and simulated IR: experimental FTIR spectrum of MSU-H-CTZ at 18% by mass (blue); theoretical IR spectrum of CTZ combined with SiOH vibrational contribution (red); simulated IR spectrum of SiOH vibrational contribution of imidazole (I) (dot-dashed black line); imidazole (II) (dashed black line); phenyls (I) (dotted black line); phenyls (II) (black line). At the bottom of the graph, sticks represent the theoretical SiO-H stretching frequencies without Pimentel's correction.

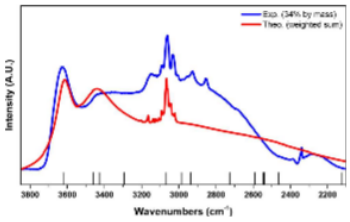

Figure 9. Experimental and simulated IR: experimental FTIR spectrum of MSU-H-CTZ at 34% by mass, after degas (blue); simulated IR spectrum of CTZ combined with SiOH vibrational contribution (red). At the bottom of the graph, sticks represent the theoretical SiO-H stretching frequencies without Pimentel's correction.

Pimentel's empirical rule to account for the broadening effect due to H-bonding.[56] The uncorrected computed SiO-H frequencies have been reported in the lower part of both Figures 8 and 9 as vertical lines. The final theoretical spectra (red lines) of Figures 8 and 9 are then the combination of these SiO-H stretching modes and the CTZ signals. Figure 8 also includes the theoretical spectra computed for the four low loading configurations, limited to the SiO-H stretching modes.

For both the low and high loading cases, the agreement between theory and experiment is remarkable and helps the interpretation of the signals. Considering CTZ modes, the 3175−3100 cm^{-1} experimental bands are due to the ensemble of the C−H symmetric stretching of SiOH-π interacting aromatic rings. Peaks between 3000 and 2800 cm^{-1} are due to alkyl impurities in the silica samples. As regards SiO-H signals, the sharp peak at 3750 cm^{-1} (only in the low loading case) corresponds to isolated silanols. The broad band between 3700 and 3550 cm^{-1} corresponds to the silanol signals of SiOH−π interactions. All silanols signals at lower wavenumbers (3400−2500 cm^{-1}) are due to SiOH−imidazole interactions. As expected, the SiO-H stretching frequency is highly affected by this interaction, with bathochromic shifts up to more than a thousand wavenumbers, as shown by the individual signals reported in both figures (stick lines) and particularly for the high loading case. The higher intensity of this broad band in both experimental spectra of Figure 8 and 9 with respect to the simulation is due to the Pimental's approximation which cannot account for all the subtle features due to anharmonic coupling and intensity stealing between modes in H-bond interactions.

A first effect of increasing the drug loading is the loss of the isolated silanol peak, suggesting that all silanols become involved in interactions (see spectra of Figures 8 and 9). A second result is an intensification of the SiOH−imidazole signals with respect to the SiOH−π ones, suggesting that a decreasing amount of silanols is able to interact with the phenyl groups and an increasing amount of SiOH−imidazole H-bonds is formed. Such behavior seems counterintuitive with respect to the energetics of Table 1: computed ΔH^0s suggest that by increasing drug loading more stable configurations (imidazole-driven) should be populated earlier than less stable ones (phenyls-driven), while FTIR shows that SiOH−phenyls signals are more prominent in the low loading case than the high loading one. This apparent disagreement can be resolved by taking into account the complexity of CTZ adsorption on the silica pore walls. Comparison between computed and experimental enthalpies of adsorption (Table 1) suggests that at least some energetically very stable imidazole-driven interactions (such as that of Figure 3.a) are quite rare in a real sample as they depend on the presence of specific surface sites. Moreover, given the structure of the CTZ molecule, also when it adsorbs through its imidazole ring, more silanols are influenced by its phenyls and chlorophenyls moieties than by the SiOH-N interaction. This can be deduced from the individual simulated spectra of Figure 8, in which signals corresponding to SiOH−π are present in all four configurations, independently of what drives the interaction. Furthermore, the strong bathochromic shift caused by the SiOH-N H-bonds corresponds to a significant signal broadening, so that at low loading these modes are smeared out over the whole spectrum. Finally, AIMD simulations proved that some phenyls-driven adsorptions, although based on relatively weak interactions, are indeed stable at room temperature: given the bulky conformation of CTZ (Figure 1c) such configurations might be highly probable during incorporation, also at low loadings.

■ CONCLUSIONS

We have reported the concurrent experimental and theoretical (both static and dynamic) characterization of a common antifungal drug, clotrimazole (CTZ), incorporated in ordered mesoporous silica of the MSU-H type.

Comparison between experimental and computed interaction energies, pore size distributions, and vibrational spectra resulted in a very good agreement. This suggests that DFT simulation of drug adsorption on realistic amorphous silica surface models can be used to predict the behavior of drugs inside the pores of mesoporous silica materials, provided that a good sampling of the different interactions is achieved.

As regards the MSU-H-CTZ system, results shown here reveal that CTZ is adsorbed, over the incorporation with $scCO_2$, following a homogeneous and statistical distribution on the silica surface. This picture is explained only considering

DOI: 10.1021/acs.jpcc.5b02666
J. Phys. Chem. C XXXX, XXX, XXX−XXX

together the molecular layer models. Thanks to the quantum mechanical simulations, we were able to describe the experimentally measured change in pore size distribution by considering the thickness of the molecular layer at high loading.

Simulations and their comparison with experimental data suggest that CTZ interacts in multiple orientations with the silica surface: the strongest interaction includes an H-bond between the nitrogen atom of the imidazole ring with terminal silanols of H-bonded chains already present on the silica walls, but other H-bonds that involve the phenyl rings and the chlorine atom are also present. Comparison with experiment shows that a very stable configuration found by the simulations is probably quite rare in the real system due to the specificity of the adsorbing sites.

AIMD simulations provided a direct evidence of high mobility of drugs adsorbed into mesoporous silica, supporting experimental results in literature. We also revealed that large displacements parallel to the surface of adsorbed molecular layers may be triggered by local changes in the interactions.

Energetically, it was confirmed that London forces play a key role in drug adsorption on silica and that they are indeed the true driving force of the process in the case of apolar molecules such as CTZ, also assisting the stabilization of molecular layers on the surface. Experimental and theoretical data also agree in that CTZ adsorption on silica and CTZ interaction on its own crystal surfaces are almost isoenergetic processes, thus suggesting a possible explanation for the lack of crystallization inside the pores of MSU-H.

A comprehensive picture of this complex scenario was achieved only through the joint of simulation and experiment and the present methodology paves the way to improve our understanding of the interactions between drugs and delivery systems.

■ ASSOCIATED CONTENT

Supporting Information

Computational details, crystalline structure, surface models, nitrogen adsorption isotherms, AIMD simulations details, FT-IR spectra and bands attribution, absolute energies, fractional coordinates of all the optimized structures, and video of the significant AIMD simulations. The Supporting Information is available free of charge on the ACS Publications website at DOI: 10.1021/acs.jpcc.5b02666.

■ AUTHOR INFORMATION

Corresponding Authors

*E-mail: piero.ugliengo@unito.it.
*E-mail: barbara.onida@polito.it.

Notes

The authors declare no competing financial interest.

■ ACKNOWLEDGMENTS

The vast majority of the calculations have been carried out on the FERMI supercomputer, in Bologna, Italy, thanks to the ISCRA (Italian SuperComputing Resource Allocation) class B projects IBUEXCIP and SIL4SKIN. Models have been visualized and manipulated by MOLDRAW.[57] AIMD simulations have been analyzed through VMD.[58] Figures have been rendered with the Tachyon ray tracer,[59] built into VMD.

■ REFERENCES

(1) Hillery, A. M.; Lloyd, A. W.; Swarbrick, J.; Whateley, T. L. *Drug Delivery and Targeting: For Pharmacists and Pharmaceutical Scientists*; Taylor and Francis: London, 2002; Vol. *10*, pp 637−637.

(2) Manzano, M.; Aina, V.; Areán, C. O.; Balas, F.; Cauda, V.; Colilla, M.; Delgado, M. R.; Vallet-Regí, M. Studies on MCM-41 Mesoporous Silica for Drug Delivery: Effect of Particle Morphology and Amine Functionalization. *Chem. Eng. J.* **2008**, *137*, 30−37.

(3) Song, S.-W.; Hidajat, K.; Kawi, S. Functionalized SBA-15 Materials as Carriers for Controlled Drug Delivery: Influence of Surface Properties on Matrix− Drug Interactions. *Langmuir* **2005**, *21*, 9568−9575.

(4) Vallet-Regi, M.; Rámila, A.; Del Real, R. P.; Pérez-Pariente, J. A New Property of MCM-41: Drug Delivery System. *Chem. Mater.* **2001**, *13*, 308−311.

(5) Tourné-Péteilh, C.; Lerner, D. A.; Charnay, C.; Nicole, L.; Bégu, S.; Devoisselle, J. M. The Potential of Ordered Mesoporous Silica for the Storage of Drugs: The Example of a Pentapeptide Encapsulated in a MSU-Tween 80. *ChemPhysChem* **2003**, *4*, 281−286.

(6) Lai, C.-Y.; Trewyn, B. G.; Jeftinija, D. M.; Jeftinija, K.; Xu, S.; Jeftinija, S.; Lin, V. S.-Y. A Mesoporous Silica Nanosphere-Based Carrier System with Chemically Removable CdS Nanoparticle Caps for Stimuli-Responsive Controlled Release of Neurotransmitters and Drug Molecules. *J. Am. Chem. Soc.* **2003**, *125*, 4451−4459.

(7) Vallet-Regí, M. Ordered Mesoporous Materials in the Context of Drug Delivery Systems and Bone Tissue Engineering. *Chem.—Eur. J.* **2006**, *12*, 5934−5943.

(8) Andersson, J.; Rosenholm, J.; Areva, S.; Lindén, M. Influences of Material Characteristics on Ibuprofen Drug Loading and Release Profiles from Ordered Micro- and Mesoporous Silica Matrices. *Chem. Mater.* **2004**, *16*, 4160−4167.

(9) Mellaerts, R.; Mols, R.; Jammaer, J. A. G.; Aerts, C. A.; Annaert, P.; Van Humbeeck, J.; Van den Mooter, G.; Augustijns, P.; Martens, J. A. Increasing the Oral Bioavailability of the Poorly Water Soluble Drug Itraconazole with Ordered Mesoporous Silica. *Eur. J. Pharm. Biopharm.* **2008**, *69*, 223−230.

(10) Izquierdo-Barba, I.; Martinez, A.; Doadrio, A. L.; Pérez-Pariente, J.; Vallet-Regí, M. Release Evaluation of Drugs from Ordered Three-Dimensional Silica Structures. *Eur. J. Pharm. Sci.* **2005**, *26*, 365−373.

(11) Herskowitz, A.; Ishii, N.; Schaumburg, H. N-Hexane Neuropathy. A Syndrome Occuring as a Result of Industrial Exposure. *N. Engl. J. Med.* **1971**, *285*, 82−85.

(12) Spencer, P. S.; Schaumburg, H. H. Neurotoxic Properties of Certain Aliphatic Hexacarbons. *Proc. R. Soc. Med.* **1977**, *70*, 37−39.

(13) Belhadj-Ahmed, F.; Badens, E.; Llewellyn, P.; Denoyel, R.; Charbit, G. Impregnation of Vitamin E Acetate on Silica Mesoporous Phases Using Supercritical Carbon Dioxide. *J. Supercrit. Fluids* **2009**, *51*, 278−286.

(14) Ni, M.; Xu, Q.-Q.; Yin, J.-Z. Preparation of Controlled Release Nanodrug Ibuprofen Supported on Mesoporous Silica Using Supercritical Carbon Dioxide. *J. Mater. Res.* **2012**, *27*, 2902−2910.

(15) Gignone, A.; Manna, L.; Ronchetti, S.; Banchero, M.; Onida, B. Incorporation of Clotrimazole in Ordered Mesoporous Silica by Supercritical CO_2. *Microporous Mesoporous Mater.* **2014**, *200*, 291−296.

(16) Span, R.; Wagner, W. A New Equation of State for Carbon Dioxide Covering the Fluid Region from the Triple-Point Temperature to 1100 K at Pressures up to 800 MPa. *J. Phys. Chem. Ref. Data* **1996**, *25*, 1509−1596.

(17) Pifferi, G.; Restani, P. The Safety of Pharmaceutical Excipients. *Farmaco* **2003**, *58*, 541−550.

(18) Azais, T.; Tourne-Peteilh, C.; Aussenac, F.; Baccile, N.; Coelho, C.; Devoisselle, J. M.; Babonneau, F. Solid-State NMR Study of Ibuprofen Confined in MCM-41 Material. *Chem. Mater.* **2006**, *18*, 6382−6390.

(19) Guenneau, F.; Panesar, K.; Nossov, A.; Springuel-Huet, M.-A.; Azais, T.; Babonneau, F.; Tourné-Péteilh, C.; Devoisselle, J.-M.; Gédéon, A. Probing the Mobility of Ibuprofen Confined in MCM-41

DOI: 10.1021/acs.jpcc.5b02666
J. Phys. Chem. C XXXX, XXX, XXX−XXX

Materials Using MAS-PFG NMR and Hyperpolarised-Xe-129 NMR Spectroscopy. *Phys. Chem. Chem. Phys.* **2013**, *15*, 18805−18808.
(20) Mellaerts, R.; Roeffaers, M. B. J.; Houthoofd, K.; Van Speybroeck, M.; De Cremer, G.; Jammaer, J. A. G.; Van den Mooter, G.; Augustijns, P.; Hofkens, J.; Martens, J. A. Molecular Organization of Hydrophobic Molecules and Co-Adsorbed Water in SBA-15 Ordered Mesoporous Silica Material. *Phys. Chem. Chem. Phys.* **2011**, *13*, 2706−2713.
(21) Morais, E. C.; Correa, G. G.; Brambilla, R.; Radtke, C.; Baibich, I. M.; dos Santos, J. H. Z. The Interaction of Encapsulated Pharmaceutical Drugs with a Silica Matrix. *Colloids Surf., B* **2013**, *103*, 422−429.
(22) Rimola, A.; Costa, D.; Sodupe, M.; Lambert, J.-F.; Ugliengo, P. Silica Surface Features and Their Role in the Adsorption of Biomolecules: Computational Modeling and Experiments. *Chem. Rev.* **2013**, *113*, 4216−4313.
(23) Delle Piane, M.; Corno, M.; Ugliengo, P. Does Dispersion Dominate over H-Bonds in Drug−Surface Interactions? The Case of Silica-Based Materials As Excipients and Drug-Delivery Agents. *J. Chem. Theory Comput.* **2013**, *9*, 2404−2415.
(24) Delle Piane, M.; Vaccari, S.; Corno, M.; Ugliengo, P. Silica-Based Materials as Drug Adsorbents: First Principle Investigation on the Role of Water Microsolvation on Ibuprofen Adsorption. *J. Phys. Chem. A* **2014**, *118*, 5801−5807.
(25) Delle Piane, M.; Corno, M.; Pedone, A.; Dovesi, R.; Ugliengo, P. Large-Scale B3LYP Simulations of Ibuprofen Adsorbed in MCM-41 Mesoporous Silica as Drug Delivery System. *J. Phys. Chem. C* **2014**, *118*, 26737−26749.
(26) Kim, S. S.; Karkamkar, A.; Pinnavaia, T. J.; Kruk, M.; Jaroniec, M. Synthesis and Characterization of Ordered, Very Large Pore MSU-H Silicas Assembled from Water-Soluble Silicates. *J. Phys. Chem. B* **2001**, *105*, 7663−7670.
(27) Hoogerheide, J. G.; Wyka, B. E. Clotrimazole. In *Analytical Profiles of Drug Substances*; Elsevier: New York, 1982; Vol. *11*, pp 225−255.
(28) Borgers, M. Mechanism of Action of Antifungal Drugs, with Special Reference to the Imidazole Derivatives. *Rev. Infect. Dis.* **1980**, *2*, 520−534.
(29) Dovesi, R.; Orlando, R.; Erba, A.; Zicovich-Wilson, C. M.; Civalleri, B.; Casassa, S.; Maschio, L.; Ferrabone, M.; De La Pierre, M.; D'Arco, P.; et al. CRYSTAL14: A Program for the Ab Initio Investigation of Crystalline Solids. *Int. J. Quantum Chem.* **2014**, *114*, 1287−1317.
(30) Orlando, R.; Delle Piane, M.; Bush, I. J.; Ugliengo, P.; Ferrabone, M.; Dovesi, R. A New Massively Parallel Version of CRYSTAL for Large Systems on High Performance Computing Architectures. *J. Comput. Chem.* **2012**, *33*, 2276−2284.
(31) Perdew, J. P.; Burke, K.; Ernzerhof, M. Generalized Gradient Approximation Made Simple. *Phys. Rev. Lett.* **1996**, *77*, 3865−3868.
(32) Grimme, S. Semiempirical GGA-Type Density Functional Constructed with a Long-Range Dispersion Correction. *J. Comput. Chem.* **2006**, *27*, 1787−1799.
(33) Schafer, A.; Horn, H.; Ahlrichs, R. Fully Optimized Contracted Gaussian-Basis Sets for Atoms Li to Kr. *J. Chem. Phys.* **1992**, *97*, 2571−2577.
(34) Nada, R.; Nicholas, J. B.; McCarthy, M. I.; Hess, A. C. Basis Sets for Ab Initio Periodic Hartree-Fock Studies of Zeolite/Adsorbate Interactions: He, Ne, and Ar in Silica Sodalite. *Int. J. Quantum Chem.* **1996**, *60*, 809−820.
(35) Apra, E.; Causa, M.; Prencipe, M.; Dovesi, R.; Saunders, V. R. On the Structural Properties of NaCl: An Ab Initio Study of the B1−B2 Phase Transition. *J. Phys.: Condens. Matter* **1993**, *5*, 2969−2976.
(36) Dall'Olio, S.; Dovesi, R.; Resta, R. Spontaneous Polarization as a Berry Phase of the Hartree-Fock Wave Function: The Case of KNbO3. *Phys. Rev. B* **1997**, *56*, 10105−10114.
(37) Hutter, J.; Iannuzzi, M.; Schiffmann, F.; VandeVondele, J. CP2K: Atomistic Simulations of Condensed Matter Systems. *Wiley Interdiscip. Rev. Comput. Mol. Sci.* **2014**, *4*, 15−25.
(38) VandeVondele, J.; Krack, M.; Mohamed, F.; Parrinello, M.; Chassaing, T.; Hutter, J. Quickstep: Fast and Accurate Density Functional Calculations Using a Mixed Gaussian and Plane Waves Approach. *Comput. Phys. Commun.* **2005**, *167*, 103−128.
(39) Goedecker, S.; Teter, M.; Hutter, J. Separable Dual Space Gaussian Pseudo-Potentials. *Phys. Rev. B* **1996**, *54*, 1703−1710.
(40) VandeVondele, J.; Hutter, J. Gaussian Basis Sets for Accurate Calculations on Molecular Systems in Gas and Condensed Phases. *J. Chem. Phys.* **2007**, *127*, 114105.
(41) Bussi, G.; Donadio, D.; Parrinello, M. Canonical Sampling through Velocity Rescaling. *J. Chem. Phys.* **2007**, *126*, 014101.
(42) Thommes, M.; Köhn, R.; Fröba, M. Sorption and Pore Condensation Behavior of Pure Fluids in Mesoporous MCM-48 Silica, MCM-41 Silica, SBA-15 Silica and Controlled-Pore Glass at Temperatures above and below the Bulk Triple Point. *Appl. Surf. Sci.* **2002**, *196*, 239−249.
(43) Verevkin, S. P.; Ralys, R. V.; Zaitsau, D. H.; Emel'yanenko, V. N.; Schick, C. Express Thermo-Gravimetric Method for the Vaporization Enthalpies Appraisal for Very Low Volatile Molecular and Ionic Compounds. *Thermochim. Acta* **2012**, *538*, 55−62.
(44) Price, D. M. Vapor Pressure Determination by Thermogravimetry. *Thermochim. Acta* **2001**, *367*, 253−262.
(45) Chickos, J. S.; Hosseini, S.; Hesse, D. G.; Liebman, J. F. Heat Capacity Corrections to a Standard State: A Comparison of New and Some Literature Methods for Organic Liquids and Solids. *Struct. Chem.* **1993**, *4*, 271−278.
(46) Song, H.; Shin, H.-S. The Antifungal Drug Clotrimazole. *Acta Crystallogr., Sect. C* **1998**, *54*, 1675−1677.
(47) Sliwinska-Bartkowiak, M.; Dudziak, G.; Gras, R.; Sikorski, R.; Radhakrishnan, R.; Gubbins, K. E. Freezing Behavior in Porous Glasses and MCM-41. *Colloids Surf., A* **2001**, *187*, 523−529.
(48) Qian, K. K.; Zhou, W.; Xu, X. M.; Udovic, T. J. Characterization of Medicinal Compounds Confined in Porous Media by Neutron Vibrational Spectroscopy and First-Principles Calculations: A Case Study with Ibuprofen. *Pharm. Res.* **2012**, *29*, 2432−2444.
(49) Ambrogi, V.; Perioli, L.; Marmottini, F.; Accorsi, O.; Pagano, C.; Ricci, M.; Rossi, C. Role of Mesoporous Silicates on Carbamazepine Dissolution Rate Enhancement. *Microporous Mesoporous Mater.* **2008**, *113*, 445−452.
(50) Ambrogi, V.; Marmottini, F.; Pagano, C. Amorphous Carbamazepine Stabilization by the Mesoporous Silicate SBA-15. *Microporous Mesoporous Mater.* **2013**, *177*, 1−7.
(51) Civalleri, B.; Zicovich-Wilson, C. M.; Valenzano, L.; Ugliengo, P. B3LYP Augmented with an Empirical Dispersion Term (B3LYP-D) as Applied to Molecular Crystals. *CrystEngComm* **2008**, *10*, 405−410.
(52) Ugliengo, P.; Sodupe, M.; Musso, F.; Bush, I. J.; Orlando, R.; Dovesi, R. Realistic Models of Hydroxylated Amorphous Silica Surfaces and MCM-41 Mesoporous Material Simulated by Large-Scale Periodic B3LYP Calculations. *Adv. Mater.* **2008**, *20*, 4579−4583.
(53) Zhuravlev, L. T. Concentration of Hydroxyl Groups on the Surface of Amorphous Silicas. *Langmuir* **1987**, *3*, 316−318.
(54) Tsuzuki, S.; Honda, K.; Uchimaru, T.; Mikami, M.; Tanabe, K. Origin of Attraction and Directionality of the π/π Interaction: Model Chemistry Calculations of Benzene Dimer Interaction. *J. Am. Chem. Soc.* **2002**, *124*, 104−112.
(55) Connolly, M. L. Computation of Molecular Volume. *J. Am. Chem. Soc.* **1985**, *107*, 1118−1124.
(56) Pimentel, G. C.; Sederholm, C. H. Correlation of Infrared Stretching Frequencies and Hydrogen Bond Distances in Crystals. *J. Chem. Phys.* **1956**, *24*, 639−641.
(57) Ugliengo, P.; Viterbo, D.; Chiari, G. MOLDRAW: Molecular Graphics on a Personal Computer. *Z. Krist.* **1993**, *208*, 383−383.
(58) Humphrey, W.; Dalke, A.; Schulten, K. VMD: Visual Molecular Dynamics. *J. Mol. Graph.* **1996**, *14*, 33−38.
(59) Stone, J. An Efficient Library for Parallel Ray Tracing and Animation. In *Intel Supercomputer Users Group Proceedings*; Computer Science Department, University of Missouri-Rolla: Missouri, 1995; pp 1−5.

DOI: 10.1021/acs.jpcc.5b02666
J. Phys. Chem. C XXXX, XXX, XXX−XXX

Microporous and Mesoporous Materials 200 (2014) 291–296

Contents lists available at ScienceDirect

Microporous and Mesoporous Materials

journal homepage: www.elsevier.com/locate/micromeso

Incorporation of clotrimazole in Ordered Mesoporous Silica by supercritical CO_2

Andrea Gignone, Luigi Manna, Silvia Ronchetti, Mauro Banchero, Barbara Onida [1,*]

Department of Applied Science and Technology, Politecnico di Torino, Corso Duca degli Abruzzi 24, 10129 Torino, Italy

ARTICLE INFO

Article history:
Received 30 January 2014
Accepted 23 May 2014
Available online 4 June 2014

Keywords:
Mesoporous silica
Supercritical CO_2
Drug incorporation
Clotrimazole

ABSTRACT

Clotrimazole, a poorly water soluble antifungal active principle widely used in dermatology, was incorporated inside Ordered Mesoporous Silica (OMS) of the MSU-H type, using supercritical CO_2 ($scCO_2$) as solvent. The pristine OMS was characterized by a specific surface area of about 600 m^2/g, a total specific pore volume of 0.900 cm^3/g and an average pore size of 8.5 nm. The incorporation process was carried out in a high pressure stainless steel vessel at 25.0 MPa and 50.0 MPa, at 373 K. The time of incorporation process was varied from 6 to 18 h. The amount of incorporated clotrimazole was observed to increase with increasing incorporation time up to 12 h. Longer times (18 h) did not affect the incorporated amount. The maximum drug loading was 34% w/w, three times higher than that obtained by adsorption from ethanol solution (9.0% w/w).

The clotrimazole-containing OMS was characterized by X-ray diffraction, field emission scanning electron microscopy, thermogravimetry, infrared spectroscopy and nitrogen adsorption. The clotrimazole resulted not crystalline and homogenously distributed inside the mesopores. A model of mesopores occupation by clotrimazole molecules in the form of a molecular layer is proposed.

1. Introduction

Controlled drug release aims at optimizing drug efficiency while simultaneously reducing adverse collateral effects. Several studies have shown that pharmacokinetics, drug efficiency and suppression of undesired side effects in different pathological conditions can be improved by correct timing of drug administration and controlled kinetics of drug release [1].

In this context, Ordered Mesoporous Silicas (OMSs) have been widely investigated as drug carriers in several fields [2], from tissue engineering to cancer therapy.

Initially, the research on OMSs for drug delivery was focused on the achievement of controlled release formulations. The release kinetics of drugs by OMSs depends on several carrier properties, including pore size [3], pore connectivity [4] and the chemical composition of the surface [5].

A recent emerging feature of OMS carriers is the enhanced oral bioavailability of molecules that are poorly soluble in water [6].

In the first pioneering work by Vallet-Regi et al. [7], drug incorporation in MCM-41 was carried out by adsorption from a solution using hexane as the solvent.

Since the long-term toxicity of *n*-hexane in humans is well known [8,9], many other solvents have been studied for the incorporation. For instance, Charnay et al. [10] reported that when highly polar solvents such as dimethyl sulfoxide (DMSO), dimethylformamide (DMF) and dimethylacetamide (DMA) were used, the amount of adsorbed drug was limited, whereas a higher quantity of drug was incorporated when ethanol or hexane was used. The drug incorporation is strongly affected by the solvent due to the competition between the drug and the solvent in the adsorption [10,11].

The incorporation through supercritical carbon dioxide ($scCO_2$) is an alternative to adsorption or impregnation from a liquid solution.

Carbon dioxide is one of the most commonly used fluids in supercritical fluid technology [12]. It presents the advantage of having a critical temperature close to ambient temperature (304.25 K) and a critical pressure which is not too high (7.39 MPa). In addition, it is non-flammable, it has low cost and low toxicity. As all supercritical fluids, supercritical carbon dioxide has physical properties in between those of a gas and a liquid; in particular, it has a solvent power like a liquid and a high diffusivity like a gas. At pressures and temperatures not too far from its

* Corresponding author. Tel.: +39 011 090 4631.
E-mail address: barbara.onida@polito.it (B. Onida).
[1] CR-INSTM for Materials with Controlled Porosity, Italy.

http://dx.doi.org/10.1016/j.micromeso.2014.05.031
1387-1811/

critical point, a supercritical fluid has a high compressibility, therefore its density and hence its solvent power are easily adjustable over a wide range with a minimal change in temperature or pressure. This tunability may be used to control the phase behavior in separation processes.

The incorporation of drugs in polymers [13,14], as well as in aerogels [15] using $scCO_2$ has been widely reported. On the other hand, only a few examples of including active principles in Ordered Mesoporous Silica by using $scCO_2$ [16–18] can be found. Furthermore, in one of these cases a co-solvent (acetone or methanol) was used [18].

Belhadj-Ahmed et al. [16] investigated the supercritical impregnation of vitamine E acetate on silica matrices by means of a dynamic technique. Min et al. studied the incorporation of ibuprofen inside SBA-15 through $scCO_2$ [17], showing that the loaded drug quantity increased with a higher solubility of ibuprofene in $scCO_2$.

The aim of this work is to study the incorporation of clotrimazole (1-[(2-chlorophenyl)(diphenyl)methyl]-1H-imidazole) through $scCO_2$ into an OMS of the MSU-H type [19]. A detailed study of the solubility of clotrimazole in $scCO_2$ is present in literature [20].

MSU-H is a two-dimensional, hexagonally ordered silica with large uniform mesopores assembled through a nonionic supramolecular assembly pathway using sodium silicate as a silica source and the triblock copolymer Pluronic P123 ($EO_{20}PO_{70}EO_{20}$) as a structure-directing agent. The framework structure of MSU-H is analogous to that of SBA-15 and consists of large ordered pores connected by micropores in the pore walls. Morphology of MSU-H differs from that of SBA-15, in that SBA-15 mesostructures usually assemble into larger and more monolithic particles [19].

Clotrimazole is an active principle ingredient that is poorly soluble in water and is present in antifungal topical medications commonly used in the treatment of fungal infections (of both humans and animals) [21]. It is commonly available as an over-the-counter drug in various forms including creams.

The formulation of eudermic compositions containing OMS, which allow a constant concentration of the active principle ingredient to remain on the application site for a controlled time, has been recently patented [22].

The incorporation of clotrimazole in silica xerogel monolith from aqueous solution has been previously reported [23]. Instead, at the best of our knowledge the incorporation of clotrimazole inside OMS particles is herein reported for the first time. In particular, no examples of incorporation of this molecule into a porous solid matrix through $scCO_2$ is available in the literature.

The study of incorporation of clotrimazole in OMS through $scCO_2$ herein discussed is focussed on the effect of process conditions, such as time and pressure, on the incorporated amount. Prior to this, the effect of the supercritical solvent on the structure and morphology of the OMS was characterized.

At variance with previous studies [16,17], where the effect of drug solubility in $scCO_2$ on the incorporated amount was mainly discussed, herein the form of the drug hosted inside the OMS is examined in detail.

2. Experimental

Clotrimazole ($C_{22}H_{17}ClN_2$) and Ordered Mesoporous Silica (MSU-H type) were purchased from Sigma–Aldrich. Carbon dioxide with a purity of 99.5% was supplied by SIAD.

2.1. Drug loading

A homemade device was used to perform the incorporation of the drug by means of $scCO_2$. This consists in a glass cylinder of 1 cm diameter containing a pellet of clotrimazole (100 mg) and a pellet of OMS (100 mg) separated by a disc of filter paper, in order to prevent their contact and to allow their separation at the end of the incorporation process. This approach differs from those previously reported by Belhadj-Ahmed et al. [16] and by Min et al. [17], where the not-pelletized OMS powder was used.

This device was placed inside a stainless steel vessel, which was put in an oven that maintained all the system at constant temperature. The apparatus was also equipped with a volumetric pump and a back pressure regulator. Further details on the apparatus can be found elsewhere [24].

The incorporation was performed in static condition. The vessel was filled with liquid carbon dioxide and heated up to 373 K. After the heating, additional carbon dioxide was pumped in the vessel to reach the final desired pressure (25.0 MPa or 50.0 MPa). The system was then maintained in the described conditions for several hours (from 6 to 18) to allow the drug dissolution and diffusion into the OMS.

At the end of the incorporation process, the apparatus was depressurized and the temperature was decreased to room conditions.

In order to characterize the effects of the $scCO_2$ on the OMS, an additional experiment (25.0 MPa, 373 K, 12 h) was performed on a sole pellet of OMS, i.e. without the pellet of clotrimazole in the glass cylinder.

For comparison, incorporation of clotrimazole was also performed by adsorption from ethanol solution. To this purpose, 300 mg of clotrimazole and 100 mg of OMS were introduced in a Erlenmeyer flask with 5 ml of ethanol (99.8%, Sigma–Aldrich) and maintained at room temperature under stirring for 24 h. Then the powder was filtered and dried overnight in vacuum (residual pressure 0.1 Pa).

2.2. Characterization

Samples were characterized by means of X-ray diffraction (XRD), thermogravimetry (TG), fourier transform infrared spectroscopy (FTIR), nitrogen adsorption isotherms and field emission scanning microscopy (FESEM).

XRD patterns were obtained using a PANalytical X'Pert Powder (Cu K_α radiation) diffractometer. TG analyses were carried out between 298 K and 1073 K in air (flow rate 100 mL/min with a heating rate of 10 K/min) using a SETARAM 92 instrument. Nitrogen adsorption isotherms were measured using a Quantachrome AUTOSORB-1 instrument. Prior to nitrogen adsorption, samples were outgassed at 393 K for 2 h. BET specific surface areas were calculated in the relative pressure range 0.04–0.1 and the pore size distribution were determined through the DFT (Density Functional Theory) method, using the NLDFT equilibrium model for cylindrical pores [25]. FESEM image were recorded with a FESEM ZEISS MERLIN. For FTIR measurements powders were pressed in self-supporting wafers and spectra were recorded at room temperature with a Bruker Tensor 27 spectrometer operating at 2 cm^{-1} resolution, after outgassing the sample at 373 K for 1 h (residual pressure equal to 0.1 Pa).

FTIR spectrum of crystalline clotrimazole was recorded on the powder dispersed in potassium bromide. FTIR spectrum of clotrimazole in solution was recorded on a diluted carbon tetrachloride solution (1 g/L).

3. Results and discussion

The effect of the $scCO_2$ treatment on the structure and morphology of OMS was investigated by means of XRD and FESEM prior to

the incorporation of clotrimazole because no study of the effects of $scCO_2$ on OMS is reported in literature.

Fig. 1 reports the wide angle XRD patterns of the sample before (Curve 1) and after (Curve 2) the $scCO_2$ treatment, which was carried out at 25.0 MPa and 373 K for 12 h without clotrimazole. No significant changes are observed in the pattern, which is typical of the MSU-H hexagonal structure [19].

Fig. 2 reports the FESEM micrographs of the same sample before (1) and after (2) the $scCO_2$ treatment. As for the XRD data, negligible variations are observed. Both XRD and FESEM results show that the $scCO_2$ process as such does not affects significantly the structure and the morphology of the OMS used in the study.

$ScCO_2$ was used to incorporate clotrimazole (Scheme 1) inside the OMS. Pressure and time of the $scCO_2$ treatment were varied, in order to investigate the effect on the amount of incorporated clotrimazole, whereas the temperature was maintained constant and equal to 373 K. This temperature was chosen significantly higher than the critical temperature of carbon dioxide, at variance with what was reported by Belhadj-Ahmed et al. [16] and by Min et al. [17]. Thermal degradation of clotrimazole can be ruled out since it was reported to occur at 453 K [21]. The selected working pressures ensured a good solvent power of the fluid. The density and solubility parameter were respectively equal to 550 kg/m^3 and 9.1 (MJ/m^3)$^{1/2}$ at 25.0 MPa, while they were 819 kg/m^3 and 12.5 (MJ/m^3)$^{1/2}$ at 50.0 MPa.

As a whole, four different incorporation procedures were carried out and their typical parameters are summarized in Table 1, together with the corresponding loading of incorporated clotrimazole, which was measured by TG analyses.

The maximum amount of incorporated clotrimazole, corresponding to 34% w/w (percentage by weight), was obtained at 50.0 MPa after a 12-h-supercritical treatment.

Data in Table 1 reveal that time plays a crucial role up to 12 h. In fact, the clotrimazole loading increased from 12% w/w to 30% w/w when time increased from 6 h to 12 h at 25.0 MPa, whereas no further increase was observed when the process was carried out for a longer time, i.e. 18 h, at the same pressure. These data suggest that after 12 h the equilibrium between clotrimazole in $scCO_2$ and clotrimazole inside the OMS was reached. This differs from the result obtained by Belhadj-Ahmed et al. [16], who observed no change in the active principle incorporated amount for periods of time longer than 1 h. This discrepancy is probably due to the dissimilar experimental procedure.

At variance, pressure was observed to affect the incorporated amount only at a minor extent, since an increase from 25.0 MPa to 50.0 MPa yields a limited increase of the clotrimazole percentage (from 30% to 34%), probably due to a higher solubility of clotrimazole in $scCO_2$ at higher pressure.

It is worth noting that the incorporation via $scCO_2$ was largely more efficient than that obtained by adsorption from ethanol solution. In fact, in the latter case the percentage of clotrimazole inside OMS was only 9.0%. Moreover, the amount of clotrimazole used for the adsorption was three times higher than that of OMS, at variance with the $scCO_2$ treatment for which the same amounts of clotrimazole and OMS were used.

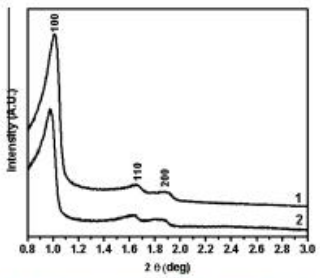

Fig. 1. Wide angle XRD patterns of OMS before (Curve 1) and after (Curve 2) treatment in $scCO_2$ (25.0 MPa, 373 K, 12 h).

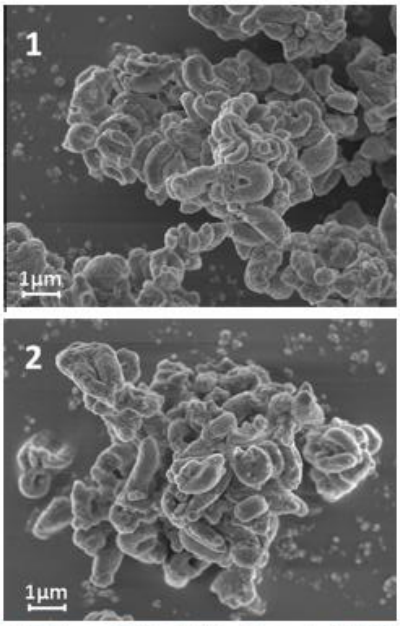

Fig. 2. FESEM images of OMS before (1) and after (2) treatment in $scCO_2$ (25.0 MPa, 373 K, 12 h).

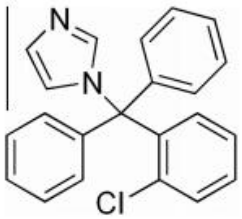

Scheme 1. Structure of clotrimazole.

Table 1
Incorporation process parameters for $scCO_2$ and ethanol solution (EtOH) and corresponding clotrimazole loading (% w/w) evaluated by TG analysis.

Incorporation procedure	Time (h)	Temperature (K)	Pressure (MPa)	Drug-OMS ratio*	Loading (% w/w)
$scCO_2$-1	6	373	25.0	1:1	12
$scCO_2$-2	12	373	25.0	1:1	30
$scCO_2$-3	12	373	50.0	1:1	34
$scCO_2$-4	18	373	25.0	1:1	30
EtOH	24	298	0.1	3:1	9.0

* Weight ratio.

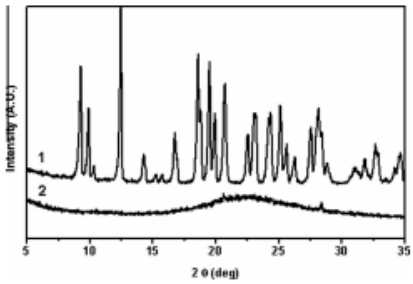

Fig. 3. XRD patterns of: (1) crystalline clotrimazole, (2) clotrimazole-containing OMS ($scCO_2$-3, 34% w/w).

Fig. 3 reports the XRD patterns of the pure clotrimazole in crystalline form (Curve 1) and the OMS containing the highest amount of clotrimazole (34% w/w; Curve 2). No diffraction peaks of the crystalline clotrimazole are observed in the latter case, evidencing that the incorporated molecules are not assembled in the crystalline structure. This result is in agreement with data reported by Sliwinska-Bartkowiak et al. [26] for nitrobenzene in pores of controlled pore glass (CPG), Vycor and MCM-41. The authors suggested that the crystallization did not occur for pore sizes smaller than twelve times the molecule diameter. In addition to this, the physical stabilization of the non-crystalline form of carbamazepine inside MCM-41 and SBA-15 for 6 month was reported by Ambrogi et al. [27,28].

Amorphization of ibuprofen by incorporation in mesoporous silica was also reported by Qian et al. [29].

The lack of crystallization is crucial, because amorphous drugs are widely accepted to have higher aqueous solubility and dissolution rate than related crystalline phases. This effect may be particularly important when molecules poorly soluble in water, such as clotrimazole, are considered [6,27,28,30].

Fig. 4 reports the FTIR spectra of OMS as such (Curve 1), clotrimazole-containing OMS (34% w/w; Curve 2), clotrimazole in solution (Curve 3) and crystalline clotrimazole (Curve 4).

Spectrum 1 shows the typical absorptions of amorphous silica, i.e. the narrow band at 3745 cm^{-1} due to isolated silanols, and the broad absorption at about 3550 cm^{-1} due to H-bonded silanols [31]. When the spectrum of clotrimazole in crystalline form (Curve 4) is compared with that of the molecule in solution (Curve 3) it is worth noting that in the latter case bands due to aromatic C–H stretching modes, above 3000 cm^{-1}, appear broader and less defined.

The spectrum of clotrimazole-containing OMS (Curve 2) does not show the band due to isolated silanols at 3745 cm^{-1}. At variance, a broad band is observed at 3630 cm^{-1}, together with a broad and ill-defined absorption centered at about 3000 cm^{-1}, to which the C–H stretching modes of clotrimazole are superimposed.

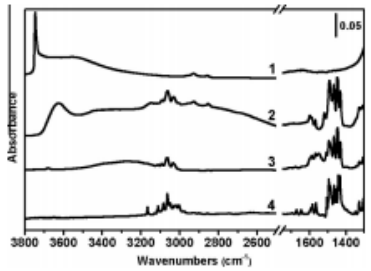

Fig. 4. FT-IR spectra of: (1) OMS, (2) clotrimazole-containing OMS ($scCO_2$-3, 34% w/w), (3) clotrimazole in CCl_4 solution, (4) crystalline clotrimazole dispersed in KBr.

The band at 3630 cm^{-1} is ascribed to the stretching mode of surface silanols interacting via H-bonding with the aromatic ring of clotrimazole molecule. In fact, the shift suffered by the SiOH stretching mode results −115 cm^{-1}, which is similar to that observed for silanol H-bonded to benzene, that is −120 ± 10 cm^{-1} [32]. The ill-defined absorption centered at about 3000 cm^{-1} is ascribed to the stretching mode of silanols H-bonded to the Nitrogen atom of the imidazole ring of clotrimazole molecule. The shift may be roughly evaluated as about −750 cm^{-1}, similar to that reported for silanol interacting with the Nitrogen atom of pyridine, i.e. −765 ± 50 cm^{-1} [32].

Bands due to aromatic C–H stretching modes of clotrimazole, above 3000 cm^{-1}, are similar to that of clotrimazole in solution, i.e. they are broader and less defined than the corresponding bands observed for crystalline clotrimazole. This evidences that incorporated clotrimazole is not in the crystalline form, in agreement with XRD data.

The absence of the band at 3745 cm^{-1} due to free isolated silanols indicates that most of the silica surface is occupied by clotrimazole molecules.

Nitrogen adsorption isotherms were measured to characterize the specific surface area, the specific pore volume and the pore size distribution of OMS as such and clotrimazole-containing OMS.

Fig. 5 reports both the adsorption and desorption branches for OMS as such (1) and OMS containing 34% w/w clotrimazole (2).

BET specific surface area decreased from 597 m^2/g for OMS as such to 157 m^2/g for clotrimazole-containing OMS and the pore volume decreased from 0.900 cm^3/g to 0.289 cm^3/g, respectively.

From the grams of clotrimazole incorporated inside the sample, the volume occupied by clotrimazole can be calculated and the residual free mesopore volume in clotrimazole-containing OMS can be estimated. This estimation is strongly affected by the density considered for clotrimazole in the calculation. Assuming a density of 1.316 g/cm^3, i.e. the density known for crystalline clotrimazole [33], the mesopore volume in clotrimazole-containing OMS resulted equal to 0.336 cm^3/g. This value is in fair agreement with that obtained by N_2 adsorption measurement (0.289 cm^3/g). The discrepancy of 0.047 cm^3/g may arise from the value of clotrimazole density used in the calculation. Indeed, XRD pattern showed that clotrimazole in OMS lacks of crystalline form and its density is likely to be lower than that of the crystalline phase.

These considerations strongly suggest that clotrimazole molecules are homogeneously distributed inside mesoporores and that no pores occlusion occurred.

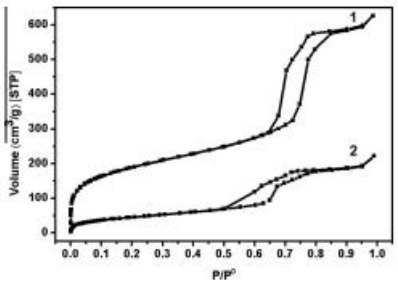

Fig. 5. N_2 adsorption isotherms of OMS (1) and clotrimazole-containing OMS ($scCO_2$-3, 34% w/w) (2).

Fig. 6a reports the pore size distributions obtained from the nitrogen sorption isotherms in Fig. 5. For OMS as such (Curve 1) a main family of pores with an average diameter of 8.5 nm is observed. In the case of clotrimazole-containing OMS (Curve 2) this family of pores is not present, whereas new families of pores (apparently two) with smaller diameter, in the range 5–7 nm, appear. The presence of smaller mesopores in the clotrimazole-containing OMS is in agreement with the coverage of the internal mesopores surface by clotrimazole molecules, as revealed by FTIR data.

For the first time, an attempt has been made to model the occupation of mesopores by drug molecules. In fact in the previous works [16–18] no elucidation about the drug distribution was presented.

On the basis of the above results, a model corresponding to a layer of clotrimazole molecules on the surface of mesopores was chosen.

Fig. 7 is a pictorial representation of empty mesopores, i.e. those present in OMS as such (on the left), together with mesopores occupied by the clotrimazole molecules layer, i.e. those assumed for clotrimazole-containing OMS (on the right).

Starting from the pore size distribution of OMS as such (Fig. 6a, Curve 1), the pore size distribution for clotrimazole-containing OMS can be calculated.

The volume V_0 of a single cylindrical empty mesopore is given by:

$$V_0 = \frac{\pi}{4} \cdot d_0^2 \cdot h \tag{1}$$

where d_0 is the mesopore diameter and h is the mesopore elongation.

The volume V_1 of a single cylindrical mesopore occupied by the clotrimazole layer is given by:

$$V_1 = \frac{\pi}{4} \cdot d_1^2 \cdot h \tag{2}$$

where d_1 is calculated as:

$$d_1 = d_0 - 2d_{do} \tag{3}$$

and d_{do} is the diameter of a clotrimazole molecule considered as a sphere (1.2 nm) calculated by MOLDRAW molecular graphics [34]. Combining Eqs. (1) and (2), Eq. (4) is obtained, which, substituting d_1 as in Eq. (3), gives rise to Eq. (5).

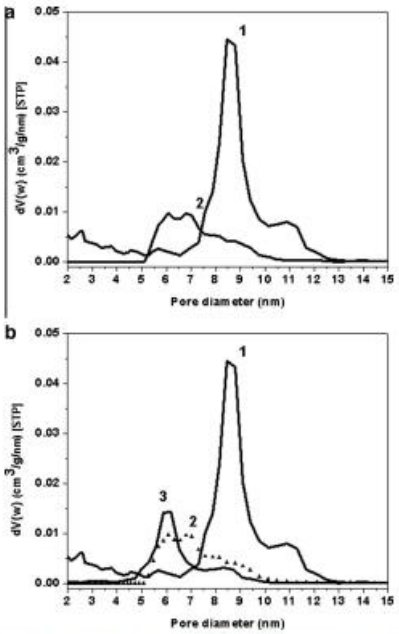

Fig. 6. Section (a): pore size distribution of OMS (1) and clotrimazole-containing OMS ($scCO_2$-3, 34% w/w) (2). Section (b): Curve 1 and Curve 2 are as in section (a); Curve 3 is the calculated pore size distribution of clotrimazole-containing OMS ($scCO_2$-3, 34% w/w).

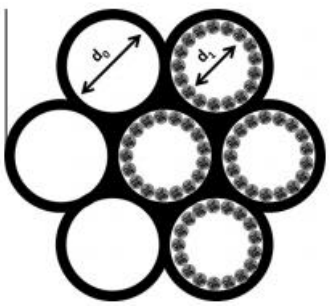

Fig. 7. Pictorial representation of empty mesopores (d_0) and mesopores occupied by the clotrimazole layer (d_1).

$$\frac{V_0}{V_1} = \frac{d_0^2}{d_1^2} \quad (4)$$

$$V_1 = \frac{(d_0 - 2d_{cw})^2}{d_0^2} \cdot V_0 \quad (5)$$

A new pore size distribution can be calculated from this equation, on the basis of the values of V_0 and d_0 of the pore size distribution of OMS as such (Fig. 6a), experimentally obtained by the nitrogen adsorption isotherm. In order to do so, V_0 and V_1 in Eq. (5) have to be normalized to the same quantity of silica, because V_0 is a specific pore volume, expressed in cm^3/g. This means that, if g_{sil} is the amount of OMS as such (silica), the amount of clotrimazole-containing OMS is $g_{sil} + g_{clo}$, where g_{clo} has been evaluated by TG. Accordingly, Eq. (5) is rewritten as Eq. (6).

$$V_1 = \frac{(d_0 - 2d_{cw})^2}{d_0^2} \cdot V_0 \cdot \frac{g_{sil}}{g_{sil} + g_{clo}} \quad (6)$$

The calculated pore size distribution is the Curve 3 in Fig. 6b. The curve shows a maximum at about 6 nm and it is in fair agreement with the pore size distribution of clotrimazole-containing OMS (Curve 2).

On the basis of the calculated pore size distribution and experimental results showing a homogeneous distribution of clotrimazole molecules inside mesopores, it can be concluded that clotrimazole was incorporated inside the OMS mainly in the form of a molecular layer.

This is in agreement with previous data reported for itraconazole by Mellaerts et al. [6], who observed a molecular dispersion of the drug in OMS.

4. Conclusions

Clotrimazole was incorporated for the first time in OMS (MSU-H type, SSA equal to 597 m^2/g and pore diameter equal to 8.5 nm) by means of $scCO_2$. The incorporation process carried out at 50.0 MPa and 373 K for 12 h yielded a clotrimazole loading of 34% w/w. This value was more than three times higher than that obtained by adsorption from ethanol solution at room temperature (9.0% w/w).

XRD, FTIR, TG and nitrogen adsorption data showed that clotrimazole was homogenously distributed inside mesopores in a non-crystalline form.

The pore size distribution of the clotrimazole-containing OMS was calculated starting from the pore size distribution of OMS as such, assuming the occupation of mesopores by clotrimazole molecules in the form of a layer. The calculated pore size distribution showed a maximum at about 6 nm, in fair agreement with the pore size distribution obtained for clotrimazole-containing OMS from the nitrogen adsorption isotherm.

Therefore it can be concluded that clotrimazole was incorporated inside the OMS mainly in the form of a molecular layer.

References

[1] A.M. Hillery, A.W. Lloyd, J. Swarbrick, Drug Delivery and Targeting, first., Taylor & Francis, London, 2001.
[2] M. Vallet-Regí, Chem. Eur. J. 12 (2006) 5934–5943.
[3] P. Horcajada, A. Ramila, P. Perez-Pariente, M. Vallet-regí, Microporous Mesoporous Mater. 68 (2004) 105–109.
[4] J. Andersson, J. Rosenholm, S. Areva, M. Linden, Chem. Mater. 16 (2004) 4160–4167.
[5] B. Munoz, A. Ramila, J. Perez-Pariente, I. Díaz, M. Vallet-Regí, Chem. Mater. 15 (2003) 500–503.
[6] R. Mellaerts, R. Mols, J.A.G. Jammaer, J.A. Martens, J. Van Humbeeck, G.V. Mooter, G. Van den Mooter, P. Augustijns, C.A. Aerts, P. Annaert, Eur. J. Pharm. Biopharm. 69 (2008) 223–230.
[7] M. Vallet-Regí, A. Ramila, R.P. del Real, J. Perez-Pariente, Chem. Mater. 13 (2001) 308–311.
[8] A. Hershkowitz, N. Ishii, H. Schaumburg, N. Engl. J. Med. 285 (1971) 82–85.
[9] H.H. Schaumburg, P.S. Spencer, Brain 99 (1976) 183–192.
[10] C. Chamay, S. Bégu, C. Tourné-Péteilh, L. Nicole, D.A. Lerner, J.M. Devoisselle, Eur. J. Pharm. Biopharm. 57 (2004) 533–540.
[11] R. Aiello, G. Cavallaro, G. Giammona, L. Pasqua, P. Pierro, F. Testa, Stud. Surf. Sci. Catal. 142 (2002) 1165–1172.
[12] R. Span, W. Wagner, J. Phys. Chem. Ref. Data 25 (1996) 1509–1596.
[13] O.R. Davies, A.L. Lewis, M.J. Whitaker, H. Tai, K.M. Shakesheff, S.M. Howdle, Adv. Drug Delivery Rev. 60 (2008) 373–387.
[14] I. Kikic, F. Vecchione, Curr. Opin. Solid State Mater. 7 (2003) 399–405.
[15] I. Smirnova, J. Mamic, W. Arlt, Langmuir 19 (2003) 8521–8525.
[16] F. Belhadj-Ahmed, E. Badens, P. Llewellyn, R. Denoyel, G. Charbit, J. Supercrit. Fluids 51 (2009) 278–286.
[17] N. Min, X. Qin-Qin, Y. Jian-Zhong, J. Mater. Res. 27 (2012) 2902–2910.
[18] A. Patil, U.N. Chirmade, I. Slipper, D.A. Lamprou, A. Urquhart, J. Nanomedic. Nanotechnology 02 (2011).
[19] S.-S. Kim, A. Karkamkar, T.J. Pinnavaia, M. Kruk, M. Jaroniec, J. Phys. Chem. B 105 (2001) 7663–7670.
[20] Y. Yamini, M. Moradi, J. Chem. Thermodyn. 43 (2011) 1091–1096.
[21] J.G. Hoogerheide, B.E. Wyka, in: K. Florey (Ed.), Analytical Profiles of Drug Substances, Academic Press, Inc., New York, 1982, pp. 225–255.
[22] B. Onida, R. Mortera, Eudermic compositions, WO 2012/007906 A2.
[23] O. Cristini-Robbe, F. Ruyffelaere, F. Dubart, A. Uwimana-mpuye, C. Kinowski, R. Bernard, C. Masselot-Robbe, J.E. Yazidi, S. Tsunell, J. Glass Ceram. 03 (2013) 74–79.
[24] M. Banchero, L. Manna, S. Ronchetti, P. Campanelli, A. Ferri, J. Supercrit. Fluids 49 (2009) 271–278.
[25] M. Thommes, R. Kohn, M. Fröba, Appl. Surf. Sci. 196 (2002) 239–249.
[26] M. Sliwinska-Bartkowiak, G. Dudziak, R. Gras, R. Sikorski, R. Radhakrishnan, K.E. Gubbins, Colloid Surf. A 187–188 (2001) 523–529.
[27] V. Ambrogi, L. Perioli, F. Marmottini, O. Accorsi, C. Pagano, M. Ricci, C. Rossi, Microporous Mesoporous Mater. 113 (2008) 445–452.
[28] V. Ambrogi, F. Marmottini, C. Pagano, Microporous Mesoporous Mater. 177 (2013) 1–7.
[29] K. Qian, W. Zhou, X. Xu, T. Udovic, Pharm. Res. 29 (2012) 2432–2444.
[30] R. Mellaerts, C.A. Aerts, J.V. Humbeeck, P. Augustijns, G.V. den Mooter, J.A. Martens, Chem. Commun. (2007) 1375–1377.
[31] P. Ugliengo, M. Sodupe, F. Musso, I.J. Bush, R. Orlando, R. Dovesi, Adv. Mater. 20 (2008) 1–5.
[32] W. Hertl, M.L. Hair, J. Phys. Chem. 72 (1968) 4676–4682.
[33] H. Song, H.S. Shin, Acta Crystallogr. C 54 (1998) 1675–1677.
[34] P. Ugliengo, D. Viterbo, G. Chiari, Z. Kristallogr. 208 (1993) 383–383.